

Prof. Dr. Wolfhard Möller

Fundamentals of Ion-Surface Interaction

Short Resume

of a lecture held at Technische Universität Dresden

Last Revision: August 2009

**Prof. Dr. Wolfhard Möller
Helmholtz-Zentrum Dresden-Rossendorf
Postfach 510119
01314 Dresden**

**Tel. 0351-2602245
w.moeller@hzdr.de
<http://www.hzdr.de/FWI>**

Intention

It is the purpose of these notes to present a short display of the physical issues and the main results presented in the lecture "Fundamentals of Ion-Surface Interaction". It is not meant to replace a textbook. For details, extended discussions and mathematical derivations, the reader is referred to the literature.

Literature

1. N.Bohr: The Penetration of Atomic Particles Through Matter (Kgl.Dan.Vid.Selsk.Mat. Fys.Medd. 18,8(1948))
2. Gombas: Statistische Behandlung des Atoms in: Handbuch der Physik Bd. XXXVI (Springer, Berlin 1959)
3. J.Lindhard et al.: Notes on Atomic Collisions I-III (Kgl.Dan.Vid.Selsk.Mat.Fys.Medd. 36,10(1968), 33,14(1963), 33,10(1963))
4. U.Fano: Penetration of Protons, Alpha Particles, and Mesons (Ann.Rev.Nucl.Sci. 13(1963)1)
5. G.Leibfried: Bestrahlungseffekte in Festkörpern (Teubner, Stuttgart 1965)
6. G.Carter, J.S.Colligon: The Ion Bombardment of Solids (Heinemann, London 1968)
7. I.M.Torrens: Interatomic Potentials (Academic Press, New York 1972)
8. P.Sigmund, Rev.Roum.Phys. 17(1972)823&969&1079
9. P.Sigmund in: Physics of Ionized Gases 1972, Hrsg. M.Kurepa (Inst. of Physics, Belgrade 1972)
10. P.Sigmund, K.B.Winterbon, Nucl.Instrum.Meth. 119(1974)541
11. H.Ryssel, I.Ruge: Ionenimplantation (Teubner, Stuttgart 1978)
12. Y.H.Ohtsuki: Charged Beam Interaction with Solids (Taylor&Francis, London 1983)
13. J.F.Ziegler (Hrsg.): The Stopping and Range of Ions in Solids (Pergamon Press, New York):
Vol.1: J.F.Ziegler, J.P.Biersack, U.Littmark: The Stopping and Range of Ions in Solids (1985)
Vol.2: H.H.Andersen: Bibliography and Index of Experimental Range and Stopping Power Data (1977)
Vol.3: H.H.Andersen, J.F.Ziegler: Hydrogen, Stopping Power and Ranges in All Elements (1977)
Vol.4: J.F.Ziegler: Helium, Stopping Power and Ranges in All Elements (1977)
Vol.5: J.F.Ziegler: Stopping Cross-Sections for Energetic Ions in All Elements (1980)
Vol.6: U.Littmark, J.F.Ziegler: Range Distributions for Energetic Ions in All Elements (1980)
14. R.Behrisch (Hrsg.): Sputtering by Particle Bombardment, (Springer, Heidelberg):
Vol.1: Physical Sputtering of Single-Element Solids (1981)
Vol.2: Sputtering of Multicomponent Solids and Chemical Effects (1983)
Vol.3: Characteristics of Sputtered Particles, Technical Applications (1991)
15. R.Kelly, M.F.da Silva (Hrsg.): Materials Modification by High-Fluence Ion Beams (Kluwer, Dordrecht 1989)
16. W.Eckstein: Computer Simulation of Ion-Solid Interactions (Springer, Berlin 1991)
17. W.Möller in: Vakuumbeschichtung 1, Hrsg. H.Frey (VDI-Verlag, Düsseldorf 1995)
18. M.Nastasi, J.K.Hirvonen, J.W.Mayer: Ion-Solid Interactions: Fundamentals and Applications (Cambridge University Press 1996)
19. J.F.Ziegler, The Stopping and Ranges of Ions in Matter ("SRIM-2000"), Computer software package. Can be downloaded via internet <http://www.SRIM.org>
20. H.E.Schiøtt, Kgl.Dan.Vid.Selsk.Mat.Fys.Medd. 35,9(1966)
21. K.Weissmann, P.Sigmund, Radiat.Effects 19(1973)7
22. P.Sigmund and A.Gras-Marti, Nucl.Instrum.Meth. 182/183(1981)25

Individual References

Individual references are incomplete. An extended version is in preparation and will be made available in 2013.

Contents

Literature.....	2
1. Binary Elastic Collisions in a Spherically Symmetric Potential.....	4
1.1 Kinematics.....	6
1.2 Cross Section.....	6
1.3 Example: Rutherford Scattering.....	6
1.4 Momentum Approximation.....	7
2. Atomic Potentials.....	8
2.1 Thomas-Fermi Statistical Model.....	8
2.2 Exchange and Correlation.....	9
2.3 Other Screening Functions.....	9
3. Interatomic Potentials.....	10
3.1 Linear Superposition of Atomic Electron Densities.....	10
3.2 Universal Approximation by Lindhard, Nielsen and Scharff (LNS).....	11
3.3 Individual Scattering Cross Sections.....	13
4. Classical and Quantum-Mechanical Scattering.....	14
4.1 The Bohr Criterion.....	14
4.2 Quantum-Mechanical Scattering Cross Section.....	16
5. Stopping of Ions.....	17
5.1 Effective Charge.....	17
5.2 Electronic Stopping – High Velocity.....	18
5.3 Electronic Stopping – Low Velocity.....	22
5.4 Electronic Stopping – Empirical Concepts.....	25
5.5 Nuclear Stopping.....	25
5.6 Stopping in Compound Materials.....	27
6. Energy Loss Fluctuations.....	28
6.1 Thickness Fluctuation.....	28
6.2 Charge State Fluctuation.....	28
6.3 Energy Transfer Fluctuation.....	29
7. Multiple Scattering.....	31
8. Ion Ranges.....	34
9. The Collision Cascade.....	36
10. Transport Equations Governing the Deposition of Particles and Energy.....	38
10.1 Primary Distributions.....	38
10.2 Distributions of Energy Deposition Including Collision Cascades.....	43
10.3 Cascade Energy Distribution.....	44
10.4 Spatial Cascade Energy Distribution.....	46
11. Binary Collision Approximation Computer Simulation of Ion and Energy Deposition.....	47
12. Radiation Damage.....	53
12.1 Analytical Treatment.....	53
12.2 TRIM Computer Simulation.....	56
13. Sputtering.....	57
13.1 Analytical Treatment.....	57
13.2 TRIM Computer Simulation.....	62
14. Thermal Spikes.....	63
15. High-Fluence Phenomena.....	66
15.1 Dynamic Binary Collision Approximation Computer Simulation.....	66
15.2 Local Saturation.....	67
15.3 Sputter-Controlled Implantation Profiles.....	69
15.4 Preferential Sputtering.....	71
15.5 Ion Mixing.....	74

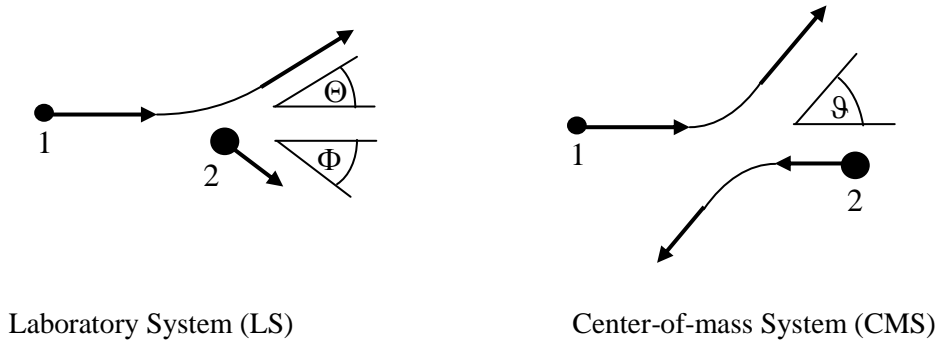
1. Binary Elastic Collisions in a Spherically Symmetric Potential

1.1 Kinematics

Both ion-atom and ion-electron collisions are treated as binary collisions. This sets a lower energy limit for the treatment of ion-atom collisions of 10...30 eV. Otherwise, many-body interactions would have to be taken onto account [16].

1 – projectile, 2 – target atom (at rest in laboratory frame)

Fig. 1.1



Transformation into CMS yields single-particle scattering kinematics

$$\mu \frac{d^2 \vec{R}}{dt^2} = -\vec{\nabla} V(\vec{R}), \quad \vec{R} = \vec{R}_1 - \vec{R}_2 \quad (1.1)$$

for a spherically symmetric interaction potential V and with the reduced mass

$$\mu = \frac{m_1 m_2}{m_1 + m_2} \quad (1.2)$$

The energy in the CMS system, being available for the collision, is given by

$$E_c = \frac{m_2}{m_1 + m_2} E \quad (1.3)$$

with E – projectile energy in LS.

Momentum and energy conservation yield the transformations of the asymptotic scattering angles between CMS and LS for an elastic collision

$$\tan \Theta = \frac{\sin \vartheta}{\frac{m_1}{m_2} + \cos \vartheta} \quad \Phi = \frac{\pi - \vartheta}{2} \quad (1.4)$$

and the reverse transformation

$$\vartheta = \Theta + \arcsin\left(\frac{m_1}{m_2} \sin \Theta\right) \quad (1.5)$$

The energy transferred to the target atom ("recoil") (in LS) is given by

$$T = \gamma E \sin^2 \frac{\vartheta}{2} \quad (1.6)$$

with the energy transfer factor

$$\gamma = \frac{4m_1m_2}{(m_1 + m_2)^2} \quad (1.7)$$

From this, the LS projectile energy after the collision becomes

$$E' = E - T = E \left(1 - \frac{4m_1m_2}{(m_1 + m_2)^2} \sin^2 \frac{\Theta}{2} \right) \quad (1.8)$$

or after transformation according to (1.4)

$$E' = E \left(\frac{m_1}{m_1 + m_2} \right)^2 \left(\cos \Theta \pm \sqrt{\left(\frac{m_2}{m_1} \right)^2 - \sin^2 \Theta} \right)^2 \quad (1.9)$$

Both (1.5) and (1.9) indicate the existence of a maximum scattering angle in LS

$$\Theta_{max} = \arcsin \left(\frac{m_2}{m_1} \right) \quad \text{if } m_1 \geq m_2 \quad (1.10)$$

For this case, both signs are valid in (1.9), so that two different energies correspond to any LS scattering angle below the maximum one.

Trivially, the recoil energy is

$$E'_2 = T = E - E' \quad (1.11)$$

Kinematical curves from (1.9) and (1.11) are shown in Fig. 1.2 for different ions, indicating a maximum LS scattering angle of 90° for the equal-mass case, and below for heavier projectiles.

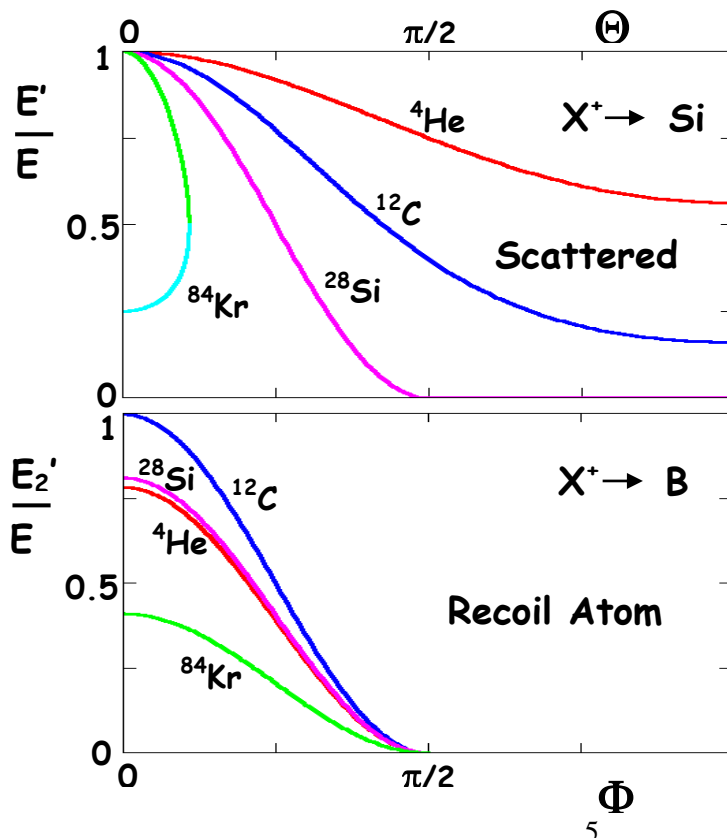


Fig. 1.2:

Kinematics of elastic scattering for the scattered projectile (different ions incident on silicon – top) and the recoil atom (different ions incident on boron – bottom)

1.2 Cross Section

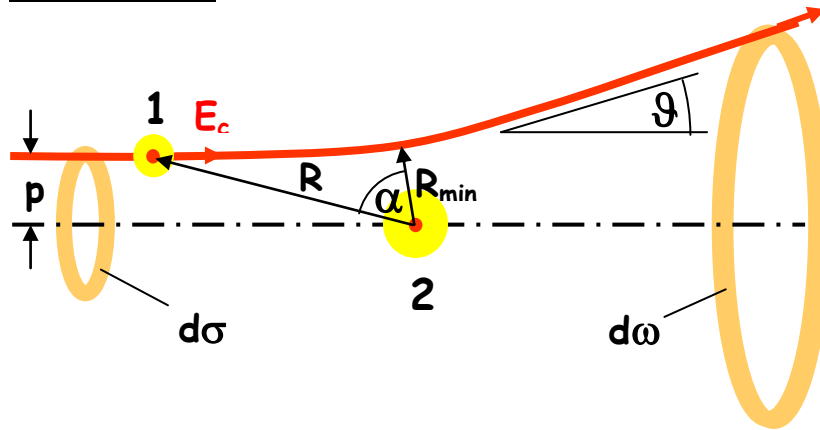


Fig. 1.3:

Scattering trajectory. Incidence within a differential ring at a given impact parameter results in a scattering into a differential solid angle

In cylindrical coordinates, the CMS trajectory is described by the distance R and the angle α (see Fig. 1.3). Energy and angular momentum conservation, and integration yield for the asymptotic scattering angle at a given impact parameter p the so-called "classical trajectory integral"

$$\vartheta = \pi - 2p \int_0^{R_{min}^{-1}} \frac{d\left(\frac{1}{R}\right)}{\sqrt{1 - \frac{V(R)}{E_c} - \frac{p^2}{R^2}}} \quad (1.12)$$

with the minimum distance of approach given by

$$\sqrt{1 - \frac{V(R)}{E_c} - \frac{p^2}{R_{min}^2}} = 0 \quad (1.13)$$

The differential cross section is given by the differential area at p and the scattering into the differential solid angle around the scattering angle

$$\frac{d\sigma}{d\omega} = \left| \frac{2\pi p dp}{2\pi \sin \vartheta d\vartheta} \right| = \left| \frac{p}{\sin \vartheta} \frac{dp}{d\vartheta} \right| \quad (1.14)$$

and can now be calculated from (1.12).

From (1.4), the transformation into the laboratory system is accomplished according to

$$\frac{d\sigma}{d\Omega} = \frac{d\sigma}{d\omega} \frac{d\omega}{d\Omega} = \frac{d\sigma}{d\omega} \frac{\left(\left(\frac{m_1}{m_2} + \cos \vartheta \right)^2 + \sin^2 \vartheta \right)^{3/2}}{1 + \frac{m_1}{m_2} \cos \vartheta} \quad (1.15)$$

1.3 Example: Rutherford Scattering

For a Coulomb potential between two interacting charges Q_1 and Q_2

$$V(R) = \frac{Q_1 Q_2 e^2}{4\pi\epsilon_0 R} \quad (1.16)$$

(1.12) yields

$$\tan \frac{\vartheta}{2} = \frac{b}{2p} \quad (1.17)$$

with the "collision diameter", i.e. the distance of minimum approach for ion-ion scattering at 180°

$$b = \frac{Q_1 Q_2 e^2}{4\pi\epsilon_0 E_c} \quad (1.18)$$

From this, the Rutherford cross section becomes

$$\frac{d\sigma}{d\omega} = \frac{b^2}{16} \frac{1}{\sin^4 \frac{\vartheta}{2}} \propto \frac{1}{E^2} \quad (1.19)$$

1.4 Momentum Approximation

Due to the cylindrical symmetry of the scattering problem, large impact parameters and correspondingly small deflection angles occur largely preferentially. Therefore, it is often convenient to describe the scattering in a small-angle approximation.

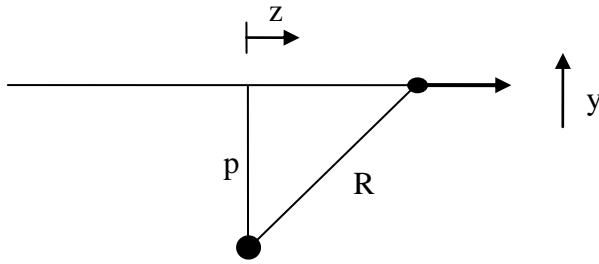


Fig. 1.4:

Momentum approximation for small-angle scattering

In the limit of forward scattering, the projectile trajectory is approximated by a straight line (see Fig. 1.4). A force integral leads to a small transverse momentum Δp_y and thereby a small deflection angle

$$\vartheta = \frac{\Delta p_y}{\sqrt{2\mu E_c}} = -\frac{2}{E_c} \frac{\partial}{\partial p} \int_{-\infty}^{+\infty} V(\sqrt{z^2 + p^2}) dz \quad (1.20)$$

(1.4) reads in small-angle approximation

$$\Theta = \frac{m_2}{m_1 + m_2} \vartheta \quad (1.21)$$

yielding directly (see (1.3)) the LS deflection which is independent on the mass of the target

$$\Theta = -\frac{2}{E} \frac{\partial}{\partial p} \int_{-\infty}^{+\infty} V(\sqrt{z^2 + p^2}) dz \quad (1.22)$$

2. Atomic Potentials

For the ion – target atom interaction with a sufficiently large minimum distance R_{\min} , the interatomic potential $V(R)$ is influenced by the presence of the electrons, so that a screened Coulomb potential has to be employed. Naturally, the development of proper interatomic potentials $V(R)$ is closely related to the choice of the atomic potentials of the collision partners.

The treatment of atomic potentials here will not cover quantum-mechanical calculations of the Hartree-Fock-Slater type, but be restricted to statistical models and analytical approximations for practical uses.

2.1 Thomas-Fermi Statistical Model

From simple quantum statistics in the free electron gas of density n_e , the mean kinetic energy density (i.e. the mean kinetic energy per unit volume) results as

$$\bar{\epsilon}_k = \frac{3}{10} (3\pi^2)^{2/3} \frac{e^2 a_0}{4\pi\epsilon_0} n_e^{5/3} =: \kappa_k n_e^{5/3} \quad (2.1)$$

with $a_0 = 0.053$ nm denoting the radius of the first Bohr orbit.

Treating the atom with atomic number Z as the nucleus and an assembly of local free electron gases, its electrostatic potential given by

$$\phi(\mathbf{r}) = \frac{Ze}{4\pi\epsilon_0 r} - \frac{e}{4\pi\epsilon_0} \int \frac{n_e(\mathbf{r}')}{|\mathbf{r} - \mathbf{r}'|} d^3\mathbf{r}' \quad (2.2)$$

A calculus of variation of the total energy

$$E_{tot} = \int \bar{\epsilon}_k d^3\mathbf{r} - \frac{Ze^2}{4\pi\epsilon_0} \int \frac{n_e(\mathbf{r})}{r} d^3\mathbf{r} + \frac{e^2}{8\pi\epsilon_0} \int \frac{n_e(\mathbf{r})n_e(\mathbf{r}')}{|\mathbf{r} - \mathbf{r}'|} d^3\mathbf{r}d^3\mathbf{r}' \quad (2.3)$$

with respect to the electron density yields

$$\frac{5}{3} \kappa_k n_e(r)^{2/3} - r(\phi(r) - \phi_0) = 0 \quad (2.4)$$

with an additive constant ϕ_0 . Self-consistency is provided by the Poisson equation

$$\Delta\Delta(\phi(r) - \phi_0) = \frac{e}{\epsilon\epsilon_0} n_e(r) \quad (2.5)$$

Combining (2.4) and (2.5) in spherical coordinates and writing the potential as a screened Coulomb potential according to

$$\phi(r) = \frac{Ze}{4\pi\epsilon_0 r} \varphi\left(\frac{r}{a}\right) \quad (2.6)$$

the substitution $r = ax$ yields for the screening distance

$$a = \frac{1}{2} \left(\frac{3\pi}{4} \right)^{2/3} \frac{a_0}{Z^{1/3}} = 0.8853 \frac{a_0}{Z^{1/3}} \quad (2.7)$$

and the Thomas-Fermi equation

$$\frac{d^2 \varphi_{TF}}{dx^2} = \frac{\varphi_{TF}^{3/2}}{x^{1/2}} \quad (2.8)$$

Eq. (2.8) is solved numerically with the boundary conditions

$$\varphi(0) = 1 \quad \varphi(\infty) = \varphi'(\infty) = 0 \quad (2.9)$$

as the Coulomb potential holds at small distance to the nucleus, and due to the neutrality of the whole atom.

The screening function is often approximated by a series of exponentials. The ‘‘Moliere’’ approximation to the TF function is valid for about $x < 5$:

$$\varphi_M(x) = \sum_i C_i e^{-c_i x} = 0.35e^{-0.3x} + 0.55e^{-0.2x} + 0.1e^{-6x} \quad (2.10)$$

2.2 Exchange and Correlation

Quantum-mechanical exchange and correlation have also been described within the framework of the statistical model, resulting in the following energy densities as function of the electron density:

$$\bar{\epsilon}_{ex} = -\left(\frac{3}{\pi}\right)^{4/3} \frac{e^2}{16\epsilon_0} n_e^{4/3} =: \kappa_{ex} n_e^{4/3} \quad (2.11)$$

$$\bar{\epsilon}_{corr} \approx -0.46 \frac{e^2}{4\pi\epsilon_0} n_e^{5/3} =: \kappa_{corr} n_e^{5/3} \quad (2.12)$$

2.3 Other Screening Functions

The variation problem mentioned above has been solved by Lenz and Jensen using a proper ansatz for the electron density with appropriate boundary conditions. The resulting screening function is

$$\varphi_{LJ}(x) = \left(1 + y + 0.3344 y^2 + 0.0485 y^3 + 0.002647 y^4\right) e^{-y}; \quad y = \sqrt{9.67 x} \quad (2.13)$$

The most simple screening function is a pure exponential according to Bohr:

$$\varphi_B(x) = e^{-y} \quad (2.14)$$

Lindhard has given an approximative, so-called ‘‘standard’’ potential

$$\varphi_{LS}(x) = 1 - \frac{x}{\sqrt{x^2 + 3}} \quad (2.15)$$

Finally, power-law approximations are used for different regions of x , of the form

$$\varphi_{PL}(x) = \frac{K_s}{s} \left(\frac{1}{x}\right)^{s-1} \quad (2.16)$$

corresponding to $\phi(r) \sim r^{-s}$.

Although the following “Universal” screening functions has been formulated for the interatomic potential (see 3.), it is included here for completeness:

$$\varphi_V(x) = 0.182e^{-3.2x} + 0.51e^{-0.942x} + 0.28e^{-0.403x} + 0.0282e^{-0.202x} \quad (2.17)$$

in this case with the screening distance

$$a_V = 0.8853 \frac{a_0}{Z^{0.23}} \quad (2.18)$$

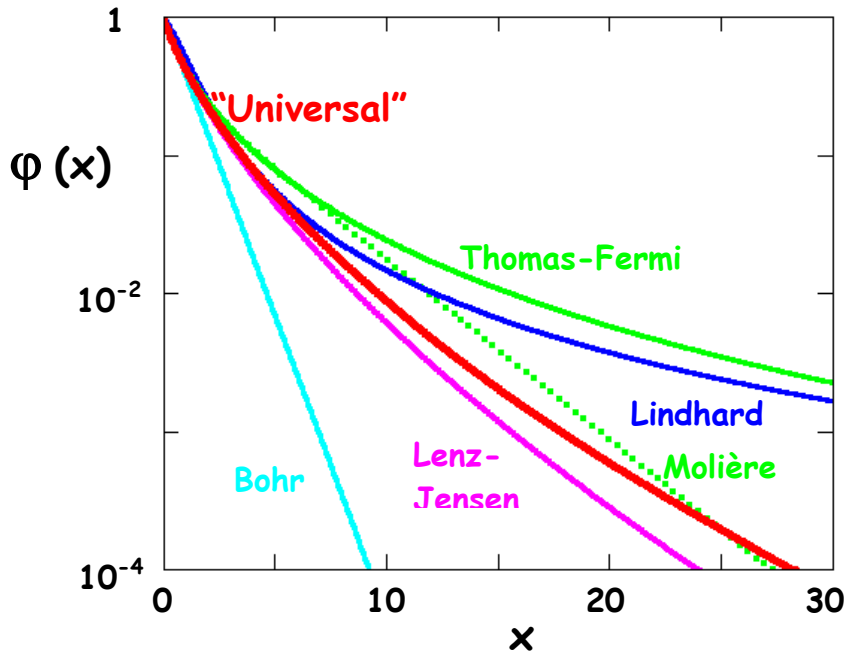


Fig. 2.1
Different atomic screening functions

3. Interatomic Potentials

The interaction potential of two fast atoms, each of which is individually represented by a screened Coulomb potential, can now be treated in an approximate way.

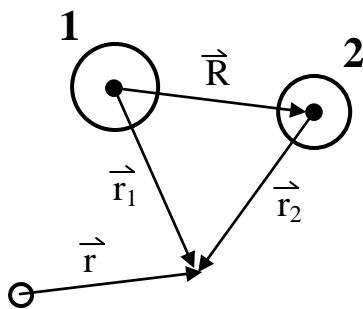


Fig. 3.1
Interatomic Coordinates

3.1 Linear Superposition of Atomic Electron Densities

A simple approach is the linear superposition of the individual electron densities to obtain the total electron density $n(r)$, i.e. neglecting any atomic rearrangements during the collision

$$n_e(\vec{r}) = n_{e1}(\vec{r}) + n_{e2}(\vec{r}) \quad (3.1)$$

Expressing the total energy (including Coulomb, kinetic, exchange and correlation terms according to sect. 2) as function of the distance R , and subtracting the total energies of the individual atoms yields the interaction potential

$$\begin{aligned}
V(R) = & \frac{Z_1 Z_2 e^2}{4\pi\epsilon_0 R} - \frac{e^2}{4\pi\epsilon_0} \int \left(\frac{Z_1}{r_1} n_{e2}(r_2) + \frac{Z_2}{r_2} n_{e1}(r_1) \right) d^3 r \\
& + \frac{e^2}{8\pi\epsilon_0} \iint \frac{n_{e1}(r_1) n_{e2}(r_2) + n_{e1}(r_1') n_{e2}(r_2)}{|\bar{r} - \bar{r}'|} d^3 r d^3 r' + \\
& + \kappa_{ex} \int \left((n_{e1}(r_1) + n_{e2}(r_2))^{4/3} - (n_{e1}(r_1))^{4/3} - (n_{e2}(r_2))^{4/3} \right) d^3 r \\
& + \kappa_{corr} \int \left((n_{e1}(r_1) + n_{e2}(r_2))^{5/3} - (n_{e1}(r_1))^{5/3} - (n_{e2}(r_2))^{5/3} \right) d^3 r
\end{aligned} \tag{3.2}$$

Eq. (3.2) has to be solved numerically for all R , from which the scattering cross section can be obtained according to eqs. (2.12-2.14). This is clearly a lengthy procedure and has to be repeated for each pair of atoms.

3.2 Universal Approximation by Lindhard, Nielsen and Scharff (LNS)

With the aim to obtain a simple and universal description of the interatomic potential and the scattering cross section of two fast atoms, LNS start from the atomic screened Coulomb potential (see sect. 2). In the limiting cases of $Z_1 \ll Z_2$ or $Z_1 \gg Z_2$, the interatomic potential would be correctly described by the screened Coulomb potential of one atom (eq. (2.6)), since the problem can be approximated by a point charge in the potential of the heavier atom, so that

$$V(R) = \frac{Z_1 Z_2 e^2}{4\pi\epsilon_0 R} \varphi\left(\frac{R}{a}\right) \tag{3.3}$$

with a properly chosen screening distance a . For the Thomas-Fermi screening function, the following choice represents the limits correctly:

$$a_{TF} = \frac{0.8853 a_0}{\left(Z_1^{2/3} + Z_2^{2/3} \right)^{1/2}} \tag{3.4}$$

For the "Universal" potential (see sect. 2), the screening distance reads correspondingly

$$a_U = \frac{0.8853 a_0}{Z_1^{0.23} + Z_2^{0.23}} \tag{3.5}$$

The other extreme is obviously the case of $Z_1 = Z_2$. For this situation, LNS evaluated (3.2) for a number of atoms and found a reasonable agreement with eqs. (3.3+3.4). Therefore, they assumed (3.3+3.4) to represent a good approximation of a universal interatomic interaction potential.

For the derivation of a universal scattering cross section, LNS consider the limit of small scattering angles given by the momentum approximation (1.19), which is evaluated for a screened Coulomb potential yielding

$$\mathfrak{D} = \frac{b}{p} g\left(\frac{p}{a}\right)$$

with b from eq. (1.17) and

(3.6)

$$g(\zeta) = \int_0^{\pi/2} \cos \eta \left[\varphi\left(\frac{\zeta}{\cos \eta}\right) - \frac{\zeta}{\cos \eta} \varphi'\left(\frac{\zeta}{\cos \eta}\right) \right] d\eta$$

Further, a reduced energy is introduced according to

$$\varepsilon = \frac{a}{b} = \frac{4\pi\varepsilon_0 a}{Z_1 Z_2 e^2} E_c \quad (3.7)$$

so that

$$\varepsilon \cdot \mathfrak{D} = \frac{a}{p} g\left(\frac{p}{a}\right) \quad (3.8)$$

represents the universal classical scattering integral in the small-angle approximation. In order to extrapolate this to wide angles, LNS substitute

$$\varepsilon \cdot \mathfrak{D} \Rightarrow 2\varepsilon \sin \frac{\mathfrak{D}}{2} \quad (3.9)$$

and introduce a reduced scattering angle by

$$t^{1/2} = \varepsilon \sin \frac{\mathfrak{D}}{2} \quad (3.10)$$

Therefore,

$$2t^{1/2} = \frac{a}{p} g\left(\frac{p}{a}\right) \quad (3.11)$$

becomes a universal scattering integral being valid for all angles. The inverse function of (3.11), $p(t^{1/2})$, yields the differential cross section according to $d\sigma = d(\pi p^2)$, which, according to LNS, is written as

$$\frac{d\sigma}{dt} = \pi a^2 \frac{f\left(t^{1/2}\right)}{2t^{3/2}} \quad (3.12)$$

with f to be calculated numerically from g. $f(t^{1/2})$ is defined in such a way that it becomes constant for a power law potential (see eq. (2.16)) with $s = 2$. Fig. 3.2 shows the scattering function f for different screening functions.

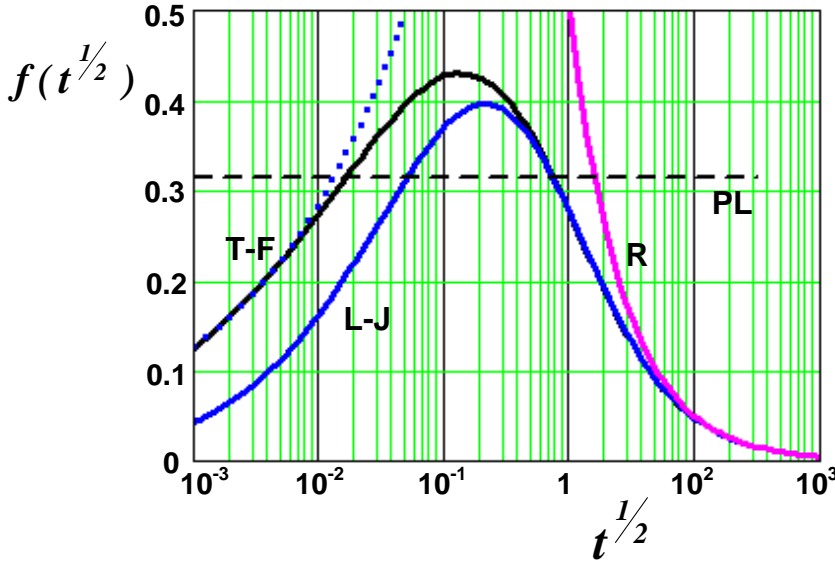


Fig. 3.2

Universal scattering function according to Lindhard, Nielsen, and Scharff, as function of the reduced scattering angle for pure Rutherford scattering (R), Thomas-Fermi (T-F), Lenz-Jensen (L-J), and power-law (PL; $s=2$, $k_s=0.8$) screening, and a low- t approximation to T-F screening according to $f(t^{1/2}) = 1.43 \cdot (t^{1/2})^{0.35}$ (dotted line)

From (3.12) and the transformation to the CMS scattering angle, the differential cross section becomes

$$\frac{d\sigma}{d\omega} = a^2 \frac{f(t^{1/2})}{8\epsilon \sin^3 \frac{\vartheta}{2}} \quad (3.13)$$

The evaluation of $f(t^{1/2})$ for the pure Coulomb potential yields

$$f_R(t^{1/2}) = \frac{1}{2t^{1/2}} \quad (3.14)$$

which, inserted into (3.13) and in comparison with (1.18), confirms that the LNS small-angle approximation holds exactly for all scattering angles in the limit of Rutherford scattering. Fig. 3.2 demonstrates that the scattering in the screened Coulomb potentials converges towards Rutherford scattering above $t^{1/2} \approx 10$.

In order to test the validity of the LNS small-angle approximation, the classical trajectory integral (1.12) can be evaluated for different ϵ , from which individual f -functions can be calculated. Fig. 3.3 shows that the error being introduced by the small angle approximation is rather small, except for very low energies.

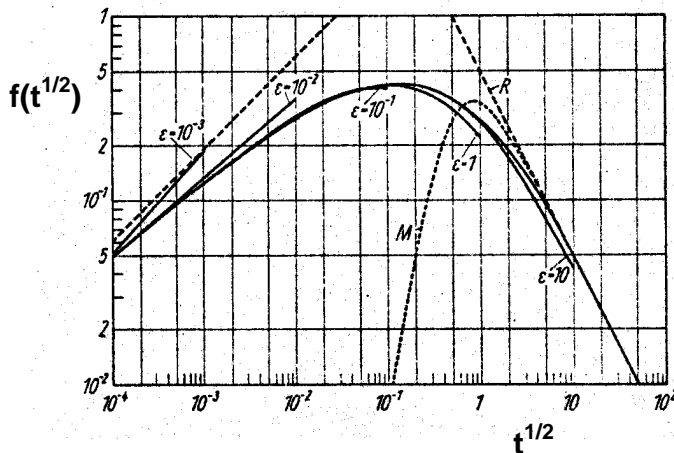


Fig. 3.3:

LNS scattering function f as function of t for Thomas-Fermi screening (continuous solid line), exact scattering functions for individual ϵ (solid lines), and several approximations (broken lines): Low- t approximation, Moliere approximation (M; eq. (2.10)), and Rutherford limit (R).

3.3 Individual Scattering Cross Sections

As compared to the LNS universal approximation, more precise interatomic scattering cross sections can, e.g., be obtained by evaluating eq. (3.2) for an individual pair of atoms. The example of Fig. 3.4, shows examples for the scattering of energetic argon ions in xenon gas. The scattering cross section has been evaluated both for two Lenz-Jensen atoms (see eq.(2.13)) and for electron densities from Dirac-Hartree-Fock-Slater quantum-mechanical calculations. The results are compared to the LNS universal formula for the Thomas-Fermi and the Lenz-Jensen potentials, and to experimental results. The quantum-mechanical prediction reproduces the position of shell oscillations as function of the scattering parameter, but underestimates their amplitude considerably.

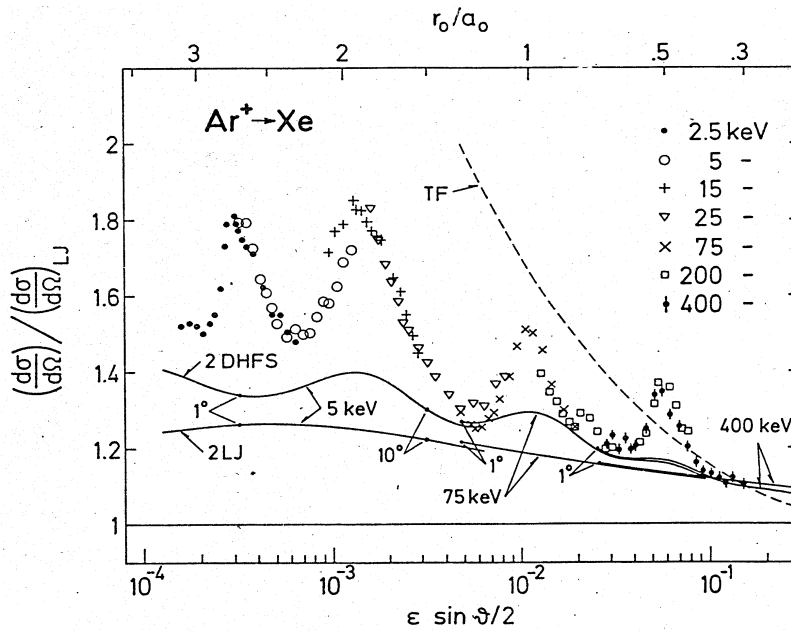


Fig. 3.4

Scattering cross sections, normalized to the universal LNS formula for the Lenz-Jensen (LJ) potential, versus the scattering parameter t . Experimental data for different ion energies and scattering angles are compared to the Thomas-Fermi (TF) universal LNS formula as well as to individual results for the superposition of two Lenz-Jensen (2LJ) and two DHFS atoms (2DHFS).

4. Classical and Quantum-Mechanical Scattering

The interaction of fast ions with matter may occur via atomic collisions, or by direct interaction with the bound electrons or the interstitial electrons of a solid. For the former, the scattering in an interatomic potential has to be treated as described in sects. 2 and 3, whereas the interaction with individual electrons is governed by the Coulomb potential. So far, classical trajectories have been assumed.

4.1 The Bohr Criterion

The validity of the classical scattering problem (sect. 1) is limited by the principle of uncertainty. In the quantum-mechanical picture, the incident particle with reduced mass μ in the CMS is represented by a plane wave with the wavelength

$$\lambda = \frac{\hbar}{\mu v} \quad (4.1)$$

with v denoting the ion velocity. (For a target at rest, the relative velocity in CMS is equal to the LS velocity). First considering the textbook example of slit interaction at a slit with width d , a classical trajectory calculation is feasible provided

$$\lambda \ll d \quad (4.2)$$

i.e. at sufficiently high velocity of the incident particle.

According to Bohr, a classical calculation can be performed provided the quantum-mechanical uncertainty of the scattering angle, $\Delta\vartheta$, is small compared to the scattering angle itself:

$$\Delta\vartheta \ll \vartheta \quad (4.3)$$

The uncertainty of the direction of a wave packet after scattering is composed from the uncertainty of the initial direction α and the impact parameter p (see Fig. 4.1). The uncertainty relation for the direction normal to the propagation reads

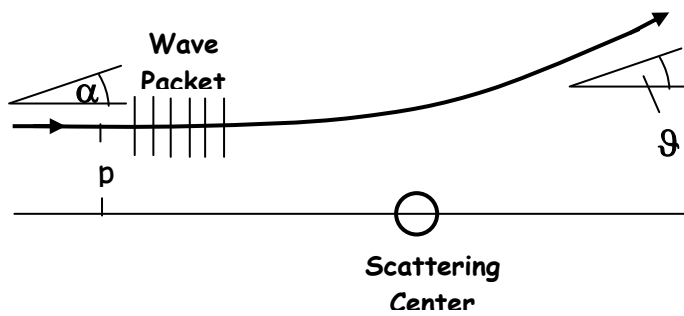


Fig. 4.1

Quantum-mechanical scattering geometry

$$\delta p \cdot \delta q_{\perp} \geq \frac{\hbar}{2} \quad (4.4)$$

with the uncertainty of the perpendicular momentum

$$\delta q_{\perp} = \mu v \delta \alpha \quad (4.5)$$

The uncertainty in p results in a partial uncertainty of ϑ . With independent contributions from the uncertainties in p and in δq_{\perp} , the total uncertainty becomes

$$(\Delta\vartheta)^2 = (\delta\alpha)^2 + \left| \frac{\partial\vartheta}{\partial p} \right|^2 (\delta p)^2 \quad (4.6)$$

Using the “=” sign in eq. (4.4) in order to calculate a minimum uncertainty, and minimizing $(\Delta\vartheta)^2$ as function of $(\delta p)^2$, the following condition for a classical trajectory calculation is obtained according to eq. (4.3):

$$\lambda \left| \frac{\partial}{\partial p} \left(\frac{1}{\vartheta(p)} \right) \right| \ll 1 \quad (4.7)$$

For a Coulomb potential, (4.7) can conveniently be evaluated for small scattering angles with $\vartheta = b/p$ according to (1.17), resulting in

$$\lambda \ll b \quad (4.8)$$

or the condition for the so-called “Bohr Kappa”

$$\kappa := \frac{2|Q_1 Q_2| e^2}{4\pi\epsilon_0 \hbar v} = 2|Q_1 Q_2| \frac{v_0}{v} \gg 1 \quad (4.9)$$

with v_0 denoting the velocity of the first Bohr orbit.

Eq. (4.8) demonstrates that the collision diameter b plays the role of the “slit” (see eq. (4.2)). However, as $b \sim v^{-2}$, the velocity dependence is just inverted: Classical trajectory calculations are feasible in the limit of low ion velocities.

For the interaction of an ion with an electron, the Bohr criterion reads

$$\kappa_e = 2Z_1 \frac{v_0}{v} \gg 1 \quad (4.10)$$

For the scattering in a screened Coulomb potential, or “nuclear” scattering, eq. (4.7) can, as an approximation, be evaluated for the Lindhard standard potential, eq. (2.15), in a small-angle approximation for distances large compared to a , resulting in

$$\kappa_n = 2Z_1 Z_2 \frac{v_0}{v} \gg 1 + \frac{p^2}{a^2} \quad (4.11)$$

that is, the Bohr criterion becomes dependent on the impact parameter.

4.2 Quantum-Mechanical Scattering Cross Section

In the quantum-mechanical picture, elastic ion scattering is described by the transition from an initial state $|i\rangle$ to a final state $|f\rangle$, both being represented by the particle at which the scattering occurs, and a plane wave for the incident and outgoing ion. In first Born approximation, the differential cross section results as

$$\frac{d\sigma_{if}}{d\omega} = \mu^2 \left(\frac{2\pi}{\hbar} \right)^4 \frac{v_f}{v_i} |\langle f | V | i \rangle|^2 \quad (4.12)$$

For elastic scattering, the scattering in a spherically symmetric potential results as

$$\frac{d\sigma}{d\omega} = \frac{\mu^2 \tilde{\lambda}^2}{\hbar^4} \frac{1}{\sin^2 \frac{\vartheta}{2}} \left| \int_0^\infty dr r V(r) \sin \left(\frac{2}{\tilde{\lambda}} r \sin \frac{\vartheta}{2} \right) \right|^2 \quad (4.13)$$

For a screened Coulomb potential with a Bohr screening function (eq. (2.14)), (4.13) can be conveniently evaluated resulting in

$$\frac{d\sigma}{d\omega} = \frac{b^2}{16} \frac{1}{\left(\sin^2 \frac{\vartheta}{2} + \left(\frac{\tilde{\lambda}}{2a} \right)^2 \right)^2} \quad (4.14)$$

which reproduces the Rutherford cross section in the limit of high velocity. In contrast to the Rutherford cross section, (4.14) can be integrated to obtain a total cross section

$$\sigma_{tot} = \int \frac{d\sigma}{d\omega} d\omega = \frac{\pi a^2 \kappa^2}{1 + \left(\frac{\lambda}{2a}\right)^2} \approx \pi a^2 \kappa^2 \quad (4.15)$$

as the second term in the denominator is negligible except for very low energies (around 1eV and less).

The validity of the first Born approximation requires a total cross section which is small compared to the characteristic atomic dimension, i.e. $\sim \pi a^2$. Therefore, according to (4.15), the first Born approximation would become questionable for low velocities with $\kappa \gg 1$. Therefore, the quantum-mechanical calculations are not feasible in this regime, and classical trajectory calculations are necessary. The Bohr criterion (4.9) delivers a unique limit between quantum-mechanical and classical calculations.

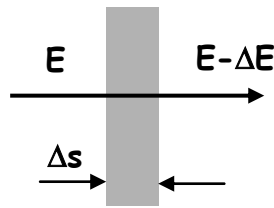


Fig. 5.1

Energy Loss

5. Stopping of Ions

When travelling along a path s through matter, an ion will continuously lose energy due to the interaction with electrons and screened nuclei. The energy loss per unit pathlength is denoted as “stopping power”:

$$B = -\frac{dE}{ds} \quad (5.1)$$

Often, the stopping is normalised to the atomic density n of the substance, resulting in the “stopping cross section”

$$S = -\frac{1}{n} \frac{dE}{ds} \quad (5.2)$$

where $n \cdot s$ is the number of atoms per unit area for a traversed pathlength s .

Although a correlation can be expected between the collisions with screened nuclei and the collisions with the electrons, as the local electron density depends on the impact parameter, “nuclear” or “elastic” interaction will be separated from the “electronic” or “inelastic” interaction in the following for simplicity. (It will turn out that the individual interactions are dominant in distinct ranges of energy, so that the approximation can be justified to some extent by the result.) Correspondingly, the total stopping is composed linearly from nuclear and electronic stopping:

$$S_{tot} = S_n + S_e \quad (5.3)$$

The stopping cross section can generally be written as

$$S = \int T d\sigma(T) \quad (5.4)$$

for an interaction with the differential cross section $d\sigma$ and the energy transfer T .

5.1 Effective Charge

In addition to stopping, the electronic interaction of an ion passing through matter results in charge-changing collisions, so that the actual charge state of a fast ion in matter is continuously fluctuating and determined by a balance between electron loss and electron attachment. The average charge of the ion, which depends on its velocity, is denoted as “effective” charge, Z_1^{eff} , and is quickly established (typically within some nm) when an ion of arbitrary charge state impinges onto a solid surface. In the limit of very low energy, the ion becomes neutral with a vanishing effective charge, so that atomic electrons interact with the electrons of the solid. Towards high velocities, electron loss dominates, so that the ions becomes a naked nucleus with $Z_1^{\text{eff}} = Z_1$ at sufficiently high energy.

More quantitatively, electron attachment is effective if the ion velocity is lower than the characteristic orbital velocity of its atomic electrons. Under this conditions, electrons from the electron gas of the solid have sufficient time to accommodate adiabatically with the moving ion. Taking the average velocity of electrons in a free electron gas with Z_1 electrons

$$\bar{v}_{e,I} \approx v_0 Z_1^{2/3} \quad (5.5)$$

as the characteristic velocity, Bohr has estimated the effective charge of the ion by

$$Z_1^{\text{eff}} \approx Z_1 \frac{v}{\bar{v}_{e,I}} = \frac{v}{v_0} Z_1^{1/3} \Rightarrow Z_1 \left(1 - \exp\left(-\frac{v}{v_0} Z_1^{-2/3}\right) \right) \quad (5.6)$$

with a high-velocity extrapolation that ascertains that Z_1^{eff} cannot exceed Z_1 .

5.2 Electronic Stopping – High Velocity

For $v \gg v_0 Z_1^{2/3}$, corresponding to $E \gg 25 \text{ keV} \cdot A_1 Z_1^{4/3}$ where A_1 denotes the atomic mass of the projectile, the ion is deprived of all its electrons. Then, the evaluation of (4.10) yields for the interaction with electrons ($|Q_2|=1$):

$$\kappa_e \ll 2Z_1^{1/3} \quad (5.7)$$

which does in general not fulfil the Bohr condition for classical trajectory calculations. Therefore, quantum-mechanical calculations have to be applied in general. For very heavy ions, however, an approximation by classical mechanics might become more feasible.

Both therefore and in order to discuss some physical concepts which will enter the classical calculation, we will start here with the latter, though being aware of the fact that it is not justified in principle.

The evaluation of (5.4) for Rutherford scattering of the ion free electrons yields

$$S_e = \frac{4\pi e^4}{(4\pi\epsilon_0)^2} \frac{Z_1^2 Z_2}{m_e v^2} \log\left(\frac{2p_{\max}}{b_e}\right) \quad (5.8)$$

with m_e denoting the electron mass and b_e the electronic collision diameter (eq. (1.18)). A difficulty in evaluating the stopping cross section arises from the fact that $d\sigma \sim T^{-2}$ according to eqs. (1.6) and (1.19), so that the integral diverges with a lower limit $T \rightarrow 0$. Therefore, a lower limit T_{\min} has to be introduced corresponding to a maximum impact parameter p_{\max} , which appears in (5.8).

An estimation of p_{max} is obtained by the so-called ‘‘adiabatic cutoff’’. Assuming a characteristic time interval τ of the interaction, the electrons of a target atom contribute to energy loss only if their mean orbital frequency ω is small compared to the inverse of the characteristic collision time. Otherwise, at large orbital frequencies, the electron would attach adiabatically to the moving ion.

Using the momentum approximation (eq. (1.21)), the characteristic collision time can be estimated from the transverse momentum transfer and its associated force integral to be

$$\tau \approx \frac{4p}{v} \quad (5.9)$$

so that the integration is limited to a maximum impact parameter

$$p_{max} \approx \frac{v\tau_{max}}{4} \approx \frac{v}{4} \frac{2\pi}{\omega} \approx \frac{v}{\omega} \quad (5.10)$$

Then, the result becomes (the classical ‘‘Bohr’’ formula)

$$S_e = \frac{4\pi e^4}{(4\pi\epsilon_0)^2} \frac{Z_1^2 Z_2}{m_e v^2} \log\left(\frac{4\pi\epsilon_0 m_e v^3}{Z_1 e^2 \omega}\right) \quad (5.11)$$

In the classical picture, the energy dependence of the electronic stopping reads as $\sim E^{-1} \log(CE^{3/2})$, C being a constant.

Now we will turn to the quantum-mechanical derivation of high-energy electronic stopping, which is imposed by the Bohr criterion.

The ion is represented by an initial and a final plane wave (see Fig. 5.2). The total initial and final states are

$$|i\rangle = |v_i\rangle (2\pi)^{-\frac{3}{2}} \exp(-ik_i \bar{r}) \quad |f\rangle = |v_f\rangle (2\pi)^{-\frac{3}{2}} \exp(-ik_f \bar{r}) \quad (5.12)$$

where $|v_i\rangle$ and $|v_f\rangle$ denote the initial and final state of the target atom, respectively, and k_i and k_f the wave vector of the ingoing and outgoing plane wave, respectively.

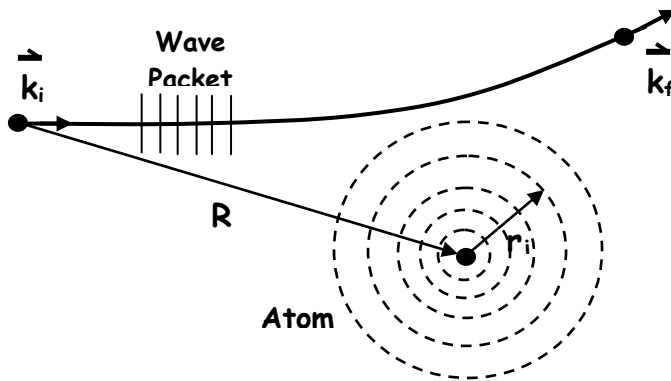


Fig. 5.2

Quantum-mechanical scattering coordinates

With ϵ denoting the total energy of the atom, the stopping cross section becomes according to (5.4)

$$S_e = \sum_f \int \frac{d\sigma_{if}}{d\omega} (\epsilon_f - \epsilon_i) d\omega \quad (5.13)$$

Into (5.13), eq. (4.12) has to be inserted with $\mu = m_e$ and the interaction potential

$$V(\vec{R}, \vec{r}_1, \dots, \vec{r}_{Z_2}) = -\frac{Z_1 e^2}{4\pi\epsilon_0} \left(\sum_{i=1}^{Z_2} \frac{1}{|\vec{R} - \vec{r}_i|} - \frac{Z_2}{R} \right) \quad (5.14)$$

With the momentum transfer

$$\vec{q} = \vec{k}_i - \vec{k}_f \quad (5.15)$$

the intermediate result is

$$S_e = \frac{8\pi e^4}{(4\pi\epsilon_0)^2} \frac{Z_1^2}{\hbar v^2} \sum_f \int_{q_{min}}^{q_{max}} \frac{dq}{q^3} (\epsilon_f - \epsilon_i) \left| \left\langle \mathbf{v}_f \left| \sum_i \exp(i\vec{q}\vec{r}_i) \right| \mathbf{v}_i \right\rangle \right|^2 \quad (5.16)$$

From energy conservation, maximum and minimum momentum transfer for a given final state are

$$q_{min} = \frac{\epsilon_f - \epsilon_i}{v} \quad q_{max} = \frac{2m_e v}{\hbar} \quad (5.17)$$

for a maximum energy transfer large compared to the binding energy of the electron.

For simplicity, Hartree wave functions

$$|\mathbf{v}\rangle = \prod_{i=1}^{Z_2} \varphi_i(\vec{r}_i) \quad (5.18)$$

with the individual orbital wave functions φ_i shall be employed intermediately. (However, the following finding also hold for more realistic total wave functions.) Then, the matrix element of (5.17) becomes

$$\left\langle \mathbf{v}_f \left| \sum_i \exp(i\vec{q}\vec{r}_i) \right| \mathbf{v}_i \right\rangle = \sum_i \int d^3\vec{r}_1 \varphi_{1f}^* \varphi_{1i} \bullet \dots \bullet \int d^3\vec{r}_i \varphi_{if}^* \varphi_{ii} \exp(i\vec{q}\vec{r}_i) \bullet \dots \bullet \int d^3\vec{r}_{Z_2} \varphi_{Z_2f}^* \varphi_{Z_2i} \quad (5.19)$$

Due to the orthonormality of the φ_i , (5.19) is only different from zero if exactly one electronic state (e.g., numbered j) is altered during the collision: Within the first Born approximation, multiple electronic excitation or ionisation is excluded. The matrix element is reduced to

$$\left\langle \mathbf{v}_f \left| \sum_i \exp(i\vec{q}\vec{r}_i) \right| \mathbf{v}_i \right\rangle = \int d^3\vec{r}_j \varphi_{jf}^* \varphi_{ji} \exp(i\vec{q}\vec{r}_j) \quad (5.20)$$

to be integrated over the atomic volume. For a characteristic radius a of the atom, the evaluation of (5.20) can be discriminated. If the momentum transfer is large compared to the inverse of the atomic radius, the exponential term oscillates quickly, and the matrix element only vanishes if

$$\varphi_{jf}(\vec{r}_j) \sim \exp(-i\vec{q}\vec{r}_j) \quad \text{for } q > \frac{1}{a} \quad (5.21)$$

i.e., the final state of the electron j is a plane wave. This situation stands for the ionisation of the atom, with

$$\varepsilon_f - \varepsilon_i = \frac{\hbar^2 q^2}{2m_e} \quad (5.22)$$

The contributions to the summation over ε_f and the integration over q in eq. (5.16) are indicated schematically in the two-dimensional plot of Fig. 5.3. For $q < 1/a$, the individual energy levels of the atoms are involved in electronic excitation. (5.16) can now be evaluated individually for the different regimes of q . For $q > 1/a$, the integrand can be converted into generalised oscillator strengths, which

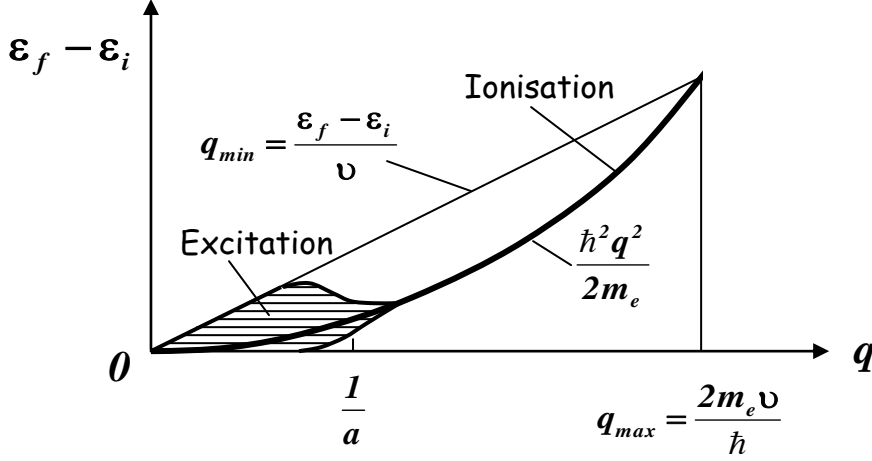


Fig. 5.3

Contributions to the stopping power integral

drop out due to their normalisation. For $q < 1/a$, the exponential of (5.20) is expanded to first order, which leads to dipole oscillator strengths f_{fi} . Adding the expressions for both regimes, the final result is the Bethe formula

$$S_e = \frac{4\pi e^4}{(4\pi\epsilon_0)^2} \frac{Z_1^2 Z_2}{m_e v^2} \log\left(\frac{2m_e v^2}{I}\right) \quad (5.23)$$

with the “mean ionisation potential” given by

$$\log I = \sum_f f_{fi} \log \hbar(\varepsilon_f - \varepsilon_i) \quad (5.24)$$

Due to the summation over all possible final states of the excited atom, I cannot readily be calculated. A reasonable approximation is according to Bloch

$$I \approx 10 \text{ eV} \cdot Z_2 \quad (5.25)$$

It should be noted that the quantum-mechanical result (5.23) differs from the classical one (5.11) only in the logarithmic terms which varies slowly with energy, anyway.

Two examples are given in Figs. 5.4a and 5.4b. In the limit of very high energy, both the classical and the quantum-mechanical formula are in good agreement with the experimental data. In the light-ion case, the Bethe formula works well for $\kappa \gg 1$. However, also the classical result is a rather good approximation even for the unsuitable energy regime. For heavy ions, quantum-mechanical calculations are only feasible for extremely high energy, and the classical picture holds well at sufficiently high energy.

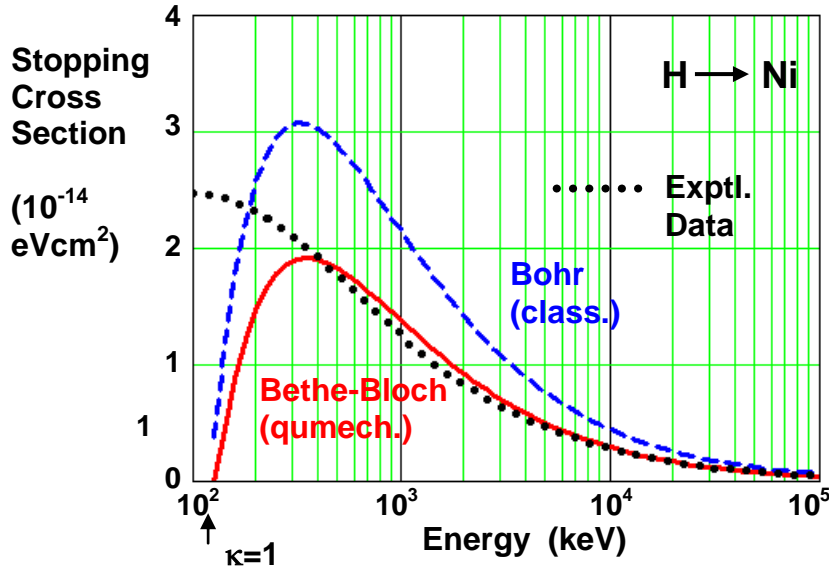


Fig. 5.4a

High-energy electronic stopping of a proton in Ni from (5.23) and (5.25) (Bethe-Bloch) and (5.11) (Bohr) with a mean orbital energy according to (5.25). The predictions are compared to semi-empirical data from the SRIM-2000 package. The energy of the Bohr criterion is indicated at the lower left.

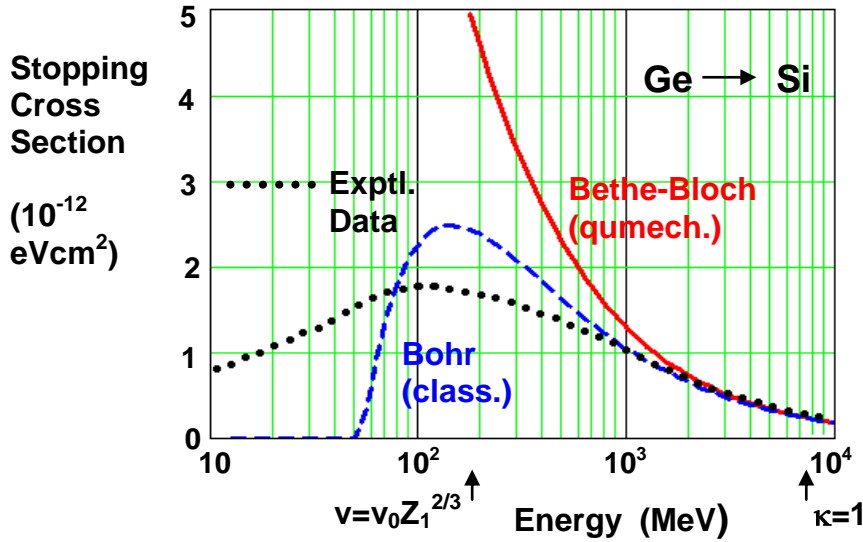


Fig. 5.4b

As 5.4a, but for germanium ions in silicon. Note the different scales. The low-velocity limit is also indicated.

For completeness, it should briefly be mentioned the high-velocity electronic energy loss can also be derived from the dynamic polarisation of a free electron gas, and the corresponding retarding drag on the ion (Lindhard and Winter). Again a result similar to (5.23) is obtained. The comparison yields in this case

$$I = \frac{1}{Z_2} \int 4\pi r^2 dr n_e(r) \log(\sqrt{2}\hbar\omega_0(r)) \quad (5.26)$$

Thus, the mean ionisation potential can be calculated more easily from realistic local radial electron densities n_e and the corresponding plasma frequencies ω_0 .

5.3 Electronic Stopping – Low Velocity

At low velocity with $v < v_0 Z_1^{2/3}$, the combination with the effective charge (eq. (5.6)) yields

$$\kappa_e \approx 2Z_1^{1/3} > 1 \quad (5.27)$$

so that classical trajectory calculations are feasible. In the following, we consider the interaction of the ion with the target electrons modelled as a free electron gas. By the scattering events with its electrons, momentum is transferred to the ion. The stopping cross section can be written in terms of the change of the longitudinal momentum, p_{\parallel} , per time unit:

$$S_e = -\frac{1}{2m_e n} \frac{d(p_{\parallel}^2)}{v dt} = -\frac{1}{n} \frac{dp_{\parallel}}{dt} \quad (5.28)$$

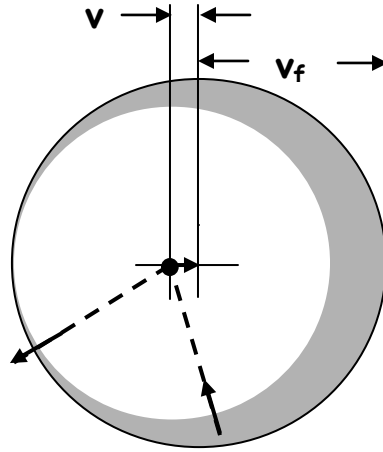


Fig. 5.4

Fermi sphere of the target free electron gas with Fermi velocity v_f , in the frame of an ion moving with small velocity v . The dashed trajectory indicates an electronic scattering event which is not forbidden by the Pauli principle.

For low ion velocities being small compared to the Fermi velocity of the electron gas, which is given by

$$v_f = \frac{\hbar}{m_e} (3\pi^2 n_e)^{1/3} \quad (5.29)$$

for a free electron gas, the Fermi sphere of the target electrons is slightly shifted in the frame of the ion (see Fig. 5.4). According to the Pauli principle, electrons can only transfer momentum to the ion when their final state lies in a previously unoccupied position beyond the original Fermi sphere. This is possible for electrons being positioned outside of a sphere with radius $v_f - v$, as indicated by the shaded area in Fig. 5.4. Its volume is about $4\pi v_f^2 v$. The velocity of the contributing electrons can be approximated by v_f , and the momentum transfer per scattering event is in the order of $m_e v_f$. A simple estimation then shows according to (5.28)

$$S_e \approx m_e Z_2 v v_f \sigma(v_f) \quad (5.30)$$

with the ion-electron scattering cross section σ . As an important result, the stopping cross section is proportional to the ion velocity, due to the Pauli principle.

A more rigorous treatment of the scattering geometry yields, still in the limit $v \ll v_f$

$$S_e = m_e Z_2 v v_f \sigma_{tr}(v_f) \quad (5.31)$$

where σ_{tr} denotes the so-called transport cross section given by

$$\sigma_{tr}(v) = \int_0^\pi (1 - \cos \vartheta) \frac{d\sigma}{d\omega}(v) d\omega \quad (5.32)$$

The evaluation of the differential cross section is rather complex and has to be performed for realistic local electron densities $n_e(r, Z_1, Z_2)$. Lindhard and Scharff arrive at

$$S_e = \frac{8\pi e^2 a_0}{4\pi\epsilon_0} \frac{Z_1^{7/6} Z_2}{(Z_1^{2/3} + Z_2^{2/3})^{3/2}} \frac{v}{v_0} =: k_e \sqrt{E} \quad (5.33)$$

where k_e is a constant defined by eq. (5.33). The result implicitly assumes that the electronic stopping acts nonlocally, i.e. independent of the actual position of the ion trajectory with respect to the position of the atoms which are passed by. Therefore, the result is independent of the actual impact parameter for a specific collision.

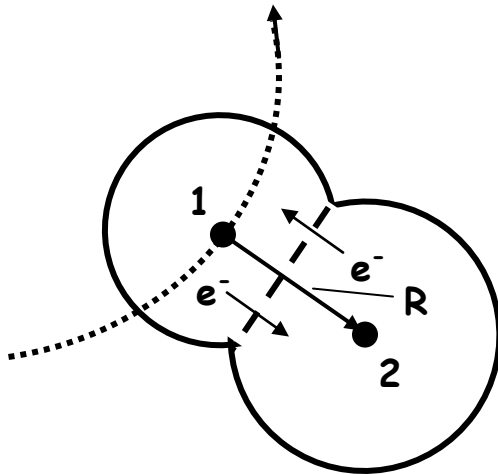


Fig. 5.5

Electronic energy loss in the Firsov picture

A different approach has been described by Firsov. During the interaction of two atoms, the electron clouds penetrate each other. Electrons transverse the intersecting plane between the two atoms, and, as $v \ll v_f$, accommodate their original directed kinetic energy (for both atoms moving in the CM system) to the dynamic electronic configuration of the interatomic system. For a free electron gas and a Thomas-Fermi interaction potential Firsov obtains for the electronic energy transfer per atomic collision

$$T_e = \frac{0.35}{a_0} \frac{(Z_1 + Z_2)^{5/3} \hbar v}{\left(1 + 0.16(Z_1 + Z_2)^{1/3} \frac{p}{a_0}\right)^5} \quad (5.34)$$

which offers the possibility to compute the energy loss as function of the impact parameter, with a very steep decrease as function of p for $p \gg a_0$. The integration over p yields in good approximation

$$S_e = 5.15 \cdot 10^{-15} (Z_1 + Z_2) \frac{v}{v_0} \text{ eV cm}^2 \quad (5.35)$$

Fig. 5.6 gives an example of low-energy electronic cross sections according to (5.33) and (5.35), in comparison to experimental values. The average agreement is good, however there are clear shell oscillations which cause significant deviations from the free-electron gas pictures.

For practical purposes in particular in connection with computer simulation, Oen and Robinson proposed an alternative expression for the local energy transfer (see eq. (5.34)):

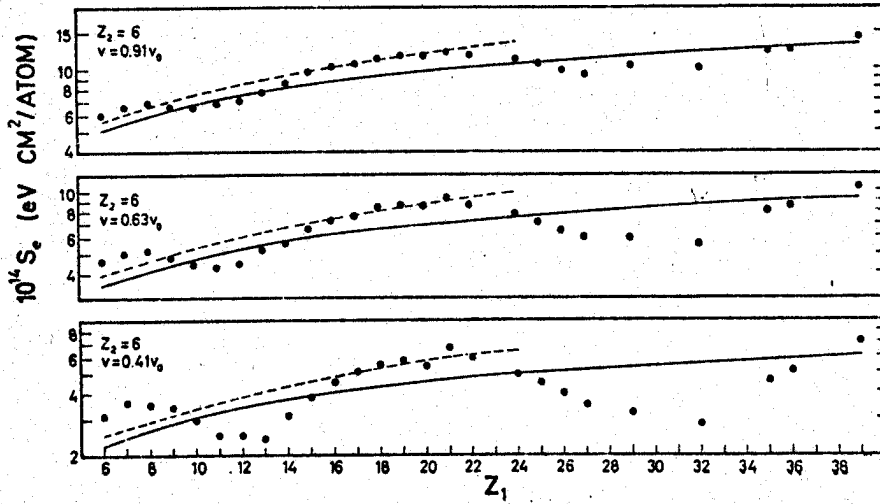


Fig. 5.6

Low-energy electronic stopping according to Lindhard and Scharff (solid lines) and Firsov (dashed lines) for different ions at three different velocities in a carbon film, compared to experimental data (dots)

$$T_e = \frac{c_1^2}{2\pi a^2} \exp\left(-c_1 \frac{R_{\min}(p)}{a}\right) k_e \sqrt{E} \quad (5.36)$$

where c_1 is the decay constant of the leading term of the exponential series approximation of the screening function (see eqs. (2.10) and (2.17)) and R_{\min} the minimum distance of approach (see eq. (1.13)). Integration of (5.36) yields the Lindhard-Scharff electronic stopping cross section (eq. (5.33)) in good approximation.

5.4 Electronic Stopping – Empirical Concepts

As seen above, the electronic stopping can be reasonably well described in the limits of high and low energies. The intermediate regime around $v = v_0 Z_1^{2/3}$ is very complex, in particular due to electron loss and attachment (see sect. 5.2). A formal approximation for this regime can be obtained by inverse interpolation

$$\frac{1}{S_e} = \frac{1}{S_e(\text{high } v)} + \frac{1}{S_e(\text{low } v)} \quad (5.37)$$

with a suitable low-velocity extrapolation (towards infinity as $v \rightarrow 0$) of the monotonically decreasing part of the above high-velocity results. Then, (5.37) reproduces the limiting low-velocity and high-velocity regimes correctly. Fig. 5.7 demonstrates a reasonable agreement with experimental data.

Interpolation formulas similar to (5.37) with proper parameterisation of the low- and high-energy formulas have been fitted to experimental data and are available in stopping tabulations (Ziegler, Andersen et. al.). A more elaborate concept (Ziegler et al.) makes additionally use of an effective-charge concept (see sect. 5.2) for a low-velocity extrapolation of the high-velocity electronic stopping. From this and the fit to many experimental data, universal semi-empirical electronic stopping power data are available from the SRIM package[19]. Specific data are shown in Figs. 5.4, 5.7 and 5.9.

5.5 Nuclear Stopping

The definition of a reduced, dimensionless pathlength according to LNS,

$$\rho = \pi a^2 n \frac{4m_1 m_2}{(m_1 + m_2)^2} \cdot s \quad (5.38)$$

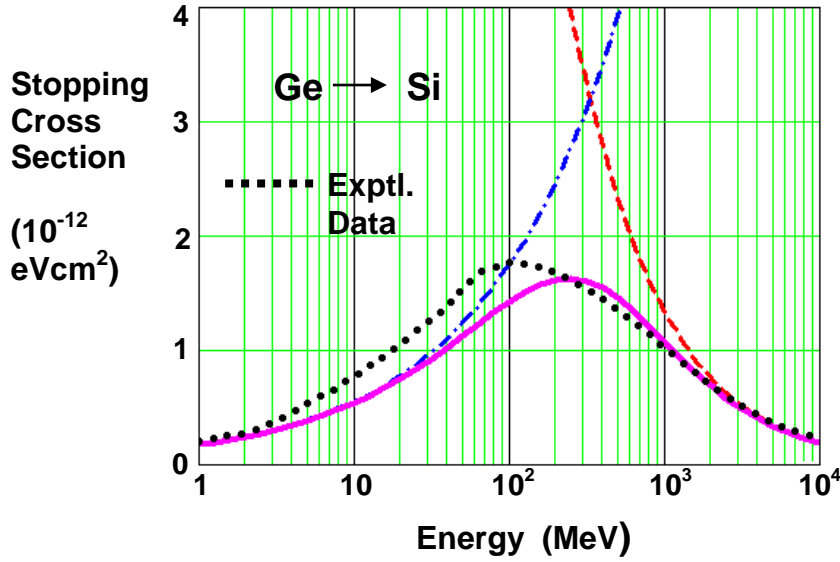


Fig. 5.7

Interpolation (solid line) of electronic stopping from the low-velocity regime (eq. (5.33), dashed-dotted line) and the high-velocity regime (eq. (5.23), dashed line) according to eq. (5.36), in comparison to semi-empirical data from the SRIM package.

yields directly a universal formula for the nuclear stopping power in reduced LNS units, making use of the universal scattering function for a screened Coulomb potential:

$$\left(-\frac{d\varepsilon}{d\rho}\right)_n = \frac{I}{\varepsilon_0} \int_0^\varepsilon f(t^{1/2}) d(t^{1/2}) \quad (5.39)$$

For the Thomas-Fermi screening function, Matsunami has given a good analytical approximation:

$$\left(-\frac{d\varepsilon}{d\rho}\right)_n = \frac{3.44\sqrt{\varepsilon} \log(\varepsilon + 2.718)}{1 + 6.35\sqrt{\varepsilon} + \varepsilon(6.882\sqrt{\varepsilon} - 1.708)} \quad (5.40)$$

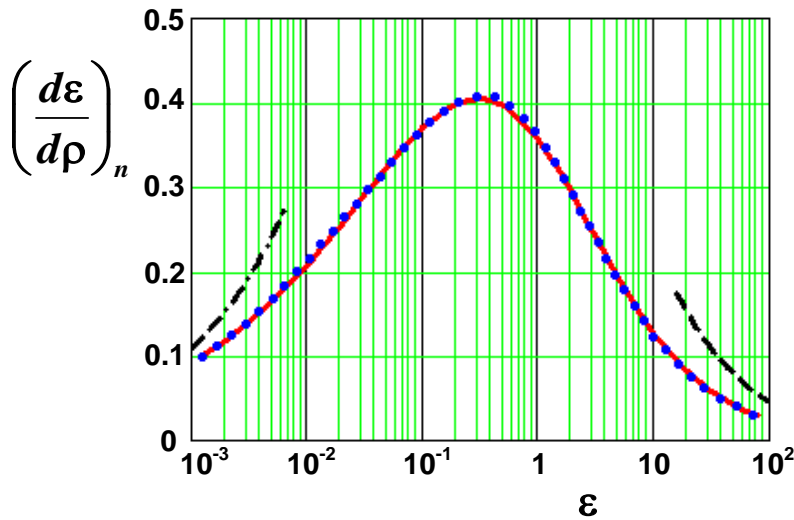


Fig. 5.8

Reduced nuclear stopping power as function of the reduced energy for Thomas-Fermi screening according to (5.39) (solid line) and the Matsunami approximation (5.40) (dotted line), with high- and low-energy limits (dashed-dotted and dashed line, respectively)

Eq. (5.40) shows that nuclear stopping, like electronic stopping, is proportional to the ion velocity in the limit of low velocity. At very high energy, it is proportional to $\varepsilon^{-1} \cdot \log(\varepsilon)$, which is just the energy scaling of electronic stopping. Fig. 5.8 shows the universal nuclear stopping together with these limits.

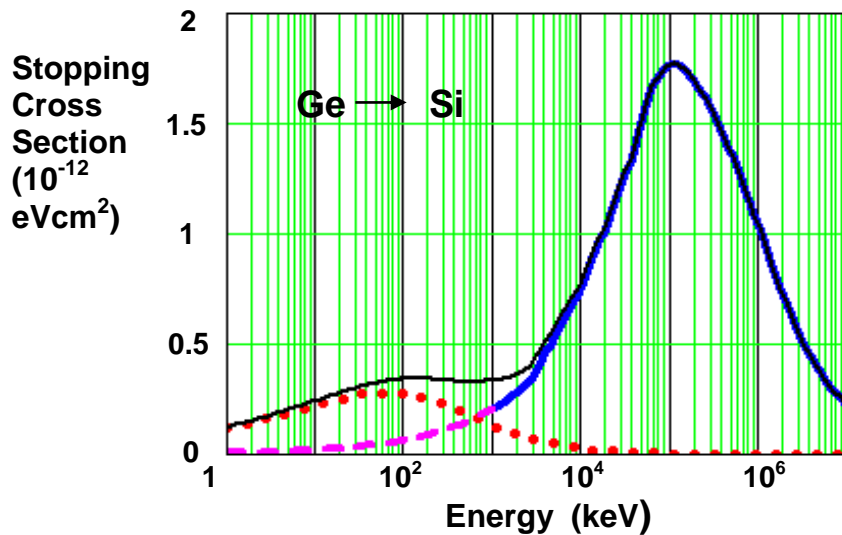


Fig. 5.9a

Nuclear (eq.(5.40), dotted line), electronic (SRIM package, solid line, and eq.(5.33), corrected by fitting factor of 1.2, dashed line) and total stopping (thin solid line) cross section versus ion energy, for germanium in silicon.

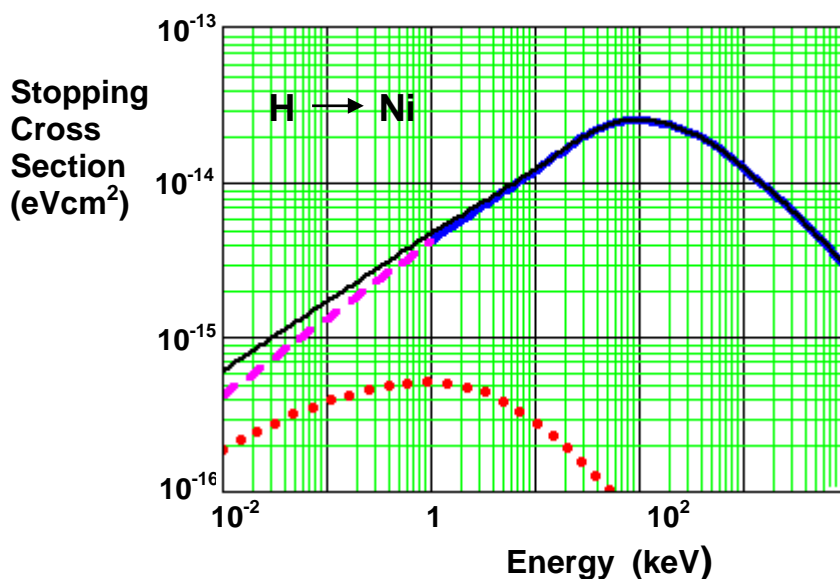


Fig. 5.9b

As Fig. 5.9a, but for hydrogen in nickel. The Lindhard-Scharff electronic stopping has been corrected by a fitting factor of 1.3. Note the different scales.

Figs. 5.9a+b show the nuclear stopping cross section S_e , which is transformed from (5.40) to non-reduced energy and pathlength, in comparison to the electronic cross section. For heavier ions, nuclear stopping dominates at low energy and becomes negligible in the limit of high energy. This is a further justification of the independent treatment of electronic and nuclear interaction. For very light ions, nuclear stopping can be neglected in a broad range of energies.

5.6 Stopping in Compound Materials

The simplest approximation to the stopping in compound materials is the summation of the pure element stopping cross sections. Thus, for a two-component material A_nB_m with the elemental stopping cross section S_A and S_B , the stopping cross section is according to “Bragg’s Rule”

$$S_{A_nB_m} = nS_A + mS_B \quad (5.41)$$

By the simple linear superposition, chemical interaction of the elements are neglected. Nevertheless, Bragg’s rule normally holds rather well. With increasing amount of covalent bonding in the compound, deviation of up to about 40% are observed, as, e.g., for oxides and hydrocarbons. For a number of compounds, stopping data are available in the SRIM package[19].

6. Energy Loss Fluctuations

In addition to the mean energy loss which is described by the stopping power, the energy distribution of an ion beam is broadened after traversing a sheet of thickness Δx (see Fig. 5.1)). This is shown schematically in Fig. 6.1. There are various reasons for energy loss fluctuations, which are partly “immanent”, i.e. connected to the statistical nature of the collisions which result in energy loss. However, in an experiment, additional contributions are observed and may obscure the immanent mechanisms, such as thickness variations of a foil or the influence of target crystallinity and/or texture. Here, we will remain in the frame of a random substance, and address the most important mechanisms.

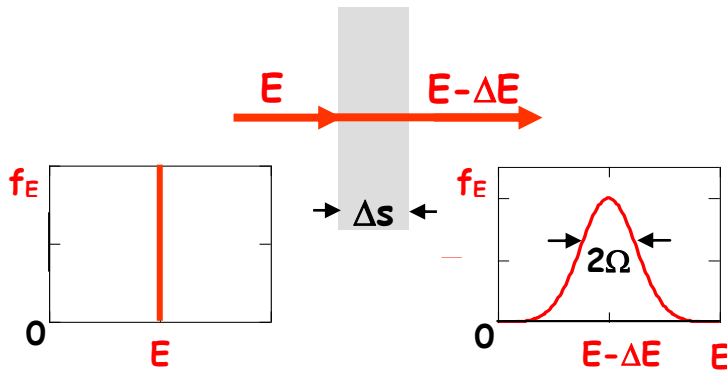


Fig. 6.1

Schematic showing the broadening of the energy distribution of an ion beam after passing through a thin sheet of matter

6.1 Thickness Fluctuation

When a thin film of thickness x with a mean square variation δx is traversed, the resulting variance of the ion energy distribution is

$$\Omega_{th}^2 = \left(-\frac{dE}{dx} \right)^2 \delta x^2 \quad (6.1)$$

that is, the width of the resulting energy distribution is proportional to the stopping power.

6.2 Charge State Fluctuation

As discussed in sect. 5.1, ions with intermediate energies undergo charge change collisions, so that they exhibit different charge states during their transport through matter. In the energy range of interest, the cross sections of charge-changing collisions are smaller than those of the atomic collision which determine the energy loss. Thus, as shown in Fig. 6.2 for the simplified case of only two different charge states, a fraction α of the total pathlength would be spent with one of the charge states, and the remaining fraction with the other charge state.

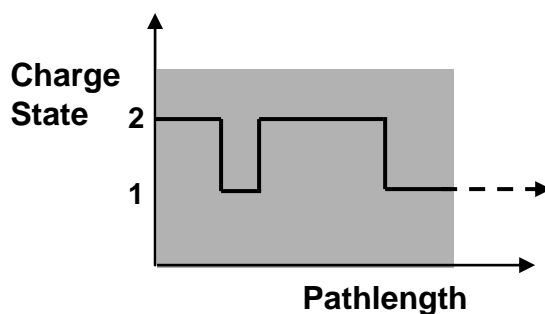


Fig. 6.2

Charge state fluctuation of an individual ion

The resulting energy loss is

$$\Delta E = \alpha S_1 n \Delta s + (1 - \alpha) S_2 n \Delta s \quad (6.2)$$

where S_1 and S_2 denote the stopping cross sections associated to the respective charge states. From this, the variance of the energy loss distribution becomes

$$\Omega_{ce}^2 = \langle (\Delta E - \langle \Delta E \rangle)^2 \rangle = (n \Delta s)^2 (S_1 - S_2)^2 (\langle \alpha^2 \rangle - \langle \alpha \rangle^2) \quad (6.3)$$

α can be expressed by the charge exchange cross sections σ_{12} (from 1 to 2) and σ_{21} (vice versa) yielding

$$\Omega_{ce}^2 = (n \Delta s)^2 (S_1 - S_2)^2 \frac{2\sigma_{12}\sigma_{21}}{(\sigma_{12} + \sigma_{21})^3} \quad (6.4)$$

The resulting width of the energy distribution is proportional to the pathlength and the difference of the stopping powers.

6.3 Energy Transfer Fluctuation

The conventional treatment of energy straggling covers the statistical nature of the atomic collisions. With κ_i denoting the number of collisions with energy transfer T_i , the energy loss becomes for a specific trajectory

$$\Delta E = \sum_i \kappa_i T_i \quad (6.5)$$

The variance of the energy loss, assuming Poisson statistics of the collision numbers, i.e. $\langle (\kappa_i - \langle \kappa_i \rangle)^2 \rangle = \langle \kappa_i \rangle$, results in

$$\Omega^2 = \langle (\Delta E - \langle \Delta E \rangle)^2 \rangle = \sum_i \langle \kappa_i \rangle T_i^2 \quad (6.6)$$

In continuous notation with $\kappa_i \Rightarrow n \Delta s \cdot d\sigma$, this becomes

$$\Omega^2 = n \Delta s \int T^2 d\sigma \quad (6.7)$$

so that the width of the energy distribution scales with the square root of the thickness.

Eq. (6) can easily be evaluated for Rutherford scattering, as first shown by Bohr. (In contrast to stopping – see sect. 5.3 – the integral converges for a zero minimum energy transfer.) For sufficiently many independent collisions, i.e. when neglecting energy loss, a Gaussian energy distribution results with a variance

$$\Omega^2 = n \Delta s \frac{4\pi e^4}{(4\pi\epsilon_0)^2} Q_1^2 Q_2^2 \frac{m_1^2}{(m_1 + m_2)^2} \quad (6.8)$$

Energy straggling is thus independent of the ion energy in the limit of high energy. Evaluating (6.8) for scattering at free electrons ($Q_2^2=1$, $m_2=m_e$, $m_e \ll m_1$, $n_e=nZ_2$) yields the Bohr formula

$$\frac{\Omega_e^2}{n \Delta s} = \frac{4\pi e^4 Z_1^2 Z_2}{(4\pi\epsilon_0)^2} \quad (6.9)$$

For lower ion energy, Lindhard and Scharff calculated the electronic straggling in a local free electron gas approximation with the result

$$\frac{\Omega^2}{\Omega_B^2} = \begin{cases} \frac{L(\xi)}{2} & \text{if } \xi \leq 3 \\ 1 & \text{if } \xi \geq 3 \end{cases} \quad (6.10)$$

with an analytical function and its variable

$$L(\xi) = 1.36\xi^{1/2} - 0.016\xi^{3/2} \quad \xi = \frac{I}{Z_2} \left(\frac{v}{v_0} \right)^2 \quad (6.11)$$

Nuclear straggling can again easily be written in reduced LNS units

$$\omega_n^2 = \frac{\gamma \Delta \rho}{\varepsilon^2} \int_0^{\xi} t f(t^{1/2}) d(t^{1/2}) \quad (6.12)$$

which reproduces (6.8) for the scattering of totally stripped nuclei in the limit of high energy.

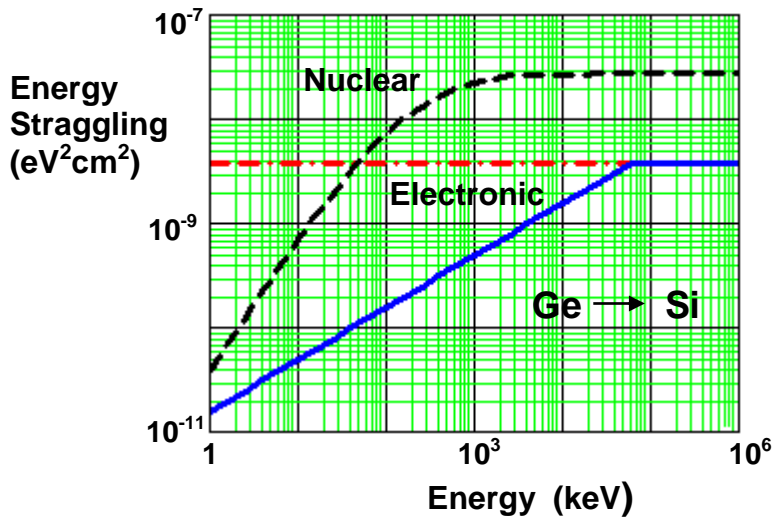


Fig. 6.3a

Energy straggling $\Omega^2/n\Delta s$ for germanium ions in silicon, according to eqs. (6.9) (dashed-dotted line), (6.10) (solid line) and (6.12) (dashed line)

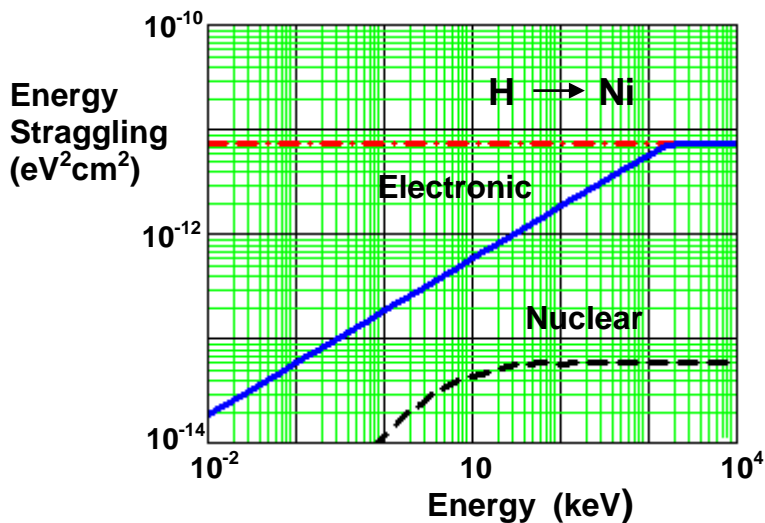


Fig. 6.3b

As Fig. 6.3a, but for hydrogen in nickel

Figs. 6.3a+b show the energy straggling as function of the ion energy for two different ion-target combinations. For very light ions, the nuclear straggling can roughly be neglected, whereas it is dominant for heavy ions (note that the total straggling results from the linear addition of the nuclear and electronic variances which are shown in the figures.)

It should, however, be noted that only simplified results have been presented, assuming sufficiently thick layers and neglecting energy loss, which is a contradiction in general. Very thin films, in particular at high ion energy, may yield strongly asymmetric energy distributions, whereas for thick films the energy loss has to be taken into account.

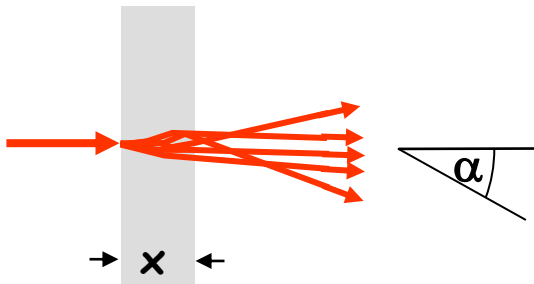


Fig. 7.1

Multiple scattering
of an ion beam

7. Multiple Scattering

As discussed in chapter 5, the stopping of ions results from electronic collisions and the interaction of the screened nuclei, with the electronic interaction often dominating the total stopping. The geometrical trajectory of each ion, however, results essentially from nuclear collisions only, as the electronic scattering is not associated with significant deflections. The statistical nature of the nuclear collisions leads to a broadening of the angular distribution of an ion beam, as indicated in Fig. 7.1, when traversing through a slab of matter with thickness x . The angular distribution of the ions depends on the depth and can be described by a distribution function $f_{\Omega}(x, \alpha)$, with the normalisation condition

$$I = \int f_{\Omega}(x, \alpha) d\Omega = 2\pi \int_0^{\pi} f_{\Omega}(x, \alpha) \sin \alpha d\alpha \approx 2\pi \int_0^{\pi} f_{\Omega}(x, \alpha) \alpha d\alpha \quad (7.1)$$

where the latter equality holds for small angles. More precisely, $f_{\Omega}(x, \alpha)$ represent the distribution over the solid angle. Alternatively, the polar angle distribution $f_{\alpha}(x, \alpha)$ can be employed with the normalisation

$$I = \int_0^{\pi} f_{\alpha}(x, \alpha) d\alpha \quad (7.2)$$

In comparison with (7.1), both distribution functions can be transformed by

$$f_{\alpha}(x, \alpha) = 2\pi \alpha f_{\Omega}(x, \alpha) \quad (7.3)$$

for small angles. This is shown schematically in Fig. 7.2.

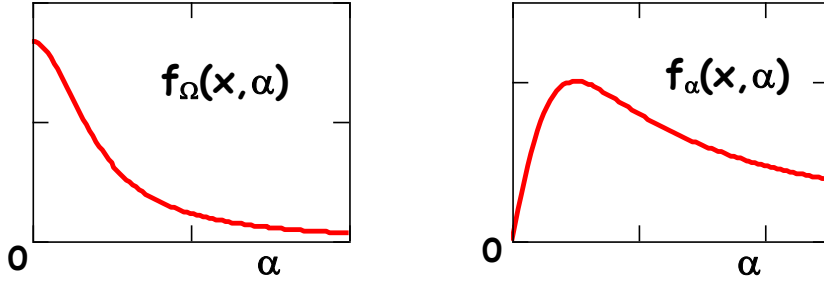


Fig. 7.2

Angular distribution in solid angle (left) and polar angle (right) representation. The polar angle distribution vanishes at $\alpha=0$.

In order to study the evolution of the distribution function at increasing penetration depth, a thin incremental slab δx is considered as shown in Fig. 7.3, which describes an example of so-called "forward" transport. Within this slab, each ion can either change its direction due to a nuclear collision, or it may just penetrate without any nuclear collision (any energy losses are neglected). In the former case, for an ensemble of ions described by the angular distribution function, the new distribution function, $f_{\Omega}(x+\delta x, \alpha)$, results from scattering events which transform fractions of the original function, $f_{\Omega}(x, \alpha')$, into the direction α . The probability is given by the scattering cross sections for all directional changes $\alpha' \rightarrow \alpha$. In the latter case, the distribution function is reproduced with a probability of one minus the total cross section. Therefore:

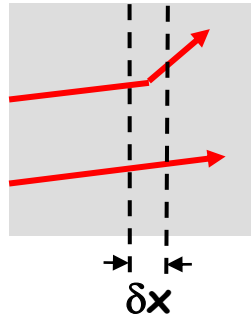


Fig. 7.3

"Forward" transport by nuclear collisions

$$f_{\Omega}(x + \delta x, \alpha) = n\delta x \int d\sigma_n(\alpha' \rightarrow \alpha) f_{\Omega}(x, \alpha') + (1 - n\delta x \int d\sigma_n) f_{\Omega}(x, \alpha) \quad (7.4)$$

Although the resulting angle distribution is axially symmetric, the flight direction of individual ions has both a polar and an azimuthal component. Therefore, in the detailed treatment, two-dimensional angles and angular distribution have to be considered, which is not explicitly indicated here for simplicity. The Taylor expansion of the left-hand side results in the Boltzmann type transport equation

$$\frac{\partial f_{\Omega}(x, \alpha)}{\partial x} = n \int d\sigma_n(\alpha' \rightarrow \alpha) (f_{\Omega}(x, \alpha') - f_{\Omega}(x, \alpha)) \quad (7.5)$$

By suitable mathematical techniques, the integro-differential equation can be solved for an initially sharp angular distribution, $f(0, \alpha) = \delta(\alpha)$, resulting in the Bothe equation

$$f_{\Omega}(x, \alpha) = \frac{1}{2\pi} \int_0^{\infty} k dk J_0(k\alpha) \exp(-n\sigma_0(k)) \quad (7.6)$$

with
$$\sigma_0(k) = \int_0^{\infty} \frac{d\sigma_n}{d\Theta} d\Theta (1 - J_0(k\Theta))$$

where J_0 denotes the zero-order Bessel function. Following Sigmund, the Bothe equation will now be turned into reduced units. The (small) laboratory scattering angle Θ can be transformed into the reduced scattering angle, eq. (3.10), by

$$t^{1/2} = \frac{4\pi\epsilon_0 a E}{2Z_1 Z_2 e^2} \Theta \quad (7.7)$$

Correspondingly, the directional angle is transformed into a reduced angle

$$\tilde{\alpha} = \frac{4\pi\epsilon_0 a E}{2Z_1 Z_2 e^2} \alpha \quad (7.8)$$

Further, a reduced thickness is introduced for the purpose of multiple scattering

$$\tau = \pi a^2 n x \quad (7.9)$$

Then, (7.6) can be rewritten as

$$f_{\tilde{\alpha}}(\tau, \tilde{\alpha}) = \frac{1}{2\pi} \int_0^{\infty} z dz J_0(z\tilde{\alpha}) \exp(-\tau\Delta(z)) \quad (7.10)$$

$$\text{with } \Delta(z) = \int_0^{\infty} d\tilde{\varphi} \frac{f(\tilde{\varphi})}{\tilde{\varphi}^2} (1 - J_0(z\tilde{\varphi}))$$

Multiple scattering distributions are tabulated for a large range of reduced angles and thickness in ref. [10]. An example is given in Fig. 7.4.

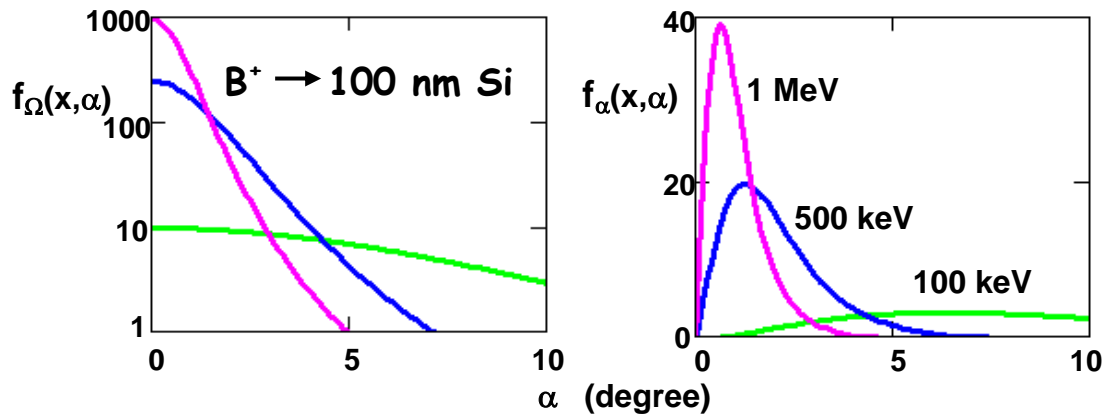


Fig. 7.4 Multiple scattering distributions for boron in silicon. Note the different presentations: (left) solid angle distribution, logarithmic; (right) polar angle distribution, linear.

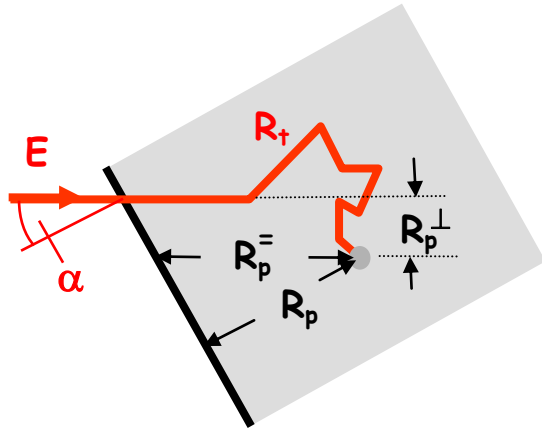


Fig. 8.1

Schematic of an ion track for an ion of incident energy E and angle of incidence α , with range definitions

8. Ion Ranges

As a consequence of stopping and scattering, each individual incident ion forms a random trajectory as shown in Fig. 8.1. Stopping alone defines the total pathlength R_t . From the endpoint of the trajectory projected ranges can be defined (longitudinal, $R_p^=$, and lateral, R_p^\perp). For practical purposes, the (normal) projected range R_p is mostly of interest, since it characterises the implantation depth with respect to the surface. Obviously, R_p is equal to $R_p^=$ for normal incidence. As in most implantation processes the extension of the implanted area is very large compared to the ion range, R_p is mostly also the only range quantity which is accessible to measurement.

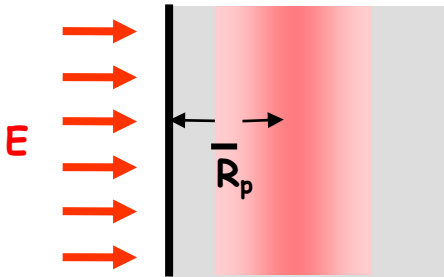


Fig. 8.2

Schematic of range distribution at normal incidence

For many incident ions, the range distribution is smeared out parallel to the surface (see Fig. 8.2), with a mean projected range R_p . If the range distribution peaks sufficiently far from the surface, the mean projected range at an angle of incidence α is related to the mean projected range at normal incidence by

$$\bar{R}_p(\alpha) = R_p^=(\alpha) \cdot \cos(\alpha) = \bar{R}_p(\alpha=0) \cdot \cos \alpha \quad (8.1)$$

at given energy of incidence.

The mean total pathlength is easily calculated from the total stopping cross section by integration along the path s , according to

$$\bar{R}_t(E) = \int_0^{\bar{R}_t} ds = \frac{1}{n_0} \int_0^E \frac{dE'}{S_{tot}(E')} \quad (8.2)$$

Simple analytical solutions can be obtained for certain energy regimes for a given ion-target combination. When electronic stopping is proportional to the ion velocity (eq. (5.33)) and nuclear stopping can be neglected (see Fig. 5.9), the result is

$$\bar{R}_t(E) = \frac{2}{nk_e} \sqrt{E} \quad \text{if } S_n \ll S_e \text{ and } v < v_0 Z_1^{2/3} \quad (8.3)$$

that is, stopping and range are proportional to the ion velocity. When nuclear stopping dominates, only approximate analytical solutions are feasible. Using the power-law approximation (2.16) for the interatomic screening function, the universal result is in reduced units

$$\bar{\rho}_t(\varepsilon) = \frac{s-1}{\lambda_s} \varepsilon^{2/s} \quad \text{if } S_e \ll S_n \quad (8.4)$$

with a constant λ_s to be determined from k_s . For the approximation $s \approx 2$ (see Fig. 3.2) the mean total pathlength becomes proportional to the ion energy according to

$$\bar{\rho}_t(\varepsilon, s=2) = 3.06 \cdot \varepsilon \quad (8.5)$$

which is frequently used as an approximation to "nuclear" ranges.

For certain regimes of parameters, analytical transformations are available to calculate the mean projected range from the mean total pathlength (in view of (8.1), we restrict ourselves to normal incidence). Generally, for $m_1 \gg m_2$ it can be anticipated that angular scattering is small, so that the total pathlength is a good approximation also for the projected range.

For the nuclear stopping regime, Lindhard et al. found from transport theory, again in power-law approximation

$$\bar{R}_p(E) = \bar{R}_t(E) \cdot \left(1 + \frac{m_2}{m_1} \frac{s^2}{4(2s-1)}\right)^{-1} \approx \bar{R}_t(E) \cdot \left(1 + \frac{m_2}{3m_1}\right)^{-1} \quad \text{if } S_e \ll S_n \quad (8.6)$$

where the latter approximation holds again for $s = 2$.

For the opposite case of high ion energy, where electronic stopping dominates, Schiøtt obtained

$$\bar{R}_p(E) = \bar{R}_t(E) \cdot \lambda(1-2\lambda) \quad \text{if } S_n < S_e \text{ and } \lambda < 0.5 \quad (8.7)$$

$$\text{with } \lambda = \frac{m_1}{m_2} \frac{S_e(E)}{S_n(E)}$$

which is applicable only in a narrow regime of parameters, in particular for light ions.

For more precise data of projected ranges, transport theory calculations have to be performed (see sect. 10). Alternatively, computer simulations of the binary collision approximation (BCA) type can be employed (see sect. 11). Both are available in the SRIM computer package [19]. Fig. 8.3 shows the range of nitrogen ions in iron for a broad energy range. The nuclear stopping approximation (8.5) yields a rough approximation to the mean total pathlength at sufficiently low energy. The ratio of the mean projected range to the mean total pathlength is about 50% at the lowest energies and 75% at the highest energies for the present case. For this ratio, eq. (8.6) gives a good result in the nuclear stopping regime, whereas the light-ion approximation (8.7) fails. The predictions from transport theory and computer simulation being available in the SRIM package [19] are in excellent agreement.

Further, as a "rule-of-thumb", it is seen that the mean projected ion range, measured in nm, is approximately equal to the incident energy, measured in keV, which can be used as a first guess for many ion-target combinations.

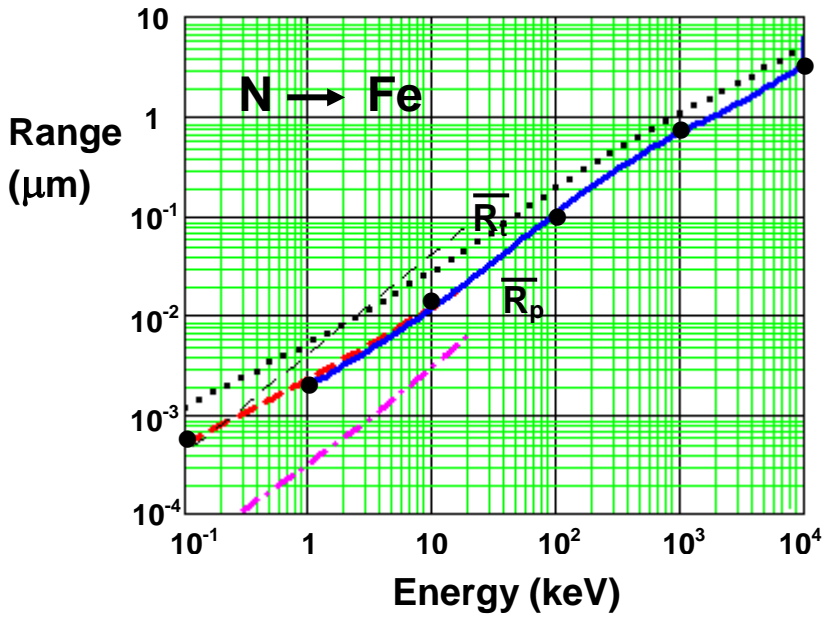


Fig. 8.3

Mean total pathlength of nitrogen ions in iron, from eq. (8.2) with stopping power from SRIM (dotted line) and from eq. (8.5) (thin dashed line), and mean projected range from SRIM transport calculation (solid line), from eq. (8.6) (dashed line), from eq. (8.7) (dashed-dotted line), and from SRIM BCA computer simulation (dots).

9. The Collision Cascade

Nuclear collision do not only contribute to the energy loss of fast ions and determine their angular distributions, but also transfer energy to the atoms of the material, thus creating "primary" recoil atoms. If the transferred energy is sufficiently large, these primary recoils will move along a trajectory similar to that of the incident ion, and may again undergo nuclear collisions, thus creating further generations of recoils and a "collision cascade". Each individual recoil, according to its initial energy, may come to rest at some distance from its original site. This is shown schematically in Fig. 9.1

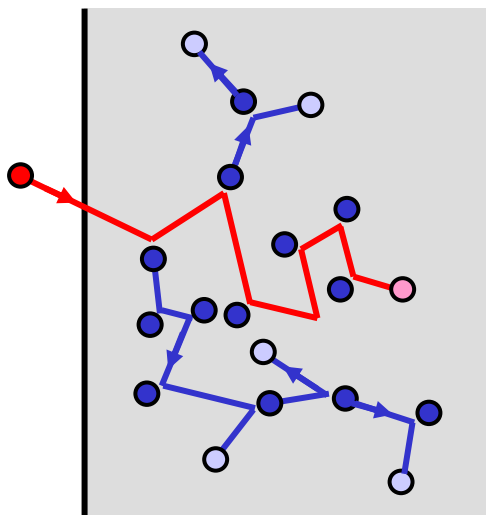


Fig. 9.1

Schematic of an ion trajectory and the associated recoil atoms with their individual trajectories.

In Fig. 9.1, the "final" positions of the ion and the cascade atoms are indicated. Strictly speaking, both come to "rest" after their kinetic energy has fallen down to the thermal energy of the target substance. However, the residual ranges already at eV energies become extremely small and comparable to the

lattice spacing in a solid (see Fig. 8.3). Therefore, if details like the final position in a lattice cell are not of interest, it is reasonable to define a cutoff energy in the order of a few eV to determine the final position of an ion or a recoil atom.

In this "collisional" picture, recoil atoms with an initial energy of less than a few eV (which is also in the order of the binding energy of a lattice atom) are meaningless. Therefore, the generation of cascade atoms is limited. In physical reality, however, the cascade will continue to dissipate its energy and finally thermalise with the surrounding medium.

Depending on the amount of deposited energy per unit volume, the collision cascade may be more or less dense. For low primary energy transfers and an ion range which is large compared to the extension of individual subcascades (see Fig. 9.2), i.e. typically in the case of light ions at high energy, the complete cascade is split into many subcascades, whereas in the opposite case the extension of the subcascades may be in the order of the ion range. Nevertheless, for many incident ions the collision cascades will also fill the complete space around the ion trajectory also in the former case, so that in average the two situations of Fig. 9.2 are not entirely different.

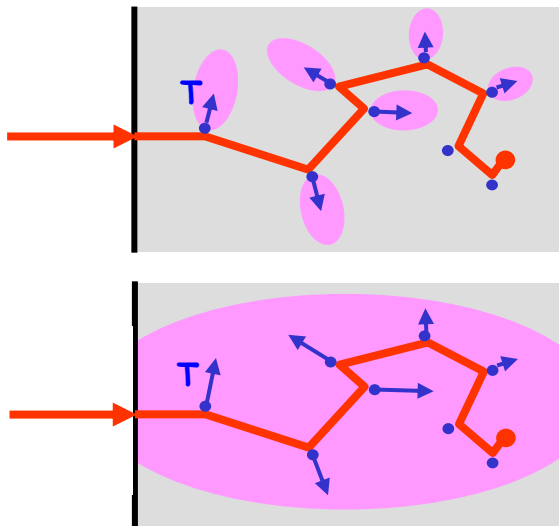


Fig. 9.2

Schematic of the cascade formation for an individual ion trajectory, depending on the average primary initial energy transfer T : Small subcascades for light ions at high energy (top), and one large cascade for heavy ions at sufficiently low energy (bottom).

The density of deposited energy does not only influence the spatial development of the cascade, but also its internal dynamics. Conventionally, three regimes are defined (see Fig. 9.3). In the single-collision regime (Fig. 9.3a), which is typical for light ions at low energy, a cascade does not really develop and the atomic motion is stopped after a few collision events.

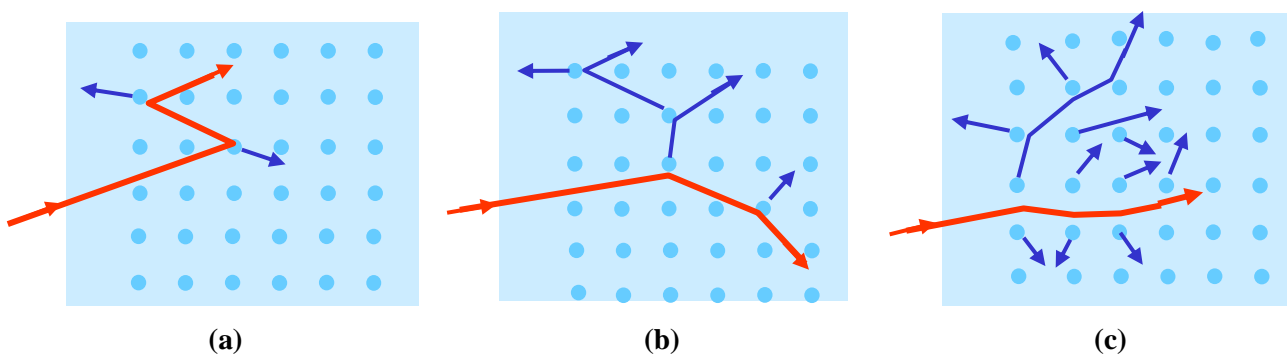


Fig. 9.3

Cascade regimes (schematically): (a) Single collision regime; (b) Linear cascade; (c) Thermal spike

The "Linear Cascade" regime (Fig. 9.3b) is defined by the requirement that collisions take place essentially only between fast particles and atoms being at rest (in the collisional sense as discussed above, i.e. neglecting thermal motion). This regime is the standard regime in the range of ion energies which are covered by the present lecture, and will be the subject of most of the discussions below. As the single collision regime, it allows to treat the cascade as a sequence of two-body collisions, which have been described in chapters 1-4.

In contrast, in the "Thermal Spike" regime (Fig. 9.3c) the cascade becomes so dense that collisions between fast particles play an essential role. In the limit, all lattice atoms within the cascade become a thermal ensemble with a high temperature, which may exceed the melting temperature of the solid and even its evaporation temperature on a short time scale.

Finally, it is worth while to address the characteristic time scales of a collision cascade. The slowing-down time of a fast atom in a target substance is according to the definition of the stopping cross section (see eq. (5.2)) with $ds = vdt$

$$t = \frac{1}{n} \int_{E_{co}}^E \sqrt{\frac{m}{2E'}} \frac{dE'}{S(E')} \quad (9.1)$$

where m and E denote the mass and the initial energy of the atom, respectively, and E_{co} the cutoff energy. With the stopping being proportional to the velocity, which holds for the electronic stopping except for very high energy and for the nuclear stopping at very low energy (see ch. 5), that is for most ions and the low-energy cascade atoms, (9.1) becomes with the stopping constant k

$$t = \frac{1}{nk} \sqrt{\frac{m}{2}} \int_{E_{co}}^E \frac{dE'}{E'} = \frac{1}{nk} \sqrt{\frac{m}{2}} \log\left(\frac{E}{E_{co}}\right) \quad (9.2)$$

For the ion-target combination of Fig. 8.3, a slowing-down time of about $5 \cdot 10^{-13}$ s is obtained, which is in the order of the lattice vibration period. The slowing-down time depends only weakly on the initial energy and on the ion and target species. Thus, the lifetime of a collisional cascade is in the order of 10^{-13} to 10^{-12} s.

The lateral extension of a cascade depends both on the characteristic primary energy transfer and the trajectory of the ion. In the present range of energies, some nm are a good estimate. From this, a typical area of a cascade, projected onto the surface plane, is in the order of 10^{-12} to 10^{-13} cm². For an ion flux of 10^{16} cm⁻²s⁻¹, which is typical for conventional high-current ion implantation, this area is hit by 10^3 to 10^4 ions per second. In comparison with the cascade lifetime as given above, this indicates an extremely small possibility of overlap of collision cascades initiated by subsequently implanted ions in the order of 10^{-9} . Thus, cascade overlap by different ions can be excluded.

10. Transport Equations Governing the Deposition of Particles and Energy

10.1 Primary Distributions

Eq. (7.4) represents a special form of a so-called "forward" transport equation, which delivers a distribution function of a beam property (deflection angle, particle energy), with the depth x as parameter. In turn, distributions of particle or energy deposition are defined as functions of the depth x , with the properties of the incident beam (incident energy E and incident angle, represented by its directional cosine η) as parameters.

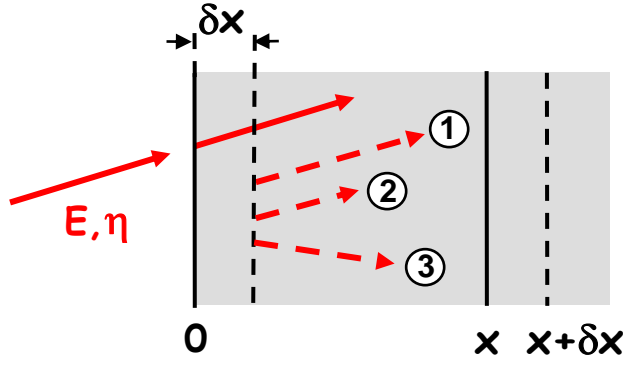


Fig. 10.1

Schematic of the "backward" transport formalism to calculate deposition distribution functions

An incident ion can interact with the substance in a differential element of depth δx at the surface, which, according to the scattering probabilities, results in a modified energy and/or direction at δx . These new initial conditions contribute to the deposition function f at $x+\delta x$, each with their corresponding distribution functions as function of x due to the translational invariance of the medium, which is assumed to be homogeneous. In δx , the ion may undergo a nuclear collision ((3) in Fig. 10.1), changing the direction η to η' and the energy E to E' , an electronic collision ((2)), changing the energy E to $E-\Delta E$ but not the direction, or no collision. Correspondingly, the following ansatz results, which is given in 1-dimensional form for simplicity:

$$\begin{aligned}
 f(x+\delta x, E, \eta) &= n v \delta t \int d\sigma_n (E, \eta \rightarrow E', \eta') f(x, E', \eta') \\
 &+ n Z_2 v \delta t \int d\sigma_e (E, \eta \rightarrow E - \Delta E, \eta) f(x, E - \Delta E, \eta) \\
 &+ \left(1 - n v \delta t \int d\sigma_n - n Z_2 v \delta t \int d\sigma_e \right) f(x, E, \eta)
 \end{aligned} \tag{10.1}$$

Here, v denotes the incident velocity and $v\delta t$ the traversed pathlength through δx , such that

$$\delta x = \eta v \delta t \tag{10.2}$$

Taylor expansion on the left-hand side yields

$$\begin{aligned}
 \eta \frac{\partial f}{\partial x}(x, E, \eta) &= n \int d\sigma_n (E, \eta \rightarrow E', \eta') (f(x, E', \eta') - f(x, E, \eta)) \\
 &+ n \int d\sigma_e (E, \eta \rightarrow E - \Delta E, \eta) (f(x, E - \Delta E, \eta) - f(x, E, \eta))
 \end{aligned} \tag{10.3}$$

Further expanding

$$\begin{aligned}
 n \int d\sigma_e (f(x, E - \Delta E, \eta) - f(x, E, \eta)) &= -n \frac{\partial f}{\partial E}(x, E, \eta) \int d\sigma_e \Delta E \\
 &= -n S_e(E) \frac{\partial f}{\partial E}(x, E, \eta)
 \end{aligned} \tag{10.4}$$

yields the Boltzmann type transport equation

$$\eta \frac{\partial f}{\partial x}(x, E, \eta) = -nS_e(E) \frac{\partial f}{\partial E}(x, E, \eta) + n \int d\sigma_n(E, \eta \rightarrow E', \eta') (f(x, E', \eta') - f(x, E, \eta)) \quad (10.5)$$

For the distribution f_R of ion ranges, the normalisation conditions reads

$$\int_{-\infty}^{+\infty} f_R(x, E, \eta) dx = 1 \quad (10.6)$$

so that $f_R(x, E, \eta) dx$ denotes the probability to find an implanted ion deposited in the depth interval dx at the depth x .

As already indicated by the integration limits in eq. (10.6), the transport equation is normally solved in an infinite medium, so that a fraction of f may extend to $x < 0$. The identification of this fraction with the ion reflection coefficient R , according to

$$\int_{-\infty}^0 f_R(x, E, \eta) dx = R \quad (10.7)$$

holds only approximately, since the transport formalism allows a multiple crossing of an ion trajectory through the "surface" at $x = 0$, whereas in reality the ion is lost at the first transmission through the surface.

Different mathematical procedures to solve eq. (10.5) analytically for ion ranges can be found in the literature, such as in refs. [3,20,21]. In ref. [21], the angular dependence is separated by means of a Legendre expansion

$$f_R(x, E, \eta) = \sum_{l=0}^{\infty} (2l+1) P_l(\eta) f_{Rl}(x, E) \quad (10.8)$$

so that the transport equation can be written down in an recursive form of the Legendre components f_{Rl} . For these, the v -th moments are defined according to

$$f_{Rl}^v(E) = \int_{-\infty}^{\infty} x^v f_{Rl}(x, E) dx \quad (10.9)$$

The transformation of the transport equation then allows a stepwise calculation of the moments with a proper screened-Coulomb scattering cross section and for a properly chosen electronic stopping cross section. With the moments of any distribution function, $f^v(x)$, given, the distribution function itself can be reconstructed, e.g., by using the Edgeworth expansion

$$f(x) = \frac{C}{\sqrt{\langle \Delta x^2 \rangle}} \left[\varphi_0(\xi) - \frac{\Gamma_1}{6} \varphi_3(\xi) + \left(\frac{\Gamma_2}{24} \varphi_4(\xi) + \frac{\Gamma_1}{72} \varphi_6(\xi) \right) + \dots \right] \quad (10.10)$$

where C is a normalisation constant and

$$\langle \Delta x^n \rangle = \langle (x - \langle x \rangle)^n \rangle \quad (10.11)$$

with the moments

$$\langle x^n \rangle = \int f(x) \cdot x^n dx \quad (10.12)$$

$\varphi_k(\xi)$ denote the Gaussian function and its derivatives,

$$\varphi_k(\xi) = \frac{1}{\sqrt{2\pi}} \frac{d^k}{d\xi^k} \exp\left(-\frac{\xi^2}{2}\right); \quad \xi = \frac{x - \langle x \rangle}{\sqrt{\langle \Delta x^2 \rangle}} \quad (10.13)$$

Finally, the shape parameter "skewness" and "excess" are given by

$$\Gamma_1 = \frac{\langle \Delta x^3 \rangle}{\langle \Delta x^2 \rangle^{3/2}} \quad \Gamma_2 = \frac{\langle \Delta x^4 \rangle}{\langle \Delta x^2 \rangle^2} - 3 \quad (10.14)$$

respectively. For a pure symmetric Gaussian function, both Γ_1 and Γ_2 vanish.

An example of range distribution in LSS reduced quantities for the depth and the energy is given in Fig. 10.2. At low energy where the electronic stopping scales with velocity, the depth scale scales with the product of the electronic stopping constant and the reduced depth.

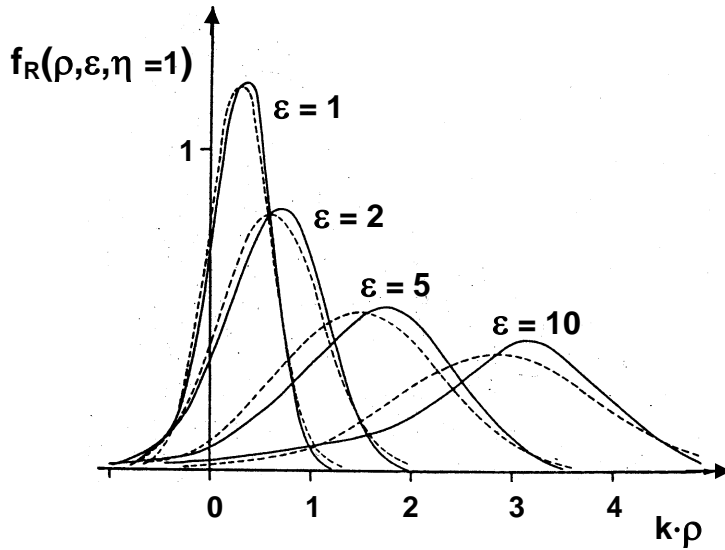


Fig. 10.2

Range distributions at low energy for normal incidence ($\eta = 1$) in reduced LSS units, as obtained from a transport theory calculation with two moments (dotted line) yielding a Gaussian function, and three moments (solid line). k denotes the electronic stopping constant in reduced units, $(d\varepsilon/d\rho)_e = k \cdot \varepsilon^{1/2}$, cf. eq. (5.33).

Depth distributions of the deposited energy can be obtained in the same way as range distributions, as long as only primary collisions between the incident ion and the target atoms are considered. These "primary" distributions of the deposited energy are a reasonable approximation when the extension of any collision cascade between the target atoms, which is triggered by a primary collision, is small compared to the ion range, as for light ions in heavy substances where the primary energy transfer is small, or for high energy where the ion range is large.

Transport equations like (10.5) can be formulated both for the energy which is dissipated into nuclear collisions, and the energy which is dissipated into electronic collisions. The corresponding deposition functions are often denoted as "damage" deposition function, f_D , and "ionisation" deposition function, f_I , respectively. For each of these, normalisation conditions hold according to

$$\int_{-\infty}^{+\infty} f_D(x, E, \eta) dx = v(E) \quad (10.15)$$

and

$$\int_{-\infty}^{+\infty} f_I(x, E, \eta) dx = \nu(E) \quad (10.16)$$

with $\nu(E)$ and $\iota(E)$ denoting the total fractions of the incident energy which are dissipated into nuclear and electronic collisions, respectively, with

$$\nu(E) + \iota(E) = E \quad (10.17)$$

The nuclear fraction can be determined from the integrated transport equation. As the distribution function vanishes at infinity, (10.5) yields

$$S_e(E) \frac{d\nu(E)}{dE} + \int d\sigma_n (\nu(E) - \nu(E')) = 0 \quad (10.18)$$

Setting $E' = E - T$ with the nuclear energy transfer T and expanding for $T \ll E$ results in

$$\nu(E) = \int_0^E \frac{S_n(E)}{S_e(E)} dE \quad (10.19)$$

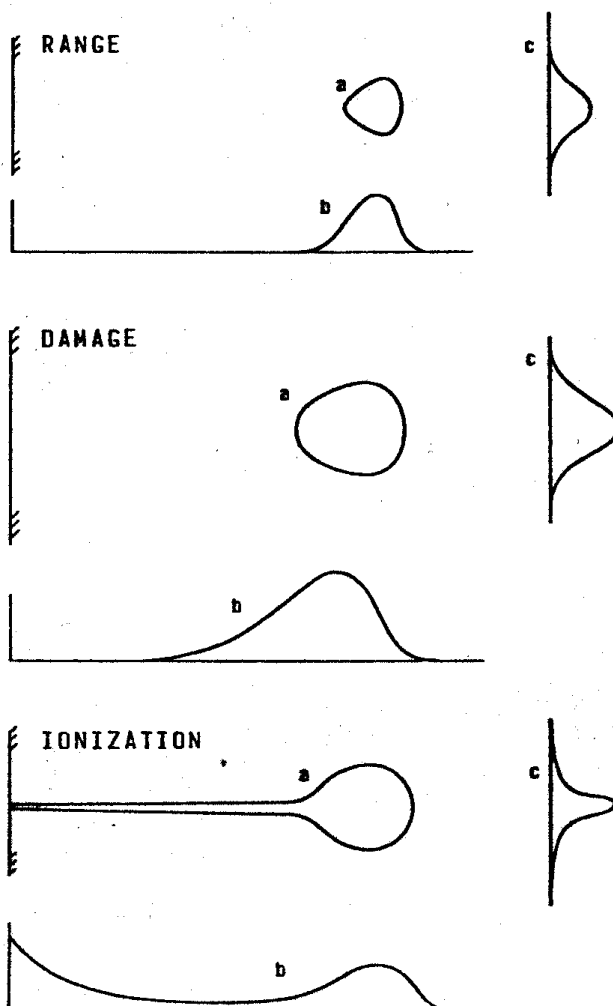


Fig. 10.3

Schematic representation of high-energy range, damage, and ionisation distributions. (a) density contour, (b) and (c) projections of the distribution functions onto a plane parallel and normal to the direction of incidence, respectively.

Corresponding evaluations and tabulations can be found in the literature. Fig. 10.3 shows a schematic representation of high-energy range, damage and ionisation distributions in three dimensions. At small depth, the nuclear energy deposition is small due to the low scattering cross section at high energy. Towards the end of the ion trajectories, the ion energy and thereby the nuclear energy dissipation becomes low, so that the damage distribution normally peaks at slightly lower depth than the range distribution. However, it has to be taken into account that multiple large angle deflections, which occur with increasing probability towards the end of the range, may result in multiple energy deposition events at the same depth for only one incident ion. This also explains the peak of the ionisation distribution function at large depth. Otherwise, it reflects the dependence of electron stopping on energy.

10.2 Distributions of Energy Deposition Including Collision Cascades

In the general case, secondary collision cascades of the target atoms have to be taken into account for the calculation of the energy deposition. This is mandatory for ion-target combinations with about equal masses, and for sufficiently low energies.

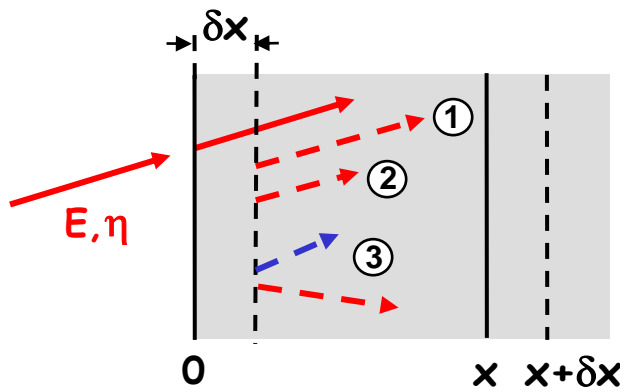


Fig. 10.4

Schematic of the transport mechanism when including secondary recoil atoms

The validity of the linear cascade regime is assumed. The secondary recoil atoms have to be taken into account which are generated in nuclear collisions (see Fig. 10.4, case (3)). For the treatment of nuclear energy deposition, the three-dimensional "damage" distribution function is defined in such a way that the differential amount of energy

$$dE_n = F_D(E, \bar{\eta}, \bar{r}) d^3 \bar{r} \quad (10.20)$$

is dissipated into the volume element $d^3 \bar{r}$ around \bar{r} , at given incident energy E and direction η . Adding to the nuclear collision term of eq. (10.1) a term for the recoil atom, with an initial energy equal to the nuclear energy transfer T and an initial direction η'' , results in

$$\begin{aligned} F_D(E, \bar{\eta}, \bar{r} + \delta \bar{r}) = & n |\delta \bar{r}| \int d\sigma_n (E \rightarrow E - T) (F_D(E - T, \bar{\eta}', \bar{r}) + F_D(T, \bar{\eta}'', \bar{r})) \\ & + n Z_2 |\delta \bar{r}| \int d\sigma_{el} (E \rightarrow E - \Delta E) F_D(E - \Delta E, \bar{\eta}, \bar{r}) \\ & + (1 - n |\delta \bar{r}| \int d\sigma_n - n Z_2 |\delta \bar{r}| \int d\sigma_{el}) F_D(E, \bar{\eta}, \bar{r}) \end{aligned} \quad (10.21)$$

Similarly as above and with

$$\bar{\eta} = \frac{\delta \bar{r}}{|\delta \bar{r}|} \quad (10.22)$$

the transport equation results as

$$-\bar{\eta}\bar{\nabla}F_D(E, \bar{\eta}, \bar{r}) = nS_e(E)\frac{\partial F_D}{\partial E}(E, \bar{\eta}, \bar{r}) \quad (10.23)$$

$$+ n \int d\sigma_n(E, T) (F_D(E, \bar{\eta}, \bar{r}) - F_D(E-T, \bar{\eta}', \bar{r}) - F_D(T, \bar{\eta}'', \bar{r}))$$

Evaluations for the damage function, and for the ionisation function F_I (see 10.1) are again found in the literature. Examples in comparison to experimental results are given in Fig. 10.5.

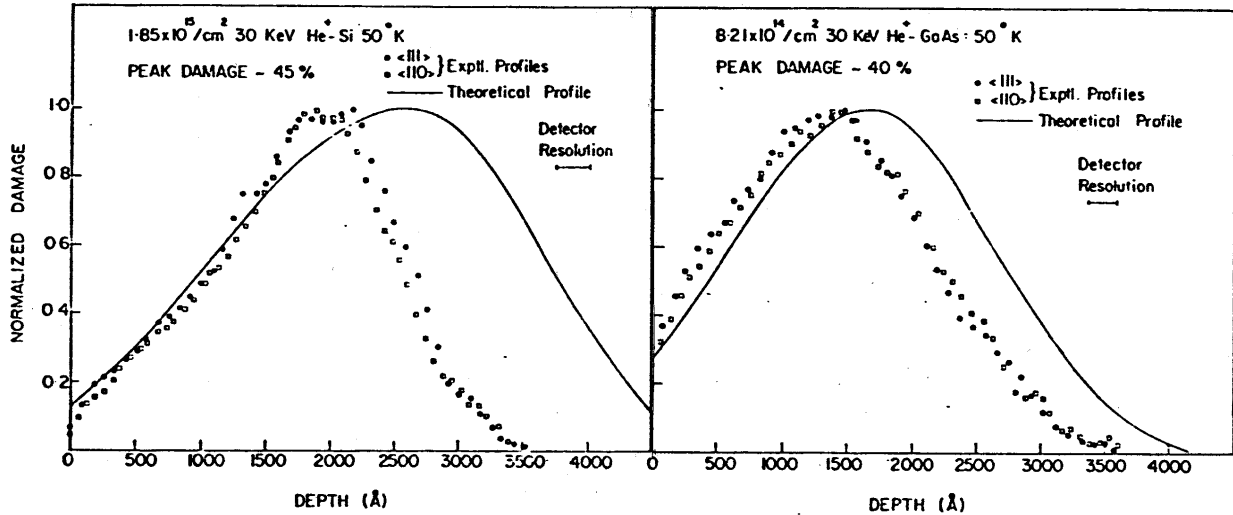


Fig. 10.5: Normalised damage profiles for He^+ bombardment of Si and GaAs. The experimental data have been obtained by high-energy ion channeling analysis.

It is not straightforward to measure a damage or ionisation function. Only the post-irradiation effects are accessible to experiments, as, e.g., the amount of remaining lattice damage. In the case of nuclear energy deposition, the creation of lattice damage is subject to a threshold energy of a recoil atom (see ch. 12), so that low energy transfer events will contribute to the deposition function, but not to physical lattice damage. This might partly explain the difference of the experimental and theoretical data in Fig. 9.5. Moreover, the survival of lattice defects depends strongly on the type of material and the temperature. Most semiconductors exhibit stable defects still at room temperature, whereas metals have to be kept typically below 5...30 K.

10.3 Cascade Energy Distribution

In 10.1 and 10.2, transport formalisms have been described which cover the deposition of the incident ions and the energy which is carried into the target substance. In the following, the energy distribution of the cascade atoms will be discussed. Assuming that the cascade is initiated by a primary recoil atom with initial energy E , a distribution function F_E of initial energies of all cascade atoms, which are subsequently generated by nuclear collisions, can be defined in such a way that

$$dN_0 = F_E(E, E_0)dE_0 \quad (10.24)$$

denotes the average number of cascade atoms which are generated in the interval of starting energies $E_0 \dots E_0 + dE_0$. F is called "recoil density", with the condition

$$F_E(E, E_0) = 0 \quad \text{if } E_0 > E \quad (10.25)$$

Similarly as above, the ansatz for the corresponding transport equation is

$$\begin{aligned}
F_E(E, E_0) dE_0 &= n \delta x d\sigma_n(E \rightarrow E_0) \\
&+ n Z_2 \delta x \int d\sigma_{el}(E \rightarrow E - \Delta E) F_E(E - \Delta E, E_0) dE_0 \\
&+ n \delta x \int d\sigma_n(E \rightarrow E - T) (F_E(E - T, E_0) + F_E(T, E_0)) dE_0 \\
&+ (1 - n \delta x \int d\sigma_n - n Z_2 \delta x \int d\sigma_{el}) F_E(E, E_0) dE_0
\end{aligned} \tag{10.26}$$

Formally compared to eq. (10.21), an additional nuclear collision term has to be taken which describes the direct conversion of the primary atom to an atom with energy E_0 . This is not contained in the second term as a starting energy of E_0 will not contribute by further collision according to (10.25). The Taylor expansions, as formerly, yield

$$\begin{aligned}
S_{el}(E) \frac{\partial}{\partial E} F_E(E, E_0) &= \frac{d\sigma_n}{dE_0}(E \rightarrow E_0) \\
&+ \int d\sigma_n(E \rightarrow E - T) (F_E(E - T, E_0) + F_E(T, E_0) - F_E(E, E_0))
\end{aligned} \tag{10.27}$$

If electronic stopping is neglected in view of the rather low energy of most of the cascade atoms, and the nuclear scattering cross section is evaluated for the power-law screening function (2.16), (10.27) can be solved analytically by using Laplace transforms and the convolution theorem, yielding

$$F_E(E, E_0) = \frac{m}{\Psi(1) - \Psi(1-m)} \frac{E}{E_0^2} \quad \text{if } E_0 \ll E \tag{10.28}$$

where $m = s^{-1}$ denotes the inverse of the power index of the screening function (see (2.16)) and

$$\Psi(y) = \frac{d}{dy} \log \Gamma(y) \tag{10.29}$$

with $\Gamma(y)$ denoting the Gamma function, and

$$F_E(E, E_0) = \frac{m}{\Gamma(1) - \Gamma(1-m)} \frac{1}{E_0} \left(\frac{E}{E_0} - 1 \right)^m \quad \text{if } E_0 \lesssim E \tag{10.30}$$

According to (10.28), the number of cascade atoms scales with the inverse square of their starting energy (so-called "Coulomb" spectrum), so that (10.28) describes the vast amount of all cascade atoms. The cascade density diverges with $E_0 \rightarrow 0$, which is a contradiction with the assumption of a linear cascade. However, the lattice atoms are bound to their original sites which has been neglected so far. With a binding energy U , an approximate solution is, replacing (10.28)

$$F_E(E, E_0) = \frac{m}{\Psi(1) - \Psi(1-m)} \frac{E}{(E_0 + U)^{1-m} E_0^{1+m}} \quad \text{if } E_0 \lesssim U \ll E \tag{10.31}$$

Taking electronic stopping rigorously into account would be rather complicated. Therefore, the total available energy E is simply replaced by the fraction which is dissipated in nuclear rather than electronic collisions, resulting in (if the binding is neglected again)

$$F_E(E, E_0) = \frac{m}{\Psi(1) - \Psi(1-m)} \frac{v(E)}{E_0^2} \tag{10.32}$$

Note that $v(E)$ in this context is different from the nuclear energy dissipation as defined for the primary damage distribution (see (10.15)-(10.19)), as secondary recoils are included. Here, the corresponding transport equation is

$$S_e(E) \frac{dv(E)}{dE} + \int d\sigma_n(E \rightarrow E-T)(v(E) - v(E-T) - v(T)) = 0 \quad (10.33)$$

(10.33) can only be solved numerically. Fig. 10.6 shows the result as function of the primary energy for different materials. Often,

$$v(E) \approx 0.9 \cdot E \quad (10.34)$$

is taken as a good approximation.

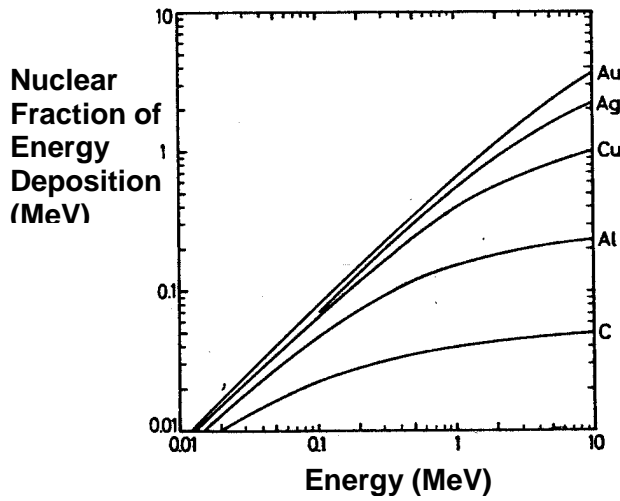


Fig. 10.6

Energy $v(E)$ of the primary recoil which is dissipated in nuclear collisions. The corresponding electronic fraction is $\iota(E) = 1 - v(E)$.

Typical starting energies of most of the cascade atoms are in the order of 10...100 eV corresponding to minimum distances of approach of about 1 nm. Here, the "hard core" approximation $s \rightarrow \infty$ or $m \rightarrow 0$ is reasonable. Then, (10.32) becomes

$$F_E(E, E_0) = \frac{1}{\Psi'(1)} \frac{v(E)}{E^2} = \frac{6}{\pi^2} \frac{v(E)}{E^2} \quad (10.35)$$

10.4 Spatial Cascade Energy Distribution

In order to fully describe the energetic and spatial development of the collision cascade, the results of 10.2 and 10.3 have to be combined now. The angular distribution of the direction of motion of the cascade particles is assumed to be isotropic, since a full momentum relaxation can be expected for most of the cascade atoms with sufficiently low energy. Therefore, the angular distribution is neglected here.

Defining a spatial recoil density F such that

$$dN(E_0, \vec{r}) = F(E, \vec{\eta}, E_0, \vec{r}) dE_0 d^3\vec{r} \quad (10.36)$$

is the number of atoms starting in the volume element d^3r around r and at an energy between E_0 and $E_0 + dE_0$, in a cascade which is initiated by a primary recoil of energy E and with direction η , the transport ansatz becomes

$$\begin{aligned}
F(E, \bar{\eta}, E_0, \bar{r} + \delta\bar{r}) &= n|\delta\bar{r}|d\sigma_n(E \rightarrow E_0)\delta(\bar{r}) \\
&+ n|\delta\bar{r}|\int d\sigma_n(E \rightarrow E - T)(F(E - T, \bar{\eta}', E_0, \bar{r}) + F(T, \bar{\eta}'', E_0, \bar{r})) \\
&+ nZ_2|\delta\bar{r}|\int d\sigma_{el}(E \rightarrow E - \Delta E)F(E - \Delta E, \bar{\eta}, E_0, \bar{r}) \\
&+ (1 - n|\delta\bar{r}|\int d\sigma_n - nZ_2|\delta\bar{r}|\int d\sigma_{el})F_D(E, \bar{\eta}, E_0, \bar{r})
\end{aligned} \tag{10.37}$$

with the resulting transport equation

$$\begin{aligned}
-\bar{\eta}\bar{\nabla}F(E, \bar{\eta}, E_0, \bar{r}) + n\frac{d\sigma(E \rightarrow E_0)}{dE_0}\delta(\bar{r}) - nS_e(E)\frac{\partial F}{\partial E}(E, \bar{\eta}, E_0, \bar{r}) \\
= n\int d\sigma_n(F(E, \bar{\eta}, E_0, \bar{r}) - F(E - T, \bar{\eta}', E_0, \bar{r}) - F_D(T, \bar{\eta}'', E_0, \bar{r}))
\end{aligned} \tag{10.38}$$

with the conditions

$$F(E, \bar{\eta}, E_0, \bar{r}) = 0 \quad \text{if } E_0 > E \tag{10.39}$$

and

$$\int F(E, \bar{\eta}, E_0, \bar{r})d^3\bar{r} = F_E(E, E_0) \tag{10.40}$$

The solution of eq. (10.38) proceeds via moment equations (for comparison, see eq. (10.9)). For the higher moments, the cutoff condition, eq. (10.39), is neglected, as the few additional high-energy atoms, which are artificially included, will little influence the main fraction of the cascade atoms. Then, the solution is straightforward. With the correct normalisation, the result is

$$F(E, \bar{\eta}, E_0, \bar{r}) = \frac{6}{\pi^2} \frac{F_D(E, \bar{\eta}, \bar{r})}{E_0^2} \tag{10.41}$$

which is plausible as it simply combines the damage function (see eq. (10.20)) with the recoil density (eq. (10.35)).

11. Binary Collision Approximation Computer Simulation of Ion and Energy Deposition

As demonstrated in the preceding chapter, transport theory calculations of ion slowing down and the associated recoils atoms, in the linear cascade regime, can provide valuable analytical expressions which describe the important physical mechanisms and dependencies. However, the solutions are often complicated and require simplifying assumptions. A major obstacle, e.g., is the treatment of the surface, as the transport equations can, without considerable additional effort, be solved only in an infinite medium, thus describing the physical situation of an internally starting beam. The treatment of an infinite medium in the transport calculations allows for multiple crossing of a given recoil trajectory through an arbitrary plane in the substance, whereas in reality the particle is lost when first crossing the surface. Therefore, also the formation of collision cascades near the surface is overestimated in infinite medium calculations. This problem arises in particular for low energies and/or heavy ions with a significant fraction of the total energy being deposited very close to the

surface. Consequently, also the treatment of the single collision regime becomes doubtful when it is applied to near-surface phenomena.

An alternative solution, which also covers the linear cascade regime, is the application of computer simulations in the so-called binary-collision approximation (BCA). In the following, only the main issues of BCA will be described. As in the preceding chapters, a random distribution of atoms in the substance will be assumed, and any effects of crystallinity will be neglected, although "crystalline" BCA codes are available. The features described below are consistent with the TRIM (TRansport of Ions in Matter) family of BCA codes. Also the BCA simulation code of the SRIM package[13,16,19] belongs to this group.

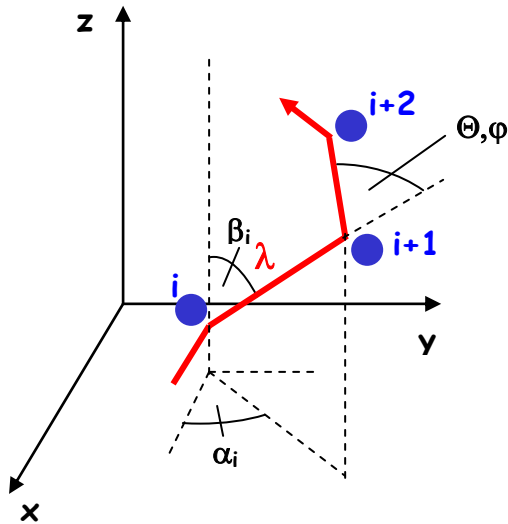


Fig. 11.1

Section of an ion or recoil trajectory with subsequent nuclear collisions with atoms denoted by i , $i+1$ and $i+2$.

The physical model of the BCA simulation is depicted by the ion slowing-down and cascade formation schematic of Fig. 9.1. The trajectory of an incident ion or an recoil atom is approximated by a polygon track given by subsequent nuclear collisions. A section is shown in Fig. 11.1. Directly after a nuclear collision with atom i (or when entering the substance), the moving atoms is characterised by a state given by its energy E_i , and its directional polar and azimuthal angles α_i and β_i , respectively. The atom is allowed to move along a free path λ . In TRIM, λ is defined by the mean atomic distance of the substance

$$\lambda = n^{-1/3} \quad (11.1)$$

rather than choosing it randomly. Thus, the TRIM model is more valid for an amorphous solid than for a random medium, which would be modelled by an analytical transport calculation. However, the impact parameter of the subsequent nuclear collision ($i+1$) is chosen randomly (see Fig. 11.2). According to the cylindrical symmetry, the actual impact parameter p is calculated from a random number r , which is equally distributed in $[0...1]$

$$p = p_{max} \sqrt{r} \quad (11.2)$$

with a maximum impact parameter p_{max} which satisfies

$$\pi p_{max}^2 \lambda = n^{-1} \quad (11.3)$$

so that one collision takes place per atomic volume of the substance. With a proper interatomic potential (recent versions of TRIM use the universal potential given by eqs. (2.17) and (3.5)), the polar scattering angle ϑ is calculated from the classical trajectory integral, eq. (1.12). The numerical integration for each nuclear collision would be rather time-consuming. Therefore, TRIM makes use of an approximate analytical formula, the so-called "magic" scattering formula.

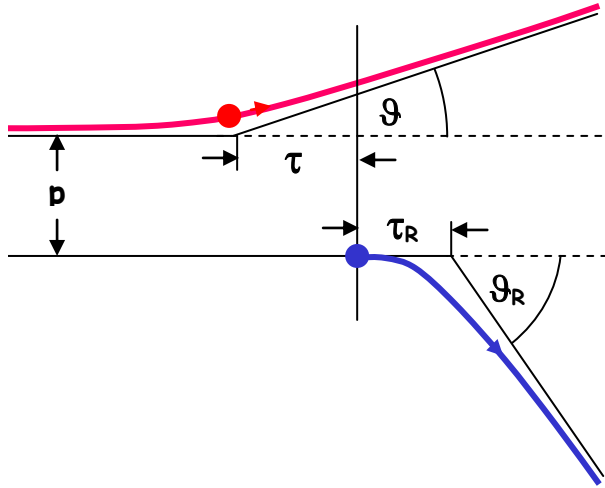


Fig. 11.2

Scattering geometry of binary collisions in the center-of-mass system, with the asymptotic trajectories

For a complete definition of the scattering process, the azimuthal deflection angle ϕ is calculated according to the axial symmetry from an additional random number r by

$$\phi = 2\pi r \quad (11.4)$$

Due to the random choice of the impact parameter (or the polar deflection angle) and the azimuthal deflection angle, BCA codes are often referred to as "Monte Carlo" simulations.

ϑ is transformed into the laboratory system deflection angle Θ (see Fig. 11.1) according to eq. (1.4). Simultaneously, a recoil atom is generated if desired with an initial polar direction Φ relative to the original direction of the projectile, according to eq. (1.4), and an azimuthal recoil angle $\phi + \pi$ according to (11.4).

The idealised trajectories of Fig. 9.1 are represented by the asymptotic trajectories before and after each collision. As shown in Fig. 9.2, the asymptotic trajectories after scattering originate from an axial position which is displaced from the original position of the recoil atom. In TRIM, the so-called "time integrals" are approximated by the hard-sphere approximation

$$\tau = p \tan \frac{\vartheta}{2} \quad (11.5)$$

for the projectile and

$$\tau_R = 0 \quad (11.6)$$

for the recoil atom.

Electronic energy loss is taken into account either in a "nonlocal" mode along the trajectory, resulting in

$$\Delta E_{nl} = n S_e (\lambda - \tau) \quad (11.7)$$

with S_e according to ch. 5, or in a "local" mode in correlation with the nuclear collisions, using the convenient "Oen-Robinson" formula

$$\Delta E_l = \frac{0.045}{\pi a^2} \exp\left(-0.3 \frac{R_{min}}{a}\right) \cdot S_e \quad (11.8)$$

with R_{min} denoting the minimum distance of approach (see eq. (1.13)) and a the screening length. (11.8) has been derived in a similar way as the Firsov formula, eq. (5.34). Often, an equipartition

$$\Delta E = \frac{1}{2} (\Delta E_{nl} + \Delta E_l) \quad (11.9)$$

is chosen rather arbitrarily.

Including the nuclear energy transfer T (eq. (1.6)), the transformation of the state of the projectile is now given by

$$E_{i+1} = E_i - T - \Delta E \quad (11.10)$$

and

$$\begin{pmatrix} \alpha_{i+1} \\ \beta_{i+1} \end{pmatrix} = TR(\Theta, \varphi) \bullet \begin{pmatrix} \alpha_i \\ \beta_i \end{pmatrix} \quad (11.11)$$

where TR denotes the geometrical transformation to the new directional angles. When recoils are included, the initial state of the generated recoil is given by

$$E_r = T - U_b \quad (11.12)$$

and

$$\begin{pmatrix} \alpha_r \\ \beta_r \end{pmatrix} = TR(\Phi, \varphi + \pi) \bullet \begin{pmatrix} \alpha_i \\ \beta_i \end{pmatrix} \quad (11.13)$$

In (11.12), U_b denotes the bulk binding energy of the lattice atoms (a few eV, often it is set to zero due to the lack of better knowledge).

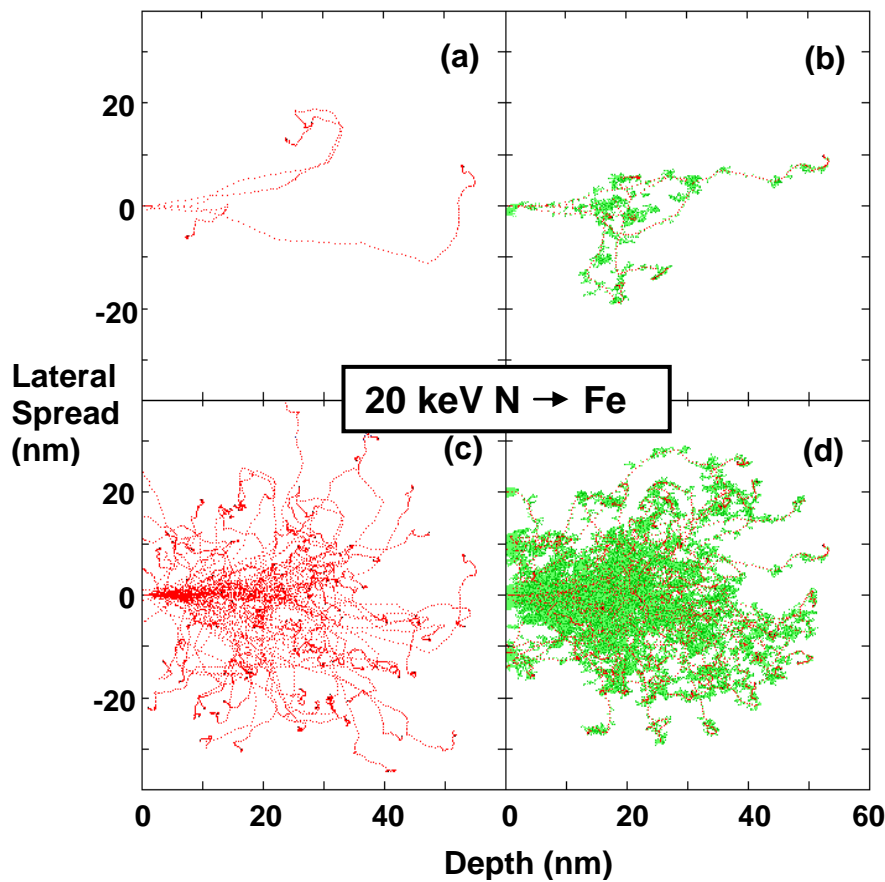


Fig. 11.3

Ion only (a,c) and ion plus recoil (b,d) trajectories for 20 keV nitrogen ions incident on iron, for 5 (a,b) and 100 (c,d) incident ions, as obtained from a TRIM computer simulation. The three-dimensional trajectories are projected onto a plane. Note that the pairs (a,b) and (c,d) each represent different runs with different ion trajectories.

The trajectories of each incident ion, and, if included in the simulation, all associated recoil atoms are traced in this way until the kinetic energy has fallen below the cutoff energy E_{co} , which again is chosen to several eV (see remark at the beginning of ch. 9).

Fig. 11.3 shows the spatial distributions of ion and recoil trajectories for 10 keV nitrogen ions in iron, as obtained from SRIM (Version 2000.39). In Fig. 11.3(a), it is evident that one of the 5 ions is backscattered. Fig. 11.3(b) indicates that, for the present ion-target combination, an individual ion creates several smaller subcascades with little overlap, in agreement with the qualitative picture of Fig. 9.2(top). The overlap of many incident ions (Fig. 11.3(d)) forms a cascade region which is similar to the region of the ion tracks (Fig. 11.3 (c)).

It should further be noted that the presentations of Fig. 11.3 assume that each ion enters the substance at exactly the same point. With this respect, the lateral extension of the ion deposition and cascade formation zone is artificial, since the beam spot of an ion beam on the surface extends over mm or cm dimensions in conventional ion implantation, and a few ten nm even in most advanced focused ion beam devices. The real lateral distribution is smeared out along the surface when many ions are implanted. Nevertheless, the lateral extension of the ion deposition and cascade formation can be physically meaningful and important for practical application, such as for masked ion implantation into microstructures.

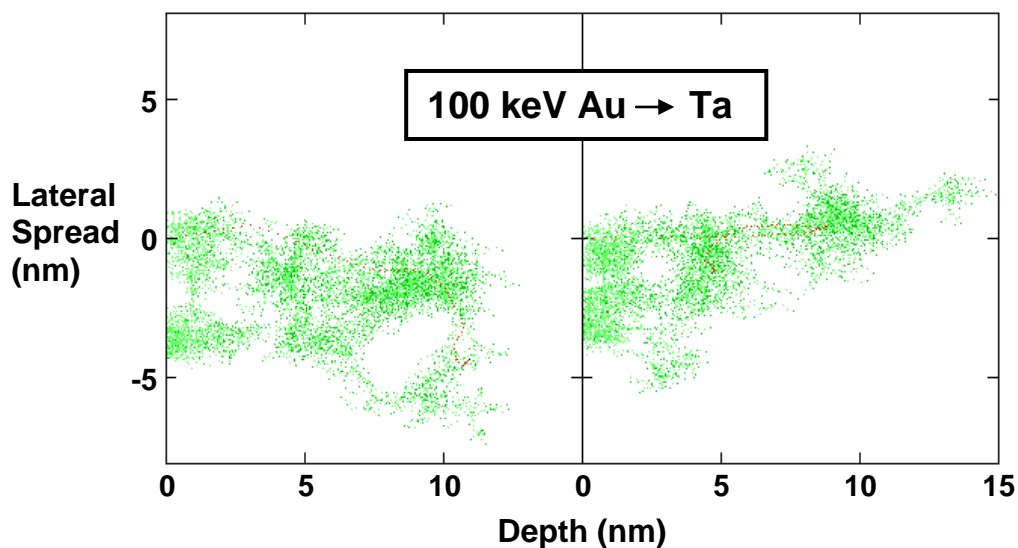


Fig. 11.4 Two different cascades triggered by one incident ion each, for 100 keV gold ions incident on tantalum.

For very high nuclear energy deposition, the space filling of the cascade is much more efficient already for one incident ion, as shown in Fig. 11.4. Although the result gets close to the schematic of Fig. 9.2 (bottom), still some subcascade formation is observed. (It has to be mentioned, however, that the linear cascade treatment becomes doubtful for the ion energy and ion-target combination of Fig. 11.4.)

For sufficiently many events of ion incidence, the distribution functions of, e.g., projected ion range of energy deposition can be obtained directly with sufficient statistical quality (see Fig. 11.5). Each incident ion in the computer (often called "pseudoprojectile") represents an increment of ion fluence (i.e. the number of incident ions per unit area)

$$\Delta\Phi = \frac{\Phi_{tot}}{N_H} \quad (11.14)$$

where Φ_{tot} denotes the total experimental fluence which shall be simulated and N_H the total number of pseudoprojectile histories chosen for the computer simulation. Each deposition or, e.g., recoil generation event is subject to the same pseudoparticle normalization, eq. (11.14). When a depth interval Δx is chosen for the sorting of these events and $N_p(x)$ of such events fall into the local depth interval, the resulting local atomic concentration, normalised to the host atomic density, is

$$c(x) = \frac{N_p(x) \Phi_{tot}}{n \Delta x N_H} \quad (11.15)$$

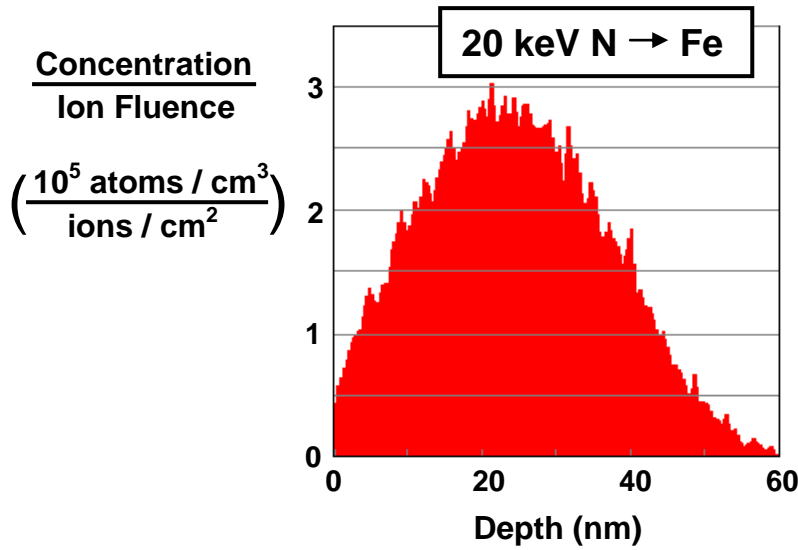


Fig. 11.5

Projected range distribution of 20 keV nitrogen ions implanted into iron, from a TRIM simulation with 20000 pseudoprojectiles (see Fig. 11.3). The mean projected range is $R_p = 24.5$ nm, the standard deviation $\sigma = 12$ nm, the skewness $\Gamma_1 = 0.19$, and the kurtosis $\Gamma_2 = 2.4$.

In this way, the ordinate of Fig. 11.5 is defined by $c(x)/\Phi_{tot}$. Nevertheless, it should be pointed out that standard TRIM computer simulations are only valid for the low-fluence limit, so that the results cannot readily be extrapolated to high fluences with, e.g., resulting implant concentrations close to stoichiometry or even above, which would be meaningless. In the BCA simulations discussed here, each incident projectile finds the same, unmodified substance that any effects of, e.g., ion deposition or surface erosion (see ch. 13) are neglected.

In a similar way, distribution functions of deposited energy can be obtained (Fig. 11.6). The electronic energy dissipation is sometimes called "ionisation" (such as in SRIM-2000), although the latter contributes only a fraction (see ch. 5). Also in SRIM-2000, the nuclear energy dissipation is called "energy to recoils". Note that the definition of nuclear energy dissipation is only meaningful for primary collisions of the incident ions with target atoms. For the complete cascade, the nuclear energy deposition vanishes as the nuclear collisions are elastic (or results from the lattice binding only). For the present ion-target combination, the total fractions of the ion energy which are dissipated into electronic and nuclear collisions are about equal, in agreement with the fact that electronic and nuclear stopping in the present energy range are about equal. The mean depth of electronic energy dissipation is somewhat lower than that of the nuclear counterpart, as electronic stopping decreases more rapidly with decreasing energy. Although the number of recoils exceeds the number of incident ions by orders of magnitude, the electronic contribution of the recoils to the energy distribution is small, due to their small average energy.

Finally a general comment related to BCA computer simulation shall be given. Obviously, the results depend critically on the choice of certain input parameters, such as the cutoff energy, but they depend also to a certain extent on "hidden" parameters such as the choice of the interatomic potential or the choice of the electronic stopping (see eqs. (11.7-9)). By varying these "hidden" inputs within reasonable limits, variations of the results for, e.g. ranges or energy deposition function, up to several 10% can be obtained. This depends, however, very much on the given problem and the energy range. Ion ranges obtained from TRIM are normally reliable within 10%.

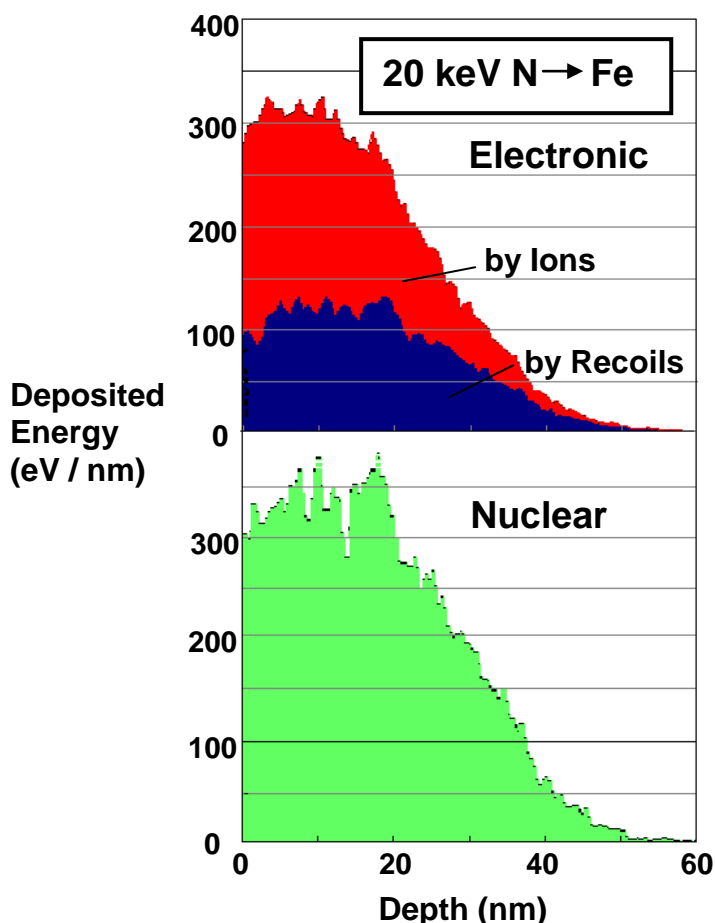


Fig. 11.6

Distribution of deposited energy into electronic (top) and nuclear (bottom) collisions for one 20 keV nitrogen ion implanted into iron, from a full-cascade TRIM simulation with 2000 pseudoprojectiles (see Fig. 11.3). The electronic fraction is split into the energy loss by the incident ions and by all recoil atoms in the collision cascade. The nuclear energy deposition results only from primary collisions (see text).

12. Radiation Damage

12.1 Analytical Treatment

The term "radiation damage of materials" covers a wide area of effects which can be observed after irradiation of a solid with energetic particles. In the present "collisional" picture in the linear-cascade regime (see beginning of ch. 9) only the initial stage of damage is considered, which is caused by the permanent displacement of lattice atoms from their original sites by the energy transfer received in nuclear collisions. It should be mentioned that, in particular in certain oxides but also in other materials at extremely high energy density which is deposited into electronic collisions, electronic energy dissipation can be converted into atomic displacement. Further, the restriction to the initial stage of damage applies only to selected physical situations. It represents a low-fluence approximation since any interaction of the resulting defects is neglected. It is also a low-temperature approximation since any thermal migration or recombination of the defects is neglected. However, the definition of low temperature in this context depends critically on the choice of the material. In metals, simple point defects may become mobile already at a few K, whereas they are stable around room temperature in common semiconductors.

Fig. 12.1 depicts the elementary event of radiation damage schematically. In order to produce a "stable" Frenkel pair consisting of a vacancy at the original site of the recoil and an interstitial atom at its final position, the distance between the interstitial-vacancy has to be sufficiently large so that an immediate recombination due to elastic forces in the lattice and/or due to directed atomic bonds is prevented. Therefore, the initial energy transfer to the recoil has to be sufficiently large. This critical energy transfer depends on the crystalline direction into which the recoil is set into motion. Therefore,

the "displacement threshold" energy U_d must be understood as an average over different directions. Thus, for any recoil starting with an initial energy transfer T below the threshold energy, the number of generated Frenkel pairs is close to zero, even if secondary recoils in a subsequent collision cascade are taken into account.

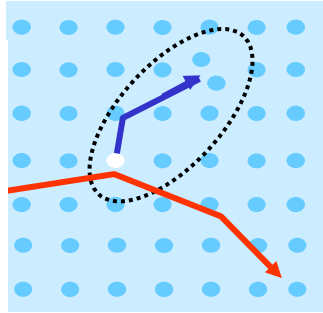


Fig. 12.1

Elementary radiation damage event in a collision cascade. A recoil atom generated by a nuclear collision is moved from its original site into an interstitial position, thus forming a vacancy- interstitial or "Frenkel" pair.

After terminating the collision cascade, a stable Frenkel pair is characterised by its formation energy U_f , i.e. the gain of potential energy with respect to the undisturbed lattice, with a contribution from the vacancy and the interstitial atom:

$$U_f = U_{vf} + U_{if} \quad (12.1)$$

Apparently, the bulk binding energy U_b is smaller than the Frenkel pair formation energy. On the other hand, the displacement threshold energy must be larger than the Frenkel pair formation energy since kinetic energy is dissipated during the slowing down of the recoil. Thus

$$U_b < U_f < U_d \quad (12.2)$$

Typical bulk binding energies are a few eV, compared to Frenkel pair formation energies of 5 to 10 eV and displacement threshold energies of 20 to 80 eV.

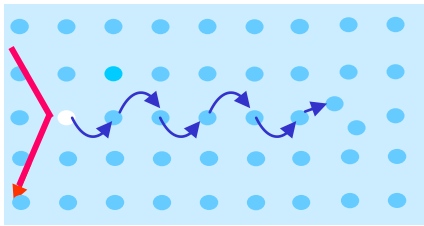


Fig. 12.2

Schematic of a replacement collision sequence.

There are other mechanisms than the simple transfer of a recoil depicted in Fig. 12.1. For low recoil energies, so-called "replacement" collision sequences become increasingly important (Fig. 12.2), which travel in particular in low-indexed directions of a crystal being "focussed" by the potential resulting from the surrounding atoms, but contribute significantly even in amorphous materials. In head-on sequences, the nuclear energy loss is effectively switched off in homonuclear materials, so that the range can become rather large (up to a few hundred atomic distances).

With these considerations, a displacement probability can be defined for each recoil starting with an energy E_0 , according to

$$P_d(E_0) = \begin{cases} 0 & \text{if } E_0 < U_d \\ \frac{E_0 - U_d}{U_d} & \text{if } U_d < E_0 < 2U_d \\ 1 & \text{if } E_0 > 2U_d \end{cases} \quad (12.3)$$

which is depicted in Fig. 12.3. The middle expression of eq. (12.3) shall, in a rather handwaving way, take into account the reduction of Frenkel pair production per recoil atom due to replacement collisions at low energy transfers, as many correlated over-threshold recoils generate only one Frenkel pair.

The total number of Frenkel pairs for one recoil atom starting with energy T , including the complete associated cascade, is then given by

$$N_F(T) = \int_{U_d}^T P_d(E_0) \cdot F_E(T, E_0) dE_0 \quad (12.4)$$

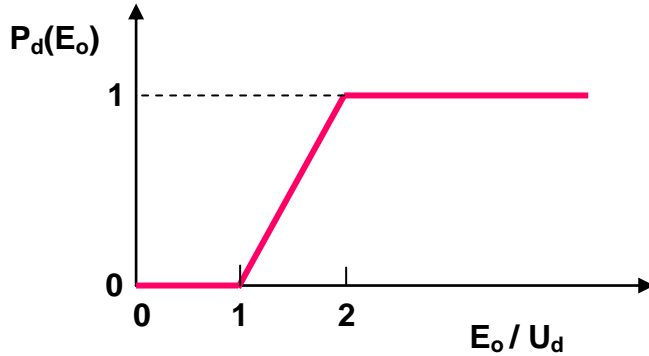


Fig. 12.3

Displacement probability model employed for the modified Kinchin-Pease model.

with F_E denoting the recoil density (see sect. 10.3). Inserting eqs. (10.35) and (12.3) results in

$$N_F(T) = \frac{6 \log 2}{\pi^2} \frac{v(T)}{U_d} = 0.42 \frac{v(T)}{U_d} \quad (12.5)$$

This is the so-called "modified Kinchin-Pease" formula. It has to be noted that the bulk binding energy is implicitly neglected (see sect. 10.3). Originally, Kinchin and Pease had treated the problem using hard spheres rather than a screened Coulomb potential, and consequently neglecting inelastic energy loss, resulting in

$$N_F(T) = \frac{T}{2U_d} \quad (12.6)$$

which, compared to (12.4), makes hardly a difference in view of the theoretical approximations and the experimental uncertainties in determining N_F . Formally, eq. (12.4) allows for subthreshold damage, too. Therefore, a corrected formula is often employed, where eq. (10.34) for the nuclear deposited energy has already been used:

$$N_F(T) = \begin{cases} 0 & \text{if } T < U_d \\ 1 & \text{if } U_d < T < 2.63 \cdot U_d \\ 0.38 \frac{T}{U_d} & \text{else} \end{cases} \quad (12.7)$$

The energy range of the middle contribution guarantees a continuous transition to the modified Kinchin-Pease formula.

The total number of Frenkel pairs generated by an incident ion of energy E is obtained by integrating $N_F(T)$ according to the cross section of nuclear collisions and along the ion path:

$$N_F^{tot}(E) = \int_0^E \frac{dE'}{S_{tot}(E')} \int_{U_d}^{\gamma E'} N_F(T) \frac{d\sigma_n(E', T)}{dT} dT \quad (12.8)$$

where γ denotes the energy transfer factor (eq. (1.7)). Inserting the simple Kinchin-Pease result, eq. (12.6), for simplicity, and assuming an average energy transfer $\gamma E'$ which is large compared to the displacement threshold, the inner integral in (12.8) can, in reasonable approximation, be replaced by the nuclear stopping cross section S_n . For such a "dense cascade", which occurs for large nuclear energy deposition, electronic stopping is small, so that $S_{tot} \approx S_n$. Thus, in the dense cascade approximation, the total damage is given by the simple Kinchin-Pease expression with the incident energy:

$$N_F^{tot}(E) = \frac{E}{2U_d} \quad (12.9)$$

All above results for the Frenkel pair generation represent an upper limit since a certain amount of "dynamic annealing" will take place already in the collisional phase, given by the probability of recombination of interstitial atoms with vacancies. This probability of dynamic recombination increases with increasing cascade density. In this sense, a "cascade efficiency" $\xi(T)$ is defined so that the effective number of Frenkel pairs is given by

$$N_F^{eff}(T) = \xi(T) \cdot N_F(T) \quad (12.10)$$

The cascade efficiency is between 1 in the low-density limit (e.g., light ions) and about 0.3 for very dense cascades for heavy ions with large nuclear stopping.

12.2 TRIM Computer Simulation

There are two different possibilities to treat damage in TRIM computer simulations. In the so-called "quick" calculation of damage just the ion trajectory is traced rather than the complete collision cascade. For each primary collision with energy transfer T to the primary recoil, eq. (12.6) is applied for the generation of Frenkel pair at each primary nuclear collision. In addition to the approximations implied in the Kinchin-Pease formula, this simplified simulation neglects the spatial extension of the individual subcascades. If the latter is small compared to the ion range, such as for light ions or at sufficiently high energy, the error with respect to the depth distribution remains small.

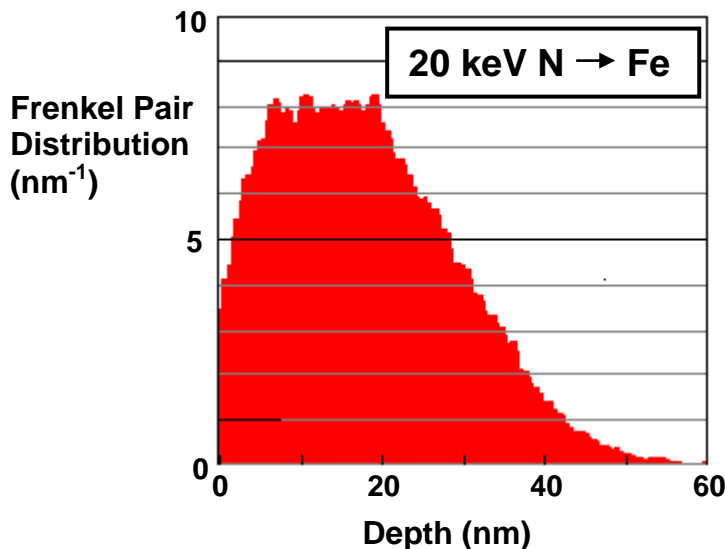


Fig. 12.4

Depth distribution of Frenkel pairs generated by one 20 keV nitrogen ion incident on iron, as obtained from a full cascade TRIM computer simulation with 2000 pseudoprojectiles, with a displacement threshold energy of 25 eV. The average total number of Frenkel pairs per ion is 240.

The more time-consuming "detailed calculation with full cascades" generates all recoils with initial energies exceeding the threshold U_d , so that all events can simply be counted. Fig. 12.4 shows the depth distribution of Frenkel pairs for nitrogen ions incident on iron obtained from a "full cascade" simulation. The depth distribution follows the distribution of nuclear energy deposition (see Fig. 11.6), with a total number of Frenkel pairs which exceeds the number of implanted ions by more than two orders of magnitude. Compared to 240 Frenkel pairs per incident ion obtained from the computer simulation, the simple Kinchin-Pease dense-cascade approximation (eq. (12.9)) yields an overestimated, but rather close number of 400. In a dense-cascade situation, for 100 keV gold ions incident on tantalum (see Fig. 11.4), the number obtained from TRIM (2075) compares well with the prediction of eq. (12.9) (2000). By definition of the binary collision approximation, any dynamic annealing in the cascade (see eq. (12.10)) is not taken into account.

Note that the Frenkel pairs are often called "vacancies" in TRIM. Quite formally, the middle regimes of eqs. (12.3) and (12.7) can be used in TRIM, as available from the SRIM package, to count the contributions of replacement collisions in full-cascade and quick simulations, respectively. The contribution is generally minor (in the order of 10% of the Frenkel pairs). The different regimes of (12.3) and (12.7) can also be used to discriminate the energetics of the cascade. The energy which goes into subthreshold recoils is called the "phonon" fraction. (Clearly, the final energy will be transferred into heat, i.e. phonons, even if the BCA simulation is far from treating any recoil-phonon coupling in a solid.) On the other hand, over-threshold recoils form the energy which is dissipated into "damage".

13. Sputtering

13.1 Analytical Treatment

When a collision cascade intersects the surface, sufficient energy can be transferred to a surface atom to overcome its binding to the surface, so that it will be ejected from the solid. A schematic presentation of sputtering in the linear cascade regime is given in Fig. 13.1.

The sputtering yield is defined as the number of emitted target atoms per incident ion:

$$Y = \frac{j_{sp}}{j_i} \quad (13.1)$$

where j_i and j_{sp} denote the flux of incident ions and sputtered atoms, respectively.

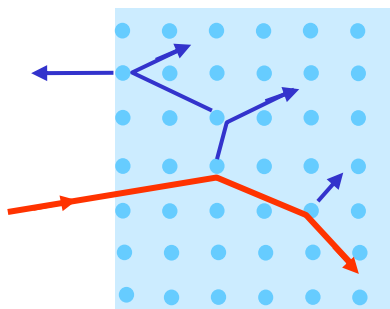


Fig. 13.1

Schematic presentation of a sputtering event in the linear cascade regime.

Applying cascade transport theory, now - in contrast to the treatment of radiation damage - the spatial development of the cascade has to be taken into account in addition to the energetics, as the surface introduces a local character. Further, the ejection of a surface atom may - according to the surface binding model which will be described below - depend on its ejection angle with respect to the surface normal, i.e. on its starting direction within the cascade. Therefore, an isotropic angular distribution of cascade atoms is added to the spatial cascade energy function, eq. (10.41),

$$F(E, \bar{\eta}, E_0, \bar{\eta}_0, \bar{r}) = \frac{6}{4\pi^3} \frac{F_D(E, \bar{\eta}, \bar{r})}{E_0^2} \quad (13.2)$$

The number of cascade atoms per energy interval starting into the direction η_0 is then obtained by integrating over the volume (geometry is indicated in Fig. 13.2):

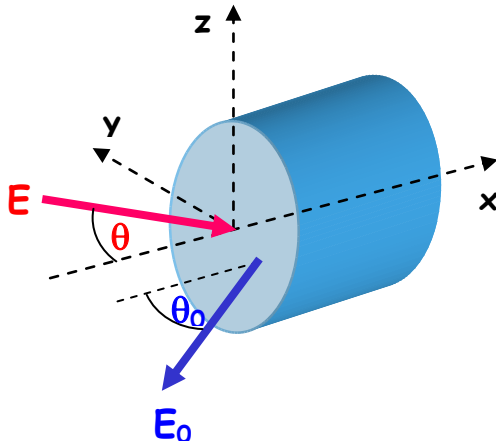


Fig. 13.2

Geometry of a near-surface collision cascade (idealized by a cylindrical volume) formed by an ion of energy E and angle of incidence θ , with a subsurface cascade atom of energy E_0 and at an angle θ_0 with respect to the surface normal.

$$\frac{d^2Y}{dE_0 d\omega_0} = \frac{6}{4\pi^3} \frac{1}{E_0^2} \int_0^{\Delta x} dx \int_{-\infty}^{\infty} d\bar{r} \cdot F_D(E, \bar{\eta}, \bar{r}) \cdot \bar{\eta}_0 \cdot P(E_0, \theta_0) \quad (13.3)$$

where df denotes the surface element. Δx is a shallow depth element from which recoil atoms contribute to sputtering, and P denotes the probability that a recoil at energy E_0 and angle θ_0 is transmitted through the surface. The surface integral yields the one-dimensional damage function which is assumed to be constant over Δx with its value at the very surface, resulting in

$$\frac{d^2Y}{dE_0 d\omega_0} = \frac{6}{4\pi^3} \frac{F_D(E, \bar{\eta}, \theta)}{E_0^2} \cdot \Delta x \cdot \cos \theta_0 \cdot P(E_0, \theta_0) \quad (13.4)$$

Δx , which may depend on E_0 , can be estimated in the following way: At maximum those recoils can contribute to sputtering which lose all their energy within Δx . Then, with $E_0/\Delta x \approx |dE_0/dx|$, where the latter denotes the stopping power of the recoils

$$\frac{d^2Y}{dE_0 d\omega_0} = \frac{6}{4\pi^3} \frac{F_D(E, \bar{\eta}, \theta)}{E_0 |dE_0/dx|} \cdot \cos \theta_0 \cdot P(E_0, \theta_0) \quad (13.5)$$

It should be noted that eq. (13.5) can also be obtained from a more rigorous treatment of the recoil fluxes for a stationary incident beam, without the simple assumption on Δx . The sputtering yield results as

$$Y = \frac{6}{2\pi^2} \int \frac{dE_0}{E_0 |dE_0/dx|} \int d(\cos \theta_0) \cdot \cos \theta_0 \cdot P(E_0, \theta_0) \cdot F_D(E, \bar{\eta}, \theta) \quad (13.6)$$

For the surface penetration probability, a planar surface model is employed with a threshold being equal to the surface binding energy U_s , which has to be overcome by the normal fraction of the recoil energy:

$$P(E_0, \theta_0) = \begin{cases} 1 & \text{if } E_0 \cos^2 \theta_0 > U_s \\ 0 & \text{else} \end{cases} \quad (13.7)$$

The stopping of the recoils is represented by their nuclear stopping in an approximation using the power law potential, eq. (2.16), yielding for $m \rightarrow 0$

$$S_n(E_0) = \frac{\pi}{2} \lambda_0 a^2 E_0 \quad (13.8)$$

where λ_0 denotes a power law constant and a the screening distance. Then, integration of (13.6) results in

$$Y(E, \theta) = \frac{3}{4\pi^2} \frac{2}{\pi \lambda_0 a^2 n} \cdot \frac{F_D(E, \bar{\eta}, \theta)}{U_s} \quad (13.9)$$

The damage function is approximated by the nuclear energy deposition of the incident ion. However, it has to be recalled that the transport theory is valid for the cascade evolution in an infinite medium with an internally starting ion, with an artificial surface plane to calculate the sputtering yield, so that the sputtering yield will be overestimated the more as a significant fraction of the cascade forms beyond the "surface" in the infinite medium. This will mainly depend on the masses of the incident ion and the target material: For large incident ion mass, the real cascade will mainly develop in forward direction, so that the error remains small, whereas for light ions the probability of momentum reversal increases. Therefore, a correction factor α is applied. The theoretical calculation of α is complicated and only successful for high ion-to-target mass ratios. Therefore, a numerical fit obtained from comparisons of experimental results to eq. (13.10) is employed, which is shown in Fig. 13.3.

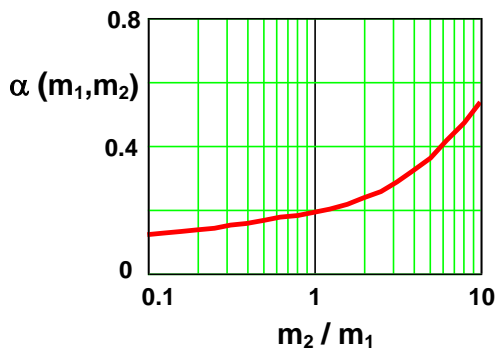


Fig. 13.3

Dependence of the correction factor α , eq. (13.10), on the target-to-ion mass ratio.

The sputtering yield then results according to

$$Y(E, \theta) = \frac{3}{2\pi^3} \frac{1}{U_s} \frac{S_n(E)}{\lambda_0 a^2} \cdot \alpha(m_1, m_2) \cdot \frac{1}{\cos \theta} \quad (13.10)$$

where the last factor describes the simple geometrical dependence of the deposited energy in the surface layer as function of the angle of incidence.

For the evaluation of (13.10), the sublimation enthalpy is normally inserted as surface binding energy for one-component materials, which amounts to about 2 ... 8 eV. For the very low energies of most of the recoils, $\lambda_0 \approx 24$ and $a \approx 0.022$ nm are reasonable values with universal validity.

Due to the approximations involved in its derivation, the final sputtering yield formula (13.10) neglects the fact that at very low ion energy the maximum energy transfer to target recoils can be lower than the surface binding energy so that sputtering is excluded. A particular situation arises for light ions, where also the single-collision regime (see Fig. 9.3a) is more appropriate which is difficult to be treated by transport theory. For light ions, the characteristic single-collision-regime sputtering event occurs after backscattering of the ion, as depicted in Fig. 13.4. For this situation with single backscattering of the ion, the maximum energy is received by the surface atom for 180° backscattering of the ion and a head-on collision with the surface atom:

$$E_0^{max} = \gamma(I - \gamma)E \quad (13.11)$$

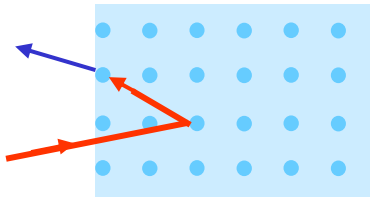


Fig. 13.4

Light-ion sputtering event in the single-collision regime.

from which a sputtering threshold energy of the incident ion can be derived according to

$$E_{thr} = \frac{U_s}{\gamma(I - \gamma)} \quad (13.12)$$

However, the ion could also be backscattered by two subsequent collisions at about 90° , which would result in a larger final energy at the surface compared to one 180° collision when electronic energy loss is neglected, or by a series of small-angle scattering events with even higher final energy, which becomes increasingly improbable and which would finally be influenced by significant electronic energy loss. Thus, it is not readily feasible to define an exact threshold energy for sputtering. Semiempirical formulas have been proposed to include threshold effects, partly based on fits to experimental results, such as (for normal incidence)

$$Y_s^{thr}(E) = Y(E) \cdot g\left(\frac{E}{E'_{thr}}\right) \quad (13.13)$$

with the correction function

$$g(\xi) = (1 - \xi^{3/2})(1 - \xi)^2 \quad (13.14)$$

and a modified expression for the threshold energy

$$E'_{thr} = \begin{cases} \frac{U_s}{\gamma(I - \gamma)} & \text{if } \frac{m_1}{m_2} < 0.2 \\ 8U_0 \left(\frac{m_1}{m_2}\right)^{2/5} & \text{else} \end{cases} \quad (13.15)$$

The sputtering yield for nitrogen ions incident on iron, according to eqs. (13.10) and (13.15), is shown in Fig. 13.5. The threshold correction reduces the sputtering yield at low energies significantly. As linear cascade sputtering scales with the nuclear stopping, the maximum sputtering yields are between about 0.01 for light ions and 50 for the heaviest ions, corresponding to energies between about 100 eV and 100 keV.

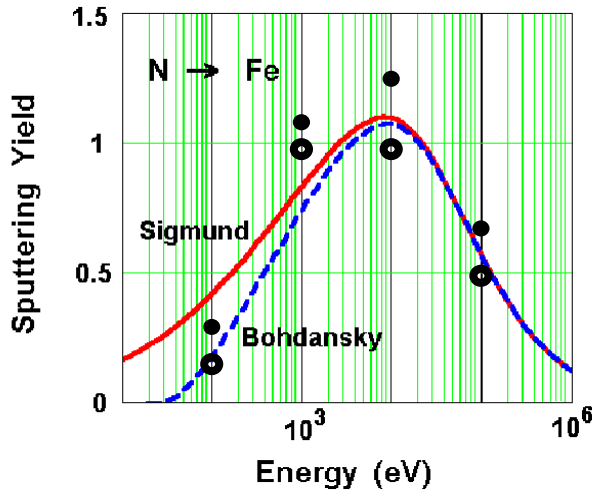


Fig. 13.5

Sputtering yield versus ion energy for nitrogen ion at iron at normal incidence, from the Sigmund formula (solid line, eq. (13.10)), the Bohdansky formula (dashed line, eqs. (13.13-15)) and different TRIM simulations, from SRIM vs. 2000.39 (dots), and TRIDYN vs. 4.0 (see ch. 15) (circles).

An early comparison to experimental data is shown in Fig. 13.6 for different rare gases incident on copper. There is a very good agreement between experiment and the prediction of eq. (13.10), except for the highest energy densities around the nuclear stopping power maximum for the heaviest projectile, xenon. This inconsistency is attributed to a significant influence of thermal spikes on sputtering.

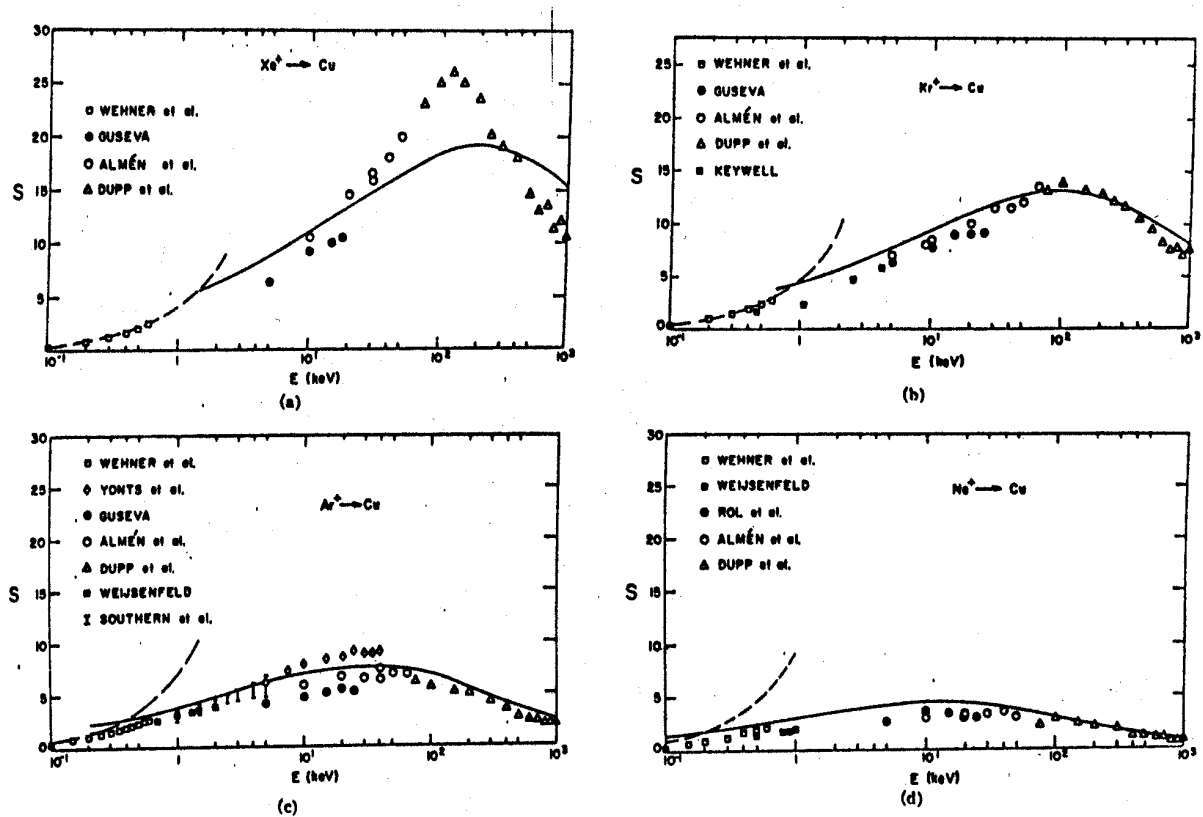


Fig. 13.6 Experimental data and theoretical predictions of sputtering yields vs. ion energy, for the bombardment of copper with different rare gases at normal incidence. Different symbols correspond to different data sets. Solid lines are from eq. (13.10), dashed lines from a low-energy approximation to nuclear stopping.

In the planar surface model, a recoil arriving at the surface is emitted if its energy is sufficiently large and its directional angle sufficiently small (see Fig. 13.7). The planar surface potential reduces the energy of the sputtered atoms and deflects their trajectories. With the parallel velocity component conserved and the normal velocity component reduced, the energy E_1 and the ejection angle θ_1 of a sputtered atom are given by the equation set

$$\begin{aligned} E_1 \cos^2 \theta_1 &= E_0 \cos^2 \theta_0 - U_s \\ E_1 \sin^2 \theta_1 &= E_0 \sin^2 \theta_0 \end{aligned} \quad (13.16)$$

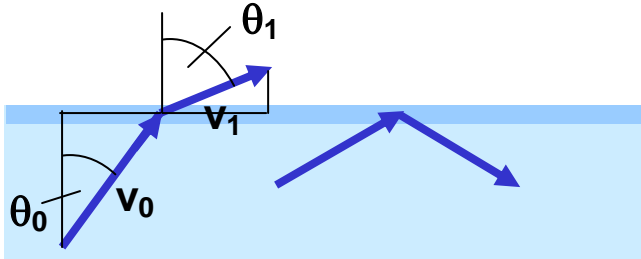


Fig. 13.7

Schematic of a sputtered (left) and a backreflected recoil, in the model of a planar surface threshold.

Eq. (13.5) then yields the energy and angular distribution of sputtered atoms (for normal ion incidence)

$$\frac{d^2 Y}{dE_1 d\omega_1} = \frac{6}{4\pi^3} F_D(E, \bar{\eta}, \theta) \frac{2}{\pi \lambda_0 a^2} \frac{E_1}{(E_1 + U_s)^3} \cdot \cos \theta_1 \quad (13.17)$$

The cosine dependence of the angular distribution is a consequence of the assumption of an isotropic cascade. The functional shape of the energy distribution ("Thompson" distribution) is shown in Fig. 13.8 in logarithmic presentation. The distribution peaks at half the surface binding energy, but has a rather broad tail towards higher energies.

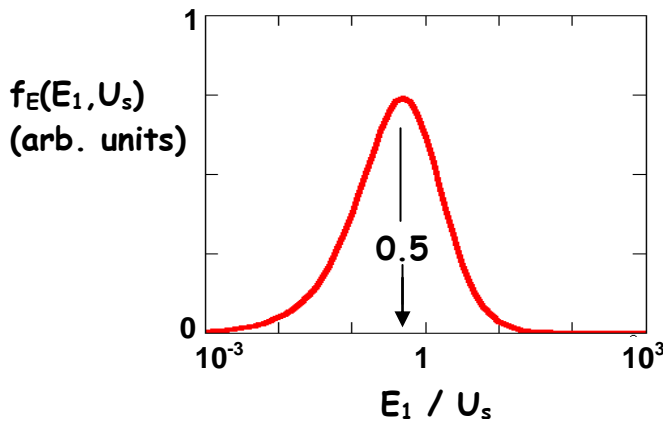


Fig. 13.8

Energy distribution of sputtered particles, normalised to the surface binding energy.

Integration with the upper limit of the incident energy yields the mean energy of sputtered particles

$$\bar{E}_1 \approx U_s \left(2 \log \frac{E_1}{U_s} - 3 \right) \quad (13.18)$$

For an incident energy of 1 keV, which is typical for thin film deposition by sputtering, a typical surface binding energy of about 4 eV results in a mean energy of sputtered atoms of about 30 eV.

13.2 TRIM Computer Simulation

Naturally, BCA computer simulations can also be applied to predict sputtering yields as well as angular and energy distributions, after including the planar surface threshold model as shown in Fig. 13.17, and applying eqs. (13.7) and (13.16). Special results of sputtering yields calculated by TRIM are included in Fig. 13.5 and found in reasonable agreement with the analytical predictions. As stated in ch. 11, the results depend on the choice of hidden parameters. For sputtering simulations, the choice of the interatomic potential and the bulk binding energy are of particular importance, in addition to the surface binding energy. Further, the treatment of electronic stopping can be of significant influence. Therefore, different versions of TRIM do not necessarily deliver identical sputtering yields, as seen in Fig. 3.17. Nevertheless, the differences are normally small in view of other uncertainties. It can be concluded that, provided that all parameters are chosen within reasonable limits, sputtering yields of all elemental targets can be simulated with a precision of about 50%.

With respect to analytical sputtering calculations, a real advantage of the computer simulations is their ability to cover the sputtering by light ions, where the transport theory for the infinite medium is in large error due to the neglect of the surface, and which is often associated with the single-collision regime. Fig. 13.9 demonstrates an excellent agreement with experimental data for the sputtering of nickel with different gaseous ions over a large range of energies and for widely different sputtering yields, in particular also for the lightest ions.

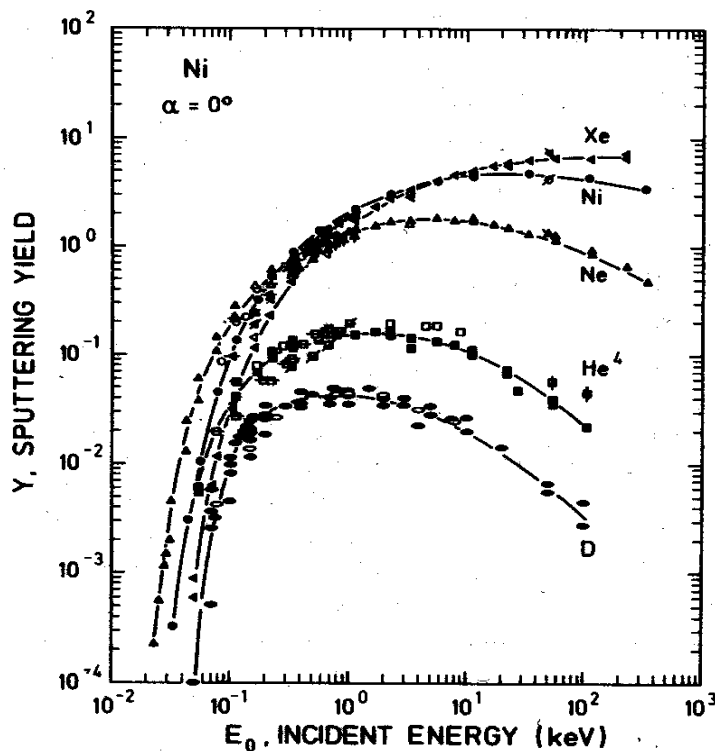


Fig. 13.9

Sputtering yield of gaseous ions at normal incidence onto nickel, from experiment (open symbols) and TRIM computer simulations (crosses, full symbols). The lines are drawn to guide the eye.

14. Thermal Spikes

The treatment of thermal spikes (see ch. 9) in literature is much less rigorous than for the linear cascade regime, as a complicated situation arises in the transition between dense linear cascades and an effective thermalisation of the atoms in a cascade. However, more recent molecular dynamics computer simulation, which are not the subject of the present presentation, have gained increased information on this regime.

It should be noted that here we still cover "collisional" spikes, i.e. at energies above about 1 eV which are of interest for the formation of defects and for sputtering. Thermal spikes in a more general sense will result from any cascade which finally will thermalise towards the temperature of the surrounding material. Atomic rearrangements with low activation energies may still occur at such low energies, but will not be the matter of the present discussion.

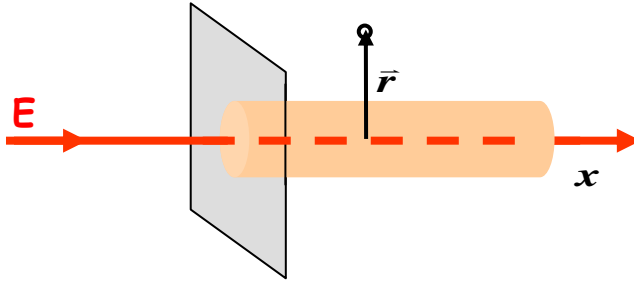


Fig. 14.1

Simplified picture of a cylindrical thermal spike

For a simple picture of a thermal spike (Fig. 14.1), the evolution of a cylindrical cascade around a linear ion track is assumed, which is justified at large ion masses and high energy. Neglecting energy loss, the system is translationally invariant in the direction of the depth x . For simplicity, a zero temperature of the material is assumed as initial condition. At $t = 0$, the time of the ion incidence, energy is deposited within a negligible time interval along the ion track, with the energy deposition function being idealised by an areal δ function in circular symmetry, leading to an initial temperature in the track according to

$$\left| \frac{dE}{dx} \right| \delta(\bar{r}) = \rho c T(r, t = 0) \quad (14.1)$$

with the normalisation

$$\int 2\pi r \delta(\bar{r}) dr = 1 \quad (14.2)$$

In eq. (14.1), ρ and c denote the mass density and the specific heat of the material, respectively. Around the track, a thermal wave develops in radial direction according to the law of thermal diffusion

$$\frac{\partial T}{\partial t} = \frac{\lambda}{\rho c} \Delta T = \frac{\lambda}{\rho c} \frac{1}{r} \frac{\partial}{\partial r} \left(r \frac{\partial T}{\partial r} \right) \quad (14.3)$$

with the thermal conductivity λ . The solution yields the temperature at radial distance r as function of time t :

$$T(r, t) = \left| \frac{dE}{dx} \right| \frac{1}{4\pi\lambda t} \exp\left(-\frac{\rho c r^2}{4\lambda t}\right) \quad (14.4)$$

which fulfills eq. (14.1) as

$$\frac{1}{\pi\tau} e^{-\frac{r^2}{\tau}} \xrightarrow{\tau \rightarrow 0} \delta(\bar{r}) \quad (14.5)$$

Fig.14.2 shows a solution for a special case. Close to the ion track, temperatures of a few 10^4 K (corresponding to a few eV) are predicted, so that the material will be liquified and probably be evaporated. The thermal pulse dissipates quickly at larger distance from the track. The characteristic time scale, however, demonstrates an inherent contradiction, as it is in the order of one lattice vibration period only, so that the above continuum picture is hardly valid.

It makes little sense to apply the thermal spike picture to the formation of radiation damage, since radiation damage in a liquid is meaningless, and since excessive dynamic annealing will occur at the very high temperature after solidification or at radii where the substance remains in the solid phase. However, one may attempt to calculate sputtering in the thermal spike picture.

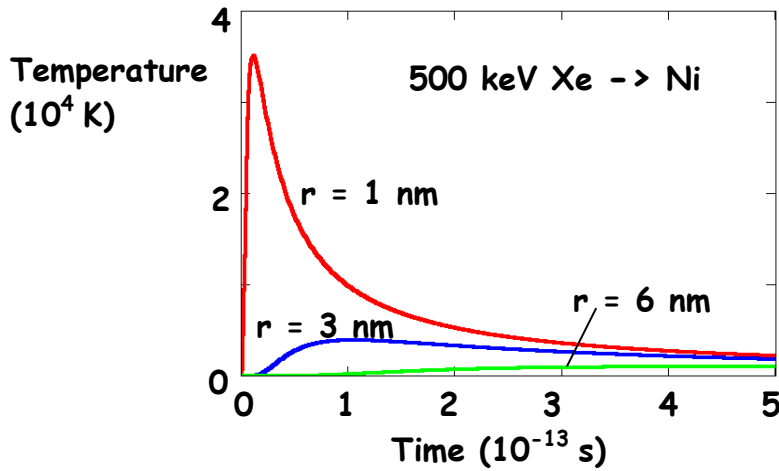


Fig. 14.2

Thermal pulse at different radial locations for 500 keV xenon ions incident onto nickel

Sputtering is modelled by the evaporation from the thermal spike at the surface. For a Maxwellian energy distribution of atoms with mass m , the energy of which exceeds the surface binding energy, the outward flux is given by

$$j(r,t) = n \sqrt{\frac{kT(r,t)}{2\pi m_2}} \exp\left(-\frac{U_s}{kT(r,t)}\right) \quad (14.6)$$

Thereby, the sputtering yield results according to

$$Y = 2\pi \int_0^\infty r dr \int_0^\infty dt \cdot j(r,t) \quad (14.7)$$

With the approximation $\rho \cdot c \approx 3nk$ for the specific heat, the integration yields

$$Y = \frac{\Gamma(3/2)}{24\sqrt{2}\pi^{3/2}} \frac{k}{\lambda\sqrt{m_2}} \frac{1}{U_s^{3/2}} \left| \frac{dE}{dx} \right|^2 \quad (14.8)$$

which shows the nonlinear dependence on the stopping power in the thermal spike regime.

For the example of xenon in copper the maximum nuclear stopping power is chosen, which is about 6.5 MeV/ μm at an energy of about 250 keV. (At this energy, electronic stopping contributes only about 10% to the total stopping.) With the room temperature value of the thermal conductivity, the evaluation of eq. (14.8) yields a sputtering yield of $Y \approx 1$. However, the thermal conductivity in the liquid might be smaller by a factor of 2 or 3. Nevertheless, the result is still significantly below the difference of experimental data and linear cascade prediction in Fig. 13.6, indicating that the above formalism might be insufficient to treat the sputtering from a thermal spike.

15. High-Fluence Phenomena

The preceding chapters did only cover low-fluence phenomena, i.e. the dynamic alteration of the target substance due to ion implantation or the formation of defects has been neglected so far. Sputtering yields can be extrapolated to large fluences as long as the material remains unchanged during sputtering. This does not hold for the sputtering of multicomponent substances, where the collision cascades or preferential sputtering may change the surface composition even in a homogeneous material, and/or modify the local composition of a layered substance.

15.1 Dynamic Binary Collision Approximation Computer Simulation

The BCA computer simulation of ion bombardment and collision cascade formation can be modified in a straightforward manner to treat dynamic compositional changes of the substance. Here, the TRIDYN code will be described which is based on TRIM.

A multicomponent material with atomic components denoted by j ($j = 1, \dots, M$) is modelled, where one or more of these components may be attributed to species of the incident beam. An arbitrary local stoichiometry can be chosen, represented by discrete depth intervals Δx_i ($i = 1, \dots, N$). Each depth interval is characterised by the fractional compositions q_{ij} with

$$\sum_{j=1}^M q_{ij} = 1 \quad (15.1)$$

and a total atomic density n_i given by

$$\frac{1}{n_i} = \sum_{j=1}^M \frac{q_{ij}}{n_{j0}} \quad (15.2)$$

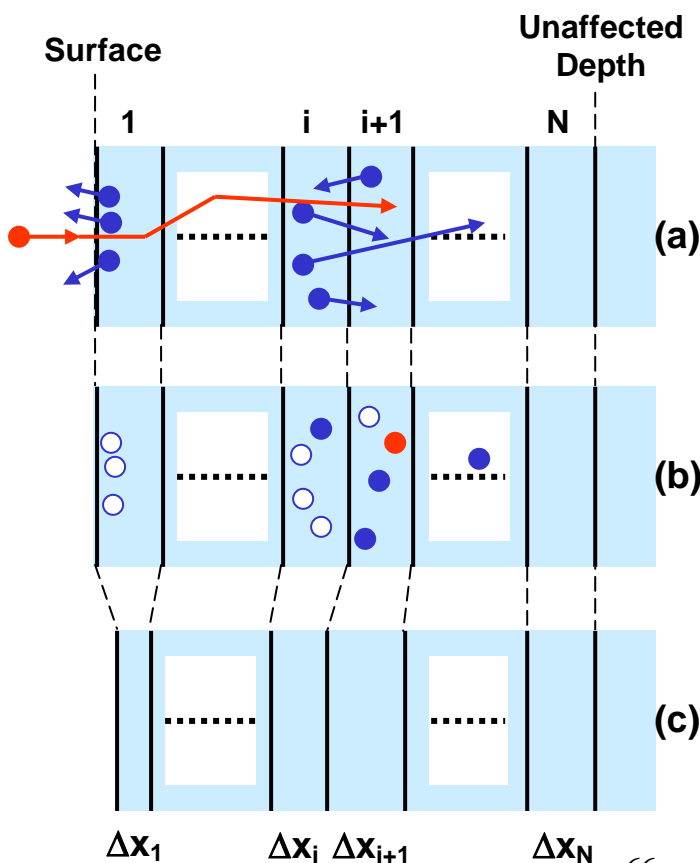


Fig. 15.1

Scheme of the dynamic computer simulation in binary collision approximation (TRIDYN).
 (a) A pseudoprojectile is implanted and generates sputtering and recoil atoms.
 (b) "Vacancies" and "interstitial atoms" are left behind.
 (c) The individual slabs relax.

where n_{j0} ($j = 1, \dots, M$) denotes the elemental atomic densities of the pure component j , i.e. the inverse of the atomic volume of species j . The elemental atomic densities are fixed input parameters, i.e. any atomic volume changes due to chemical effects are neglected.

The principle of the TRIDYN simulation is schematically shown in Fig. 15.1. The depth of interest is initially subdivided into N slabs of equal thickness Δx_0 . The slowing down of the first pseudoprojectile and its associated collision cascades are simulated. Ion implantation, sputtering and recoil relocation result in the addition and/or the removal of "pseudoatoms" to/from certain depth intervals. Each of such events represents a change of the areal densities of real atoms in the affected slabs according to the pseudoprojectile normalisation, eq. (11.14). Denoting the change of the number of pseudoatoms of species j in each layer i by ΔN_{ij} , the new areal densities of any species j in each layer i is given by

$$A_{ij} = q_{ij} n_i \Delta x_i + \Delta N_{ij} \quad (15.3)$$

Depth intervals i with $\Delta N_{ij} \neq 0$ for at least one j may then be compressed or diluted with respect to their nominal density given eq. (15.2), and are allowed to relax according to

$$\Delta x_i = \sum_{j=1}^M \frac{A_{ij}}{n_{0j}} \quad (15.4)$$

which restores the nominal density. The new relative local fractional compositions result as

$$q_{ij} = \frac{A_{ij}}{\sum_{k=1}^M A_{ik}} \quad (15.5)$$

By this procedure, certain slabs may become very thin or excessively thick. These are added to a neighbouring slab or split into two slabs of half thickness, respectively. In TRIDYN, the conditions for slab combination and splitting are $\Delta x_i < 0.5 \Delta x_0$ and $\Delta x_i > 1.5 \Delta x_0$, respectively.

After relaxation, the next pseudoprojectile is simulated, and the complete procedure is repeated for the chosen total number N_H of pseudoprojectiles, corresponding to a fluence Φ_{tot} of incident ions (see eq. (11.14)). For a given fluence, the number of pseudoprojectiles has to be chosen sufficiently large in order to obtain a sufficient statistical quality of the result. At an excessively small total number of pseudoprojectiles, the number of added or removed atoms per pseudoprojectile in certain slabs may even exceed the total number of atoms in that slab, which has to be avoided. As a rule of experience, the number of atoms in any slab should not change by more than about 5% per pseudoprojectile throughout the whole run in order to avoid artefacts.

15.2 Local Saturation

Towards high fluence, the relative atomic concentration $c_i(x,t)$ of an implanted species with the range distribution $f_R(x)$ increases according to

$$\frac{\partial}{\partial t} c_i(x,t) = \frac{I}{n} j_i f_R(x) \quad (15.6)$$

where n denotes the atomic density of the target substance and j_i the incident ion flux. The simplest approach to high-fluence implantation profiles is to neglect any changes in n and f_R , which arise from the presence of the implanted species, and thereby just to scale the range distribution, so that

$$c_i(x, \Phi) = \frac{I}{n} f_R(x) \cdot \Phi \quad (15.7)$$

where Φ denotes the implanted fluence. Eq. (15.7) neglects any relaxation of the target substance and is thus strictly valid only for small relative concentrations. The relative concentration can be turned into the fractional composition of the implanted species according to

$$q_i = \left(1 + c_i^{-1}\right)^{-1} \quad (15.8)$$

In reality, there will often be a limitation of the concentration of the implant, such as maximum concentrations of implanted gaseous ions which can be accommodated, or stoichiometric limits in ion beam synthesis. This can be accounted for in the simple model of "local saturation", which assumes that any atom which is implanted into a region where the maximum concentration has already been reached, is immediately released from the substance. In this model, the profile evolution with a maximum concentration $c_{i,max}$ is given by

$$c_i(x, \Phi) = \begin{cases} \frac{1}{n} f_R(x) \cdot \Phi & \text{if } c_i < c_{i,max} \\ c_{i,max} & \text{else} \end{cases} \quad (15.9)$$

Fig. 15.2(a) shows an example of implantation profiles calculated in the local saturation approximation, on the basis of a range profile calculated by TRIM.

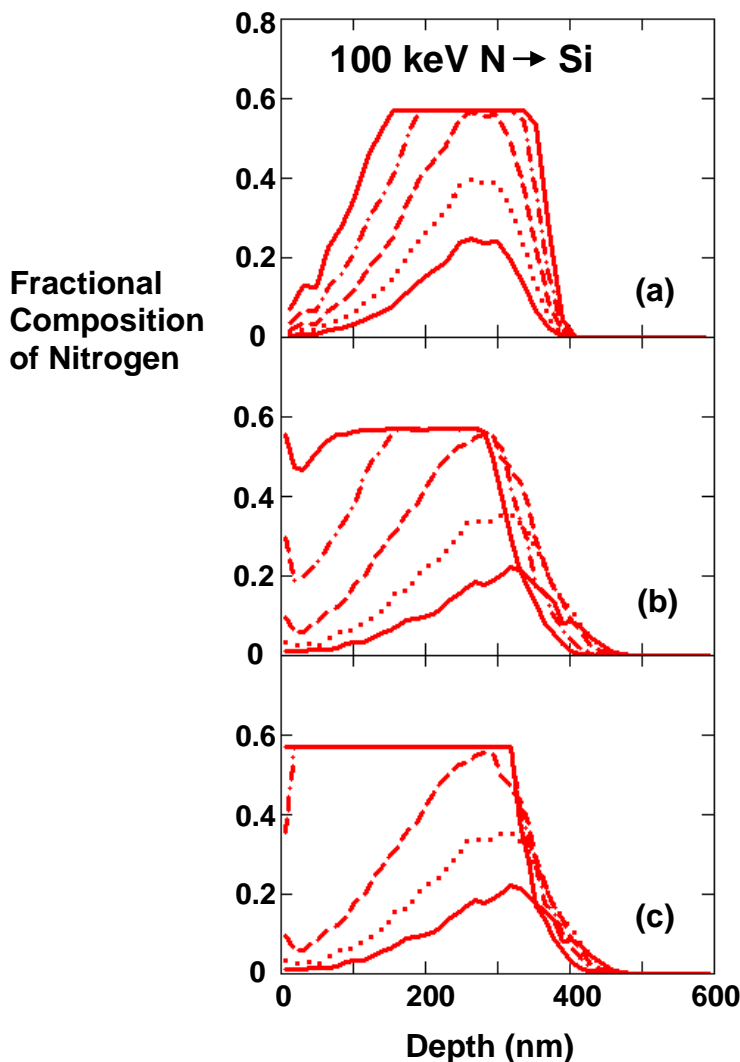


Fig. 15.2

Profiles of local saturation for 100 keV nitrogen implanted into silicon, with a maximum atomic fraction of 0.571 corresponding to Si_3N_4 . The fluences are $2.5 \cdot 10^{17} \text{ cm}^{-2}$ (solid line), $5 \cdot 10^{17} \text{ cm}^{-2}$ (dotted line), $1 \cdot 10^{18} \text{ cm}^{-2}$ (dashed line), $2 \cdot 10^{18} \text{ cm}^{-2}$ (dashed-dotted line) and $4 \cdot 10^{18} \text{ cm}^{-2}$ (solid line).

(a) Simple scaling of the range profile according to eq. (15.9), with the range profile taken from TRIM (SRIM 2000-39).

(b) From TRIDYN calculation including range broadening and sputtering. The nitrogen peak at the surface is due to preferential sputtering (see sect. 15.4).

(c) From TRIDYN calculation with simple model of "diffusion".

In reality, high-fluence implantation profiles are influenced by a number of effects which cannot easily be covered by a simple model. The presence of the implanted species influences the stopping and scattering of the incident ions so that the range profiles may be changed during the implantation. This may lead to a distortion of the implantation profiles in addition to the distortion which is caused by the relaxation of the host matrix ("swelling" due to the implanted atoms). Both are covered by dynamic BCA computer simulations. The model of local saturation can easily be incorporated into the simulation, by limiting the maximum concentration of the implanted species. The result from a TRIDYN calculation is shown in Fig. 15.2(b). In comparison with the simple analytical approach, already the profile corresponding to the lowest fluence displayed is broadened due to swelling. Towards the highest fluences, the profiles are further broadened and shifted towards the surface, due to sputtering.

In TRIDYN, it is also possible to employ a simplistic model of "diffusion", in which excess atoms are deposited in the non-saturated regions at the edges of the profiles rather than being discarded. (Actually, an atom coming to rest in a saturated region is moved to the closest depth interval which is not saturated.) The result is shown in Fig. 15.2(c), with considerable additional broadening towards the surface for the highest fluences. It depends critically on the system under investigation which of the above models can be applied.

15.3 Sputter-Controlled Implantation Profiles

In the example of Fig.15.2, the ion energy has been chosen sufficiently large so that the surface layer which is removed by sputtering is small compared to the mean projected ion range, and that the local saturation is not significantly influenced by sputtering. In contrast, at sufficiently small projected range and/or sufficiently high sputter yield, the high-fluence implantation profiles can be controlled entirely by ion deposition and sputtering. A qualitative picture is shown in Fig. 15.3.

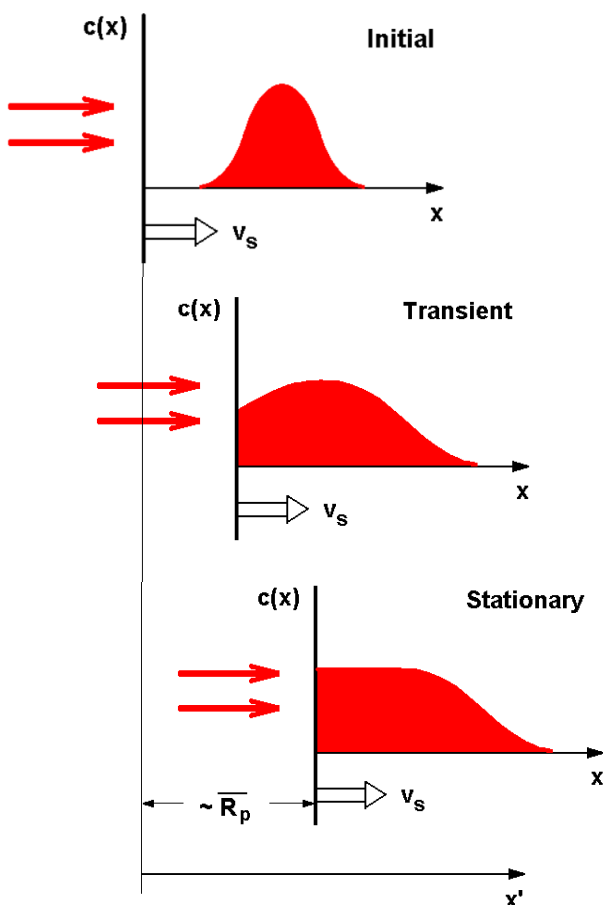


Fig. 15.3

Schematic representation of the formation of sputter-controlled implantation profiles. Range distribution and low-fluence profiles (top) with the surface moving with a velocity v_s due to sputtering, transient profile (middle) when the sputtered depth becomes comparable to the mean projected range, and stationary final profile (bottom).

Due to sputtering, the deposition profile is shifted towards the surface. Simultaneously, additional ions are implanted at the deep edge of the profile, which causes a profile broadening. Finally, when a surface layer which is thick compared to the projected range is sputtered off, a stationary profile is established with a high concentration at the surface, with the ingoing ion flux being balanced by the sputtered flux.

For a simplified treatment, a Gaussian range distribution is assumed according to

$$f_R(x) = \frac{I}{\sqrt{2\pi}\sigma} \exp\left(-\frac{(x - \bar{R}_p)^2}{2\sigma^2}\right) \quad (15.10)$$

where x is the depth in the system of the moving surface. According to the transformation into the fixed laboratory frame,

$$x' = x + v_s t \quad (15.11)$$

where v_s denotes the surface velocity due to sputtering, the range distributions

$$f'_R(x', t) = f_R(x' - v_s t) \quad (15.12)$$

are superposed in the laboratory frame with increasing time. The resulting time-dependent concentration of the implant is with the ion flux j_i , for $x' > v_s t$

$$n_i(x', t) = j_i \int_0^t f'_R(x', t') dt' \quad (15.13)$$

According to its definition, eq. (13.1), the sputtering yield it is related to the surface velocity by

$$j_{sp} = n \cdot v_s = Y \cdot j_i \quad (15.14)$$

By integration of (15.13), transformation to x and normalising to the host atomic density, the relative time-dependent concentration of the implant becomes, with erf denoting the error function

$$c_i(x, t) = \frac{I}{Y} \left[\text{erf}\left(\frac{x + v_s t - \bar{R}_p}{\sigma}\right) - \text{erf}\left(\frac{x - \bar{R}_p}{\sigma}\right) \right] \quad (15.15)$$

It has been implicitly assumed that the sputtering yield is independent of time, which is an approximation since it might be significantly influenced by the presence of the implanted species. Further, eq. (15.15) is strictly valid only for small concentrations of the implant, as eq. (15.14) becomes invalid for large surface concentration of the implant. This requires a sputtering yield which is significantly larger than one. From (15.15), the stationary implantation profile in the limit of long time becomes

$$c_i(x, t \rightarrow \infty) = \frac{I}{Y} \left[\frac{1}{2} - \text{erf}\left(\frac{x - \bar{R}_p}{\sigma}\right) \right] \quad (15.16)$$

The results (15.14) and (15.15) are qualitatively shown in Fig. 15.3. From (15.16), the surface concentration results for a sufficiently narrow Gaussian, $\sigma \ll R_p$, as

$$c_i(x = 0, t \rightarrow \infty) = \frac{I}{Y} \quad (15.17)$$

i.e., the relative surface concentration is given by the inverse of the sputtering yield.

More exact sputter-controlled implantation profiles can be obtained from dynamic BCA simulations. Fig. 15.4 shows the retained amount and a sequence of implantation profiles for sulfur ions incident on molybdenum. The depth profile at the lowest fluence, which reflects the range profile, becomes significantly distorted at the higher fluences. Stationarity is obtained at a fluence around $1.5 \cdot 10^{17} \text{ cm}^{-2}$, after about 20 nm, which is approximately 2.5 times the mean projected range, have been sputtered off. Compared to the simple error-functional shape predicted by eq. (15.16), there is a concentration drop at the surface due to preferential sputtering (see sect. 15.4). Nevertheless, the stationary profiles exhibit a nearly flat top with an atomic fraction of about 0.4, corresponding to a relative concentration (see eq. (15.8)) of 0.67. The sputtering yield for 10 keV sulfur ions incident on molybdenum is 2 according to the Sigmund formula, eq. (13.10). Thereby, the simple analytical result of eq. (15.17) is about 30% smaller.

The result demonstrates the impossibility to reach the concentration of the stoichiometric compound, MoS_2 , under the present conditions.

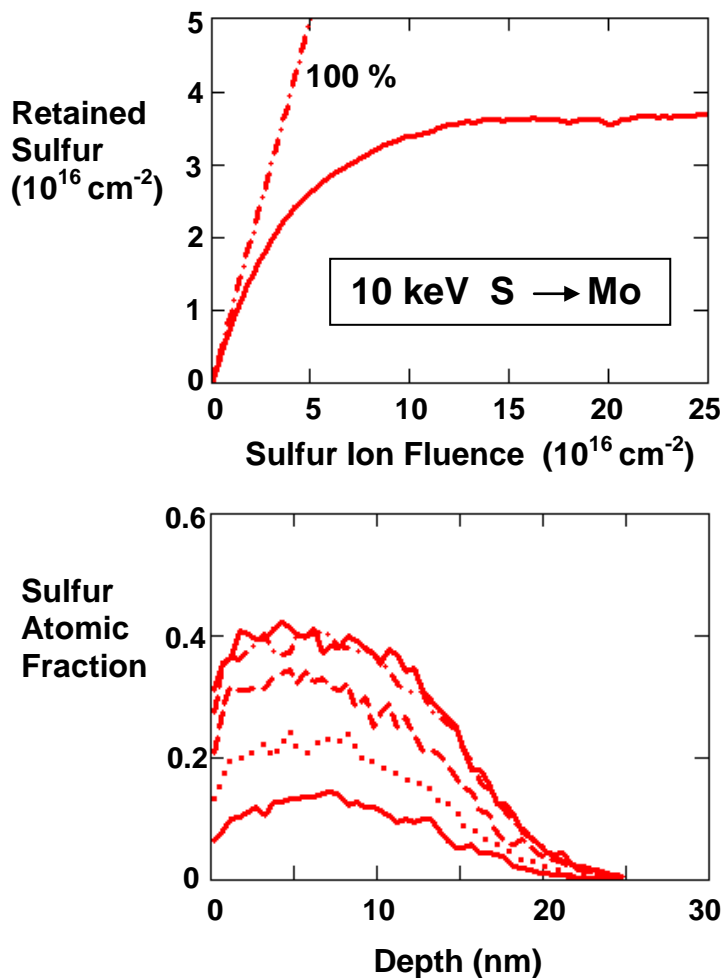


Fig. 15.4

Sputter-controlled implantation profile for 10 keV sulfur in molybdenum from a TRIDYN (vs. 4.0) computer simulation. Retained amount vs. ion fluence (top) and corresponding implantation profiles (bottom), at fluences of $1.5 \cdot 10^{16} \text{ cm}^{-2}$ (solid line), $3 \cdot 10^{16} \text{ cm}^{-2}$ (dotted line), $6 \cdot 10^{16} \text{ cm}^{-2}$ (dashed line), $1.2 \cdot 10^{17} \text{ cm}^{-2}$ (dashed-dotted line) and $2.4 \cdot 10^{17} \text{ cm}^{-2}$ (solid line). At the final fluence, a surface layer of 27.5 nm has been sputtered off.

15.4 Preferential Sputtering

According to eq. (13.10), the sputter yield is inversely proportional to the surface binding energy. It also increases with the energy transfer from the incident ion to the target atoms. Both may be different for the different atomic species in a multicomponent target material. In the limit of low fluence, the total sputtering yield can, in a first approximation, be superposed from the different components i according to their surface concentration. For this purpose, so-called "component" sputtering yields Y_i^c are defined such that the partial sputtering yields Y_i are given by

$$Y_i = q_i^s Y_i^c \quad (15.18)$$

with q_i^s denoting the surface atomic fractions. The total sputtering yield is then

$$Y = \sum_i Y_i \quad (15.19)$$

The linear dependence of the partial yields of the surface concentrations neglects any composition-dependent effects on the sputtering such as due to chemical compound or phase formation. For solid components, the component sputtering yields can be identified with the sputtering yields of the pure material of that component ($q_i^s=1$ in eq. (15.18)).

For different component sputtering yields, the equation

$$\frac{Y_i}{Y_j} \neq \frac{q_i^s}{q_j^s} \quad (15.20)$$

holds for at least one pair of components (i,j). In this case, one or more components are sputtered preferentially.

Consequently, the surface concentrations are altered at increasing fluence even in a homogeneous material. For simplicity, we assume a two-component material with the components A and B, with A being sputtered preferentially. The surface concentration of A, and thereby the partial sputtering yield of A, will then decrease with increasing fluence towards a stationary state, which is given by

$$\frac{Y_A^\infty}{Y_B^\infty} = \frac{q_A}{q_B} \quad (15.21)$$

where Y_i^∞ denote the stationary partial sputtering yields and q_i the bulk atomic fractions. Eq. (15.20) simply states mass conservation, as in the stationary state the altered composition profiles remain constant but are moved into the bulk due to sputter erosion, so that atoms sputtered at the surface must be balanced by atoms fed from the bulk into the altered layer (see Fig. (15.5)).

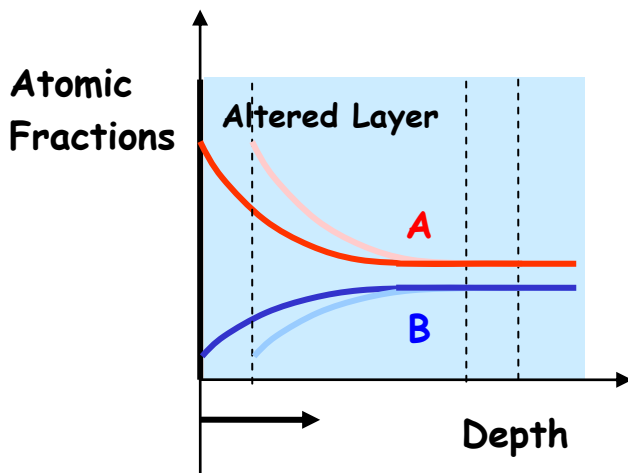


Fig. 15.5

Stationary composition profiles in an initially homogeneous two-component material due to preferential sputtering of the component B (schematic). The altered layer is moved into the bulk due to sputter erosion.

By relating eq. (15.18) for both components and combining with eq. (15.21), the following expression is obtained for of the stationary surface composition with the atomic fractions (q_i^s)[∞]

$$\frac{(q_A^s)^\infty}{(q_B^s)^\infty} = \left(\frac{q_A}{q_B} \right)^2 \frac{Y_B^0}{Y_A^0} \quad (15.22)$$

i.e., the final surface composition is determined uniquely by the initial partial sputtering yields Y_i^0 .

An example is given in Fig. 15.6 for the preferential sputtering of Ta_2O_5 by helium ions. The energy transfer to oxygen atoms is larger than to tantalum atoms. In addition, for the rather low light ion energy, threshold effects become important in particular for tantalum. (Eq. (13.12) yields a helium threshold energy of about 100 eV for the sputtering of pure tantalum.) Both effects result in a strong enrichment of tantalum at the surface. For a wide range of angles of incidence, the experimental values are in good agreement with eq. (15.22), and also with the results of TRIDYN computer simulations. At the first glance, the pronounced dependence of the stationary surface concentration on the angle of incidence is surprising, since a $\cos^{-1}\theta$ dependence (see eq. (13.10)) is expected for the partial sputtering yields of both oxygen and tantalum, so that eq. (15.22) would predict a stationary surface composition which is independent on the angle of incidence. Actually, the angular dependence is due to details of the collision sequences which cause sputtering. The heavy tantalum atoms are little influenced by the presence of oxygen. In contrast, oxygen atoms may be significantly scattered by tantalum, which results in a weaker dependence of the partial oxygen yield on the angle of incidence.

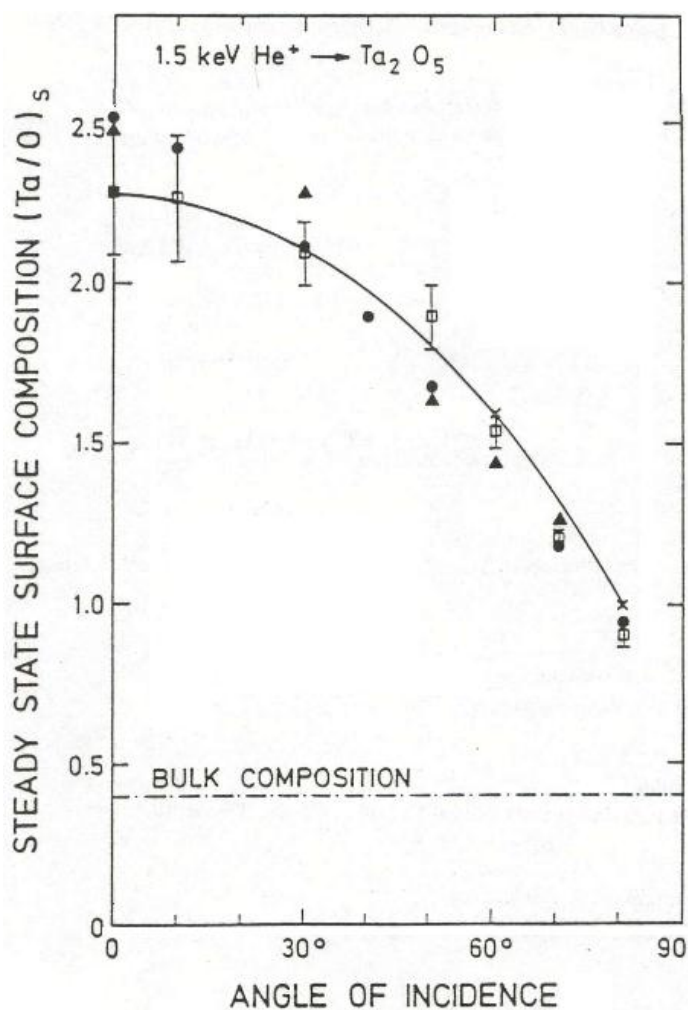


Fig. 15.6

Stationary surface composition due to preferential sputtering during 1.5 keV helium bombardment of tantalum oxide versus the angle of incidence, from experiments using Auger electron spectroscopy (dots) and ion surface scattering (triangles), TRIDYN dynamic computer simulations (squares), and calculated using eq. (15.22) for each angle (crosses connected by line) with initial partial sputtering yields from the TRIDYN simulations. The angle of incidence is defined with respect to the surface normal.

A second example is displayed in Fig. 15.7 for the sputtering of tantalum carbide by helium. The inset shows the evolution of the partial sputtering yields, as obtained from TRIDYN computer simulation. Initially, carbon is sputtered strongly preferentially and denuded at the surface. Consequently, its partial yield decreases, whereas the partial yield of tantalum increases. Both converge to a ratio of 1:1 according to eq. (15.21). The total stationary sputtering yield, as obtained from the simulation, shows good agreement with the experimental data.

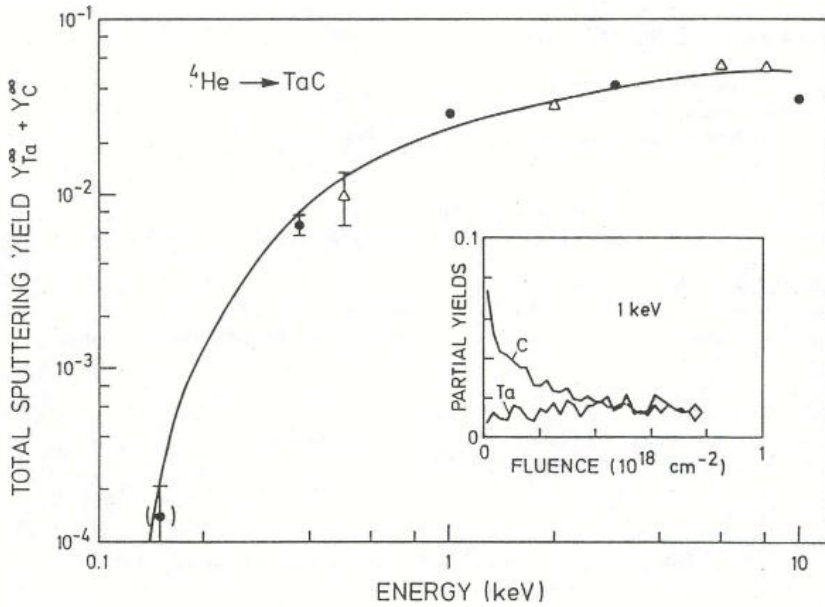


Fig. 15.7

Total stationary sputtering yield of tantalum carbide during helium bombardment, as function of the ion energy, from TRIDYN computer simulation (full points) and experiments (open triangles). The line is from an empirical fit function. The inset shows the dependence of the partial sputtering yields on the ion fluence, at an energy of 1 keV.

15.5 Ion Mixing

In an inhomogeneous multicomponent substance, the relocation of atoms due to ion knockon and in collision cascades results in "mixing" of the atoms. Prototypes of inhomogeneous materials are a thin marker of atoms A in an otherwise homogeneous material B, and an A/B bilayer as a simple example of a multilayer medium (Fig. 15.8).

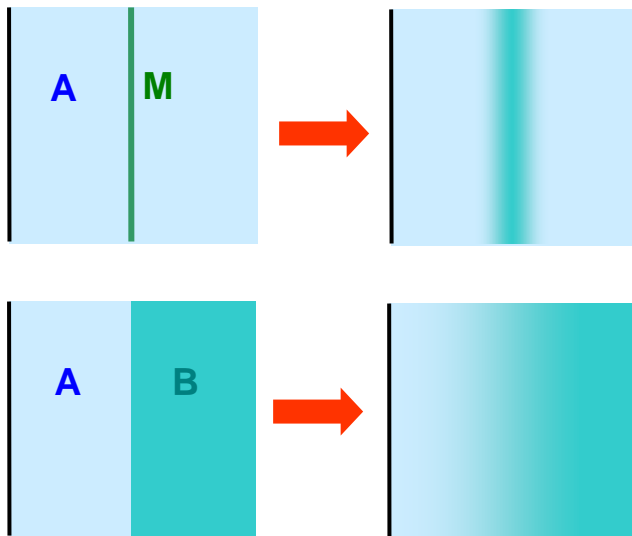


Fig. 15.8

Schematic of ion mixing in a marker system (thin marker M in a matrix A, top) and in a bilayer system (layer A on top of a layer or bulk B, bottom). Due to ion bombardment, the marker and the interface become diffuse, respectively.

There are three main mechanism of ion mixing, as indicated in Fig. 15.9. Matrix atoms can be relocated by primary collisions into or beyond the marker; this leads to marker broadening and to a shift towards the surface. Marker atoms, which are relocated by primary collisions towards larger depth, result in a tail of the marker profile, and thereby in a broadening and a shift towards the bulk. Finally, collision cascades initiated by sufficiently large primary energy transfers are more or less isotropic and cause mainly a broadening of the marker. These events interact in a complicated way. A simple analytical prediction can only be obtained for the isotropic cascade mixing [22].

For a marker system, the relocation of the marker atoms is described by relocation cross section $d\sigma(x,z)$, which describes the displacement of a marker atom due to ion bombardment, with an energy transfer T at a starting angle Θ from an original depth x by a depth increment z (see Fig. 15.10).

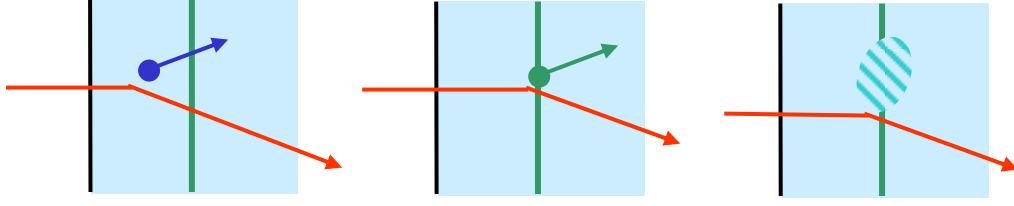


Fig. 15.9 Mechanisms of ion mixing in a marker system: Matrix relocation (left), marker relocation (middle) and cascade mixing of the marker (right).

For many incident ions, multiple displacements are obtained. The mean displacement of a marker atom for a given ion fluence Φ is

$$\langle \Delta x \rangle = \Phi \int_{-\infty}^{\infty} z d\sigma(x, z) \quad (15.22)$$

and the variance (to be shown in analogy to the variance of electronic energy loss - see sect. 6.3)

$$\Omega_m^2 = \langle (\Delta x - \langle \Delta x \rangle)^2 \rangle = \Phi \int_{-\infty}^{\infty} z^2 d\sigma(x, z) \quad (15.23)$$

Collision cascades are mainly developed by matrix atoms, as the number of marker atoms is small. Matrix atoms of the cascades may collide with marker atoms thus causing them to be relocated. The relocation cross section is then given by

$$\begin{aligned} \frac{d\sigma(x, z)}{dz} = & \int dE_0 \int d\Omega_0 \int d\bar{f} \cdot \frac{1}{4\pi} F(E, \bar{\eta}, E_0, \bar{r}) \bar{\eta}_0 \\ & \times |\cos \theta_0|^{-1} \int d\sigma_m(E_0, \bar{\eta}_0, T, \bar{\eta}') \cdot f_R(T, \bar{\eta}', z) \end{aligned} \quad (15.24)$$

The first line of eq. (15.24), in the notation of chs. 10 and 13, denotes the flux of matrix cascade atoms through the marker plane at x . The second line contains the probability of collisions $d\sigma_m$ with marker atoms, which receive an energy transfer T at a direction η' . The cosine term reflects the increased collision probability at an inclined direction of the matrix atom. f_R denotes the range distribution of the marker recoil atom. Similar to the treatment of sputtering (see eq. (13.5)), the area integral of the cascade function F can be written as

$$\int d\bar{f} \cdot \frac{1}{4\pi} F(E, \bar{\eta}, E_0, \bar{r}) \bar{\eta}_0 = \frac{6}{4\pi^3} \frac{F_D(E, \eta, x) |\cos \theta_0|}{E_0 n S_m(E_0)} \quad (15.25)$$

with F_D now denoting the one-dimensional damage function and S_m the stopping cross section of the matrix atoms in the matrix.

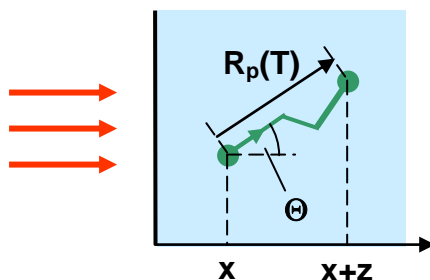


Fig. 15.10

Relocation of a marker atom starting at an angle Θ with an energy transfer T . R_p denotes its projected range.

For power law-scattering, again with $m \rightarrow 0$, the evaluation of (15.23-25) yields

$$\Omega_m^2 = \frac{2\gamma}{\pi^2} S_n(\bar{E}(x)) \frac{(R_p(U_m))^2}{U_m} \Phi \quad (15.25)$$

where γ denotes the energy transfer factor, S_n the nuclear stopping cross section of the incident ions at the mean energy at the depth of the marker, U_m a threshold energy of marker atoms below which no relocation occurs, and R_c the associated mean projected range.

The definition of the threshold energy is questionable to some extent. It can be assumed to be significantly smaller than the damage threshold energy U_d , as replacement sequences might influence the relocation more than the Frenkel pair formation. Further, in contrast to the formation of isolated Frenkel pairs, ion mixing is a high-fluence phenomenon, so that the substance can be assumed to be already heavily damaged. Stable relocation might then result from much smaller initial recoil energies than stable Frenkel pair formation in an undisturbed lattice. From experience, a choice of 8 eV has turned out to reproduce experimental data of collisional mixing rather well.

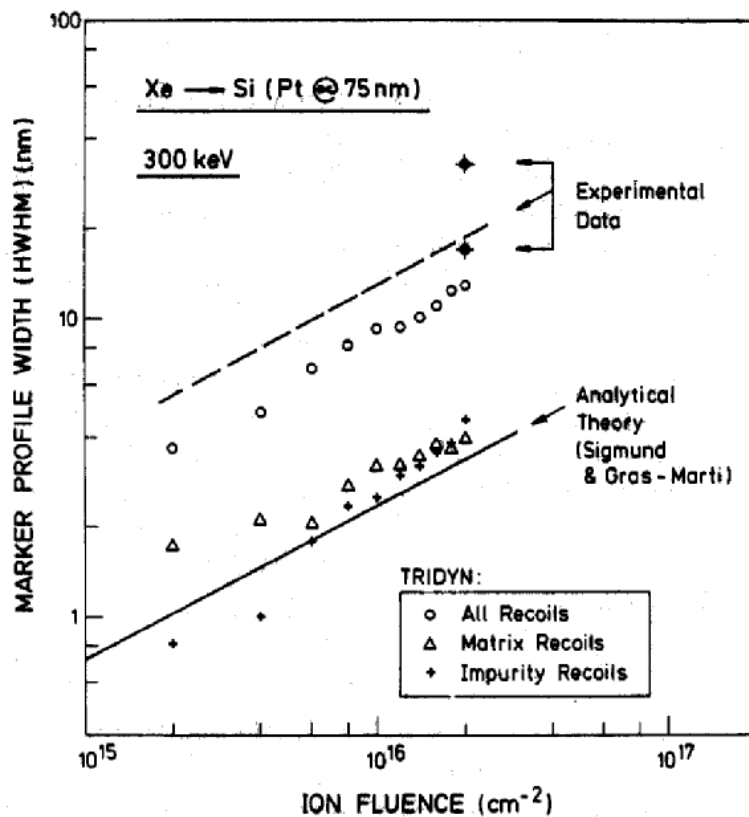


Fig. 15.11

Collisional mixing (half width at half maximum of the marker profile) by 300 keV Xe ions for an initially thin platinum marker in silicon at an initial depth of 75 nm, from experiments (dashed line, crossed dots), the analytical formula of cascade mixing - eq. (15.25) (solid line), and TRIDYN computer simulation (circles) with a cutoff energy $U_m = 8$ eV. Results from TRIDYN are also shown for the treatment of matrix recoils (triangles) and marker recoils (crosses) only.

Fig. 15.11 shows an example of marker mixing with 300 keV xenon ions. The analytical prediction (eq. (15.25)) is seen to underestimate the experimental data significantly, as it only covers isotropic cascade mixing. Dynamic BCA computer simulation does not suffer from this restriction. However, the mixing results also depend critically on the choice of the cutoff energy, so that the TRIDYN result is in rather good agreement with experiment. (The wide span of experimental data should also be noted, indicating experimental difficulties.) TRIDYN also offers the possibility to suppress matrix or marker recoils. Both results are in reasonable agreement with the analytical prediction, which is probably fortuitous as the analytical approach does not cover the recoils of an individual species, but the combination of both. However, the computer simulation demonstrates that the effects of matrix and marker recoils interact strongly (a quadratic summation of both remains significantly below the results when both species are taken into account). This is due to correlation of the marker broadening

with the marker shift, which exhibits a different sign for matrix and marker knockon as discussed above.

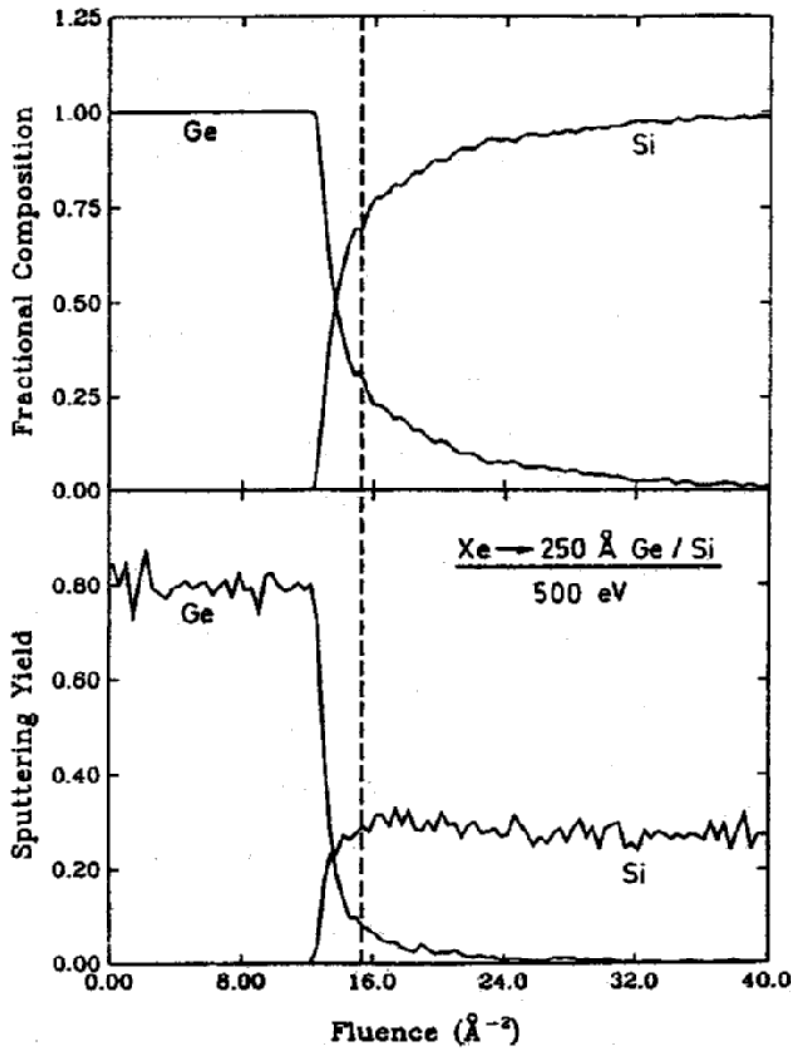


Fig. 15.12

Mixing of a bilayer system during sputter erosion by 500 eV xenon bombardment, as indicated by the surface composition (top) and the partial sputtering yields (bottom) during the irradiation, from a TRIDYN computer simulation. The dashed line indicates the fluence at which the original Ge thickness of 25 nm would be sputtered off with the initial sputtering yield of germanium.

In general, ion mixing and sputtering, including preferential sputtering, interact in a complicated way. For such problems, simple analytical descriptions are not available so that the dynamic computer simulation remains as the only viable instrument. Fig. 15.12 shows an example of sputter removal of a thin film, as it is frequently used for near-surface depth profiling by, e.g., secondary ion mass spectrometry or Auger electron spectroscopy. The initially sharp interface is significantly broadened when it is reached after sputtering. As the range of 500 eV xenon ions in germanium is only about 2 nm, cascade mixing only occurs when the remaining Ge thickness is in the order of the ion range or less. However, recoil implantation and long-range collision sequences also play a role, which is confirmed by the high asymmetry of the interface mixing. In Fig. 15.12, the crossover of the Ge and Si signals, which would normally be taken for the interface position, deviates significantly from the fluence at which a equal layer of pure germanium would have been sputtered off. Thus, mixing and recoil implantation might cause artefacts for the interpretation of depth profiling experiments.